Phase Field Modeling and Numerical Algorithm for Two-Phase Dielectric Fluid Flows

Jielin Yang¹, Ivan C. Christov², Suchuan Dong^{1*}

¹Department of Mathematics,

²School of Mechanical Engineering,
Purdue University, West Lafayette, IN47907, USA

(May 31, 2024)

Abstract

We develop a method for modeling and simulating a class of two-phase flows consisting of two immiscible incompressible dielectric fluids and their interactions with imposed external electric fields in two and three dimensions. We first present a thermodynamically-consistent and reduction-consistent phase field model for two-phase dielectric fluids. The model honors the conservation laws and thermodynamic principles, and has the property that, if only one fluid component is present in the system, the two-phase formulation will exactly reduce to that of the corresponding single-phase system. In particular, this model accommodates an equilibrium solution that is compatible with the zero-velocity requirement based on physics. This property leads to a simpler method for simulating the equilibrium state of two-phase dielectric systems. We further present an efficient numerical algorithm, together with a spectral-element (for two dimensions) or a hybrid Fourier-spectral/spectral-element (for three dimensions) discretization in space, for simulating this class of problems. This algorithm computes different dynamic variables successively in an un-coupled fashion, and involves only coefficient matrices that are time-independent in the resultant linear algebraic systems upon discretization, even when the physical properties (e.g. permittivity, density, viscosity) of the two dielectric fluids are different. This property is crucial and enables us to employ fast Fourier transforms for three-dimensional problems. Ample numerical simulations of two-phase dielectric flows under imposed voltage are presented to demonstrate the performance of the method herein and to compare the simulation results with theoretical models and experimental data.

Keywords: phase field, dielectric flow, thermodynamic consistency, reduction consistency, dielectrowetting, two-phase flow

1 Introduction

In the current work we focus on the modeling and simulation of a system of two immiscible incompressible dielectric fluids and their interaction with external electric fields. Dielectric fluids refer to fluids that are electrically non-conductive and can withstand high voltage without breakdown. They are traditionally used for cooling and insulating electrical equipment such as transformers and high-voltage cables. In recent years dielectric fluids have found widespread applications in electric vehicles, for cooling the electric motor, batteries, electric transmissions, and power electronics.

Using electric field is a widely-adopted technique for manipulating small amounts of liquids on surfaces. Electrowetting-on-dielectric (EWOD) [57] is one of the most successful and versatile approaches. EWOD systems typically involve conducting fluids or droplets on a dielectric substrate under an imposed voltage. The applications of EWOD range from "lab-on-a-chip" devices [67, 14], to adjustable lenses [6], to new types of electronic displays [35]. While EWOD is effective in fluid manipulation, it requires the fluids to be conductive and an AC (alternating-current) electric potential.

^{*}Author of correspondence. Emails: yang1659@purdue.edu (Yang), christov@purdue.edu (Christov), sdong@purdue.edu (Dong)

Using dielectrophoresis (DEP) underlies another class of techniques for manipulating fluids [5, 28], and has an advantage over EWOD in some situations [26]. Dielectrophoresis refers to the electromechanical force due to the polarization of a neutral material in non-uniform electric fields [26]. One can use the Korteweg-Helmholtz force density [43] to explain the origination of liquid dielectrophoresis. Applying an electric field **E** to the fluid results in the Korteweg-Helmholtz force density

$$\mathbf{f}_{KT} = \rho_f \mathbf{E} - \frac{1}{2} (\mathbf{E} \cdot \mathbf{E}) \nabla \epsilon + \nabla \left[\frac{1}{2} (\mathbf{E} \cdot \mathbf{E}) \rho \frac{\partial \epsilon}{\partial \rho} \right], \tag{1}$$

where ρ_f is the free electric charge density, ϵ is the permittivity, and ρ is the fluid density. Based on equation (1), in the absence of free charge ($\rho_f = 0$), as long as nonuniform polarisation of dipoles exists within the liquid ($\nabla \epsilon \neq 0$), the fluid will be influenced by the electric field; see [29, 59] for more detailed discussions of the DEP force theory.

The use of DEP to move bulk fluids can be traced to Pellat's work in 1895 [26]. A dielectric siphon is described in [41] to pump fluids between two reservoirs. DEP is used to transport dielectric particles or droplets in [5] through a channel sandwiched by electrodes. Transport of dielectric liquids at microscale and in microfluidic devices has been studied with miniaturized electrodes in [40, 39, 12]. In [9] the authors use DEP to spread a droplet onto coplanar electrodes to form a thin liquid film, estalishing the idea of interface localized liquid dielectrophoresis. In [54] the effect of localized DEP on the wetting properties of solid-liquid interface has been investigated and the term dielectrowetting is introduced. We refer to [74, 29, 53] for a review of this area and recent applications.

Two-phase systems of dielectric fluids involve fluid interfaces, the associated surface tension, the contrast in fluid properties (permittivity, density, and viscosity), contact lines and contact angles when a solid-wall boundary is present, and the interaction with the imposed electric field. The approach taken in the current work to handle the two phases belongs to the phase field framework. Phase field (a.k.a. diffuse interface) [60, 71, 3, 50, 37, 7, 48, 17] is one of the few techniques currently available for dealing with two-phase systems and fluid interfaces. It is particularly attractive because of its physics-based nature. With phase field the fluid interface is treated as a thin smooth transition layer (i.e. diffuse). Besides the hydrodynamic variables, the system is characterized by an order parameter (or phase field function), which varies smoothly within the transition layer and is mostly uniform in the bulk phases. The evolution of the fluid phases is driven by a free energy density function, which contains component terms that tend to promote the mixing of the two fluids and also component terms that tend to separate the fluids. The interplay of these two tendencies determines the dynamic profile of the fluid interface. With this approach, the governing equations can be derived rigorously based on the conservation laws and thermodynamic principles. We refer to e.g. [50, 42, 1, 66, 2, 19, 49, 30, 23, 61, 78] (among others) for several thermodynamically consistent phase field models for two-phase and multiphase flows with various degrees of sophistication.

While phase field is successful for a range of two-phase and multiphase problems, investigations into this approach for modeling two-phase hydrodynamics coupled with the electric field effect are still quite limited. In [44, 75, 76] the authors employ the phase field method coupled with the Navier-Stokes equations to study the electrohydrodynamic (EHD) phenomenon, in particular the Taylor's leaky dielelctric model [63]. The authors of [70] investigate the electrohydrodynamic patterning based on the liquid dielectrophoresis. In [72, 73] the phase field method is used to study electrowetting and its applications.

The aforementioned studies on the coupled multiphase flow and electric field have a notable drawback. These are phenomenological models, and do not admit an energy law (or energy balance relation). In other words, these models are not thermodynamically consistent. To overcome this issue, a phase field model is proposed in [25] for electrowetting (conductive fluids with free charges) based on variational principles and the thermodynamics of irresversible processes near equilibrium. The model combines multiphase flows, the electric field and the free charge system, and admits an energy balance relation. However, it only applies to cases when the two conductive fluids have the same density.

This model is extended in [10] to take into account the density contrast and the transport of free ions in the conductive fluids; see [55, 47, 56, 45] for numerical algorithms developed based on this extended model. Another diffuse interface model is proposed in [58] for electrowetting on dielectric with different densities for the two fluids, which however appears not to be Galilean invariant. In [46] a thermodynamically consistent continuum model for single-phase electrohydrodynamic flows has been described. The model combines the Navier-Stokes equations and the Poisson-Nernst-Planck (PNP) equations, in which the fluid properties

depend on the ion concentration fields. We would also like to note the finite element method developed in [81] employing a sharp-interface model for electrowetting on dielectric.

In this paper we look into the dynamics of an isothermal system of two immiscible incompressible dielectric fluids and their interaction with external electric fields in two and three dimensions (2D/3D). The fluids considered here are non-conductive and the system contains no free charges or ions. This setting is quite different from those studies reviewed in previous paragraphs related to electrowetting or electrohydrodynamics, where the fluids are electrolytic solutions and conductive and the transport of free ions is crucial to the system dynamics. Due to liquid dielectrophoresis and the Korteweg-Helmholtz force, when an external voltage is imposed, the interface between the dielectric fluids can experience large deformations, leading to the dielectrowetting phenomenon [26].

We first present a thermodynamically-consistent and reduction-consistent phase field model for two-phase dielectric flows. Thermodynamic consistency refers to the property that the model honors the conservation laws and thermodynamic principles [50, 1, 69]. The current model is developed based on the conservations of mass and momentum and the second law of thermodynamics, in which the physical properties of the two fluids (permittivity, density, and viscosity) can be different. The model derivation process follows those of [1, 19, 23], with the quasi-static electromagnetic equations taken into account. Reduction consistency refers to the property that, when only one fluid component is present in the two-phase system (while the other fluid is absent), the two-phase formulation will exactly reduce to that of the corresponding singlephase system. We refer to [23] for discussions of reduction consistency in general multiphase systems. The reduction consistency of a two-phase dielectric system places restrictions on the functional form of the mixture permittivity when expressed in terms of the phase field variable. As discussed in [23], reduction consistency reflects an inherent reduction relation within multiphase systems, and violation of reduction consistency can lead to unphysical results (e.g. production of a fluid phase where it is absent). The phase field model here for dielectric fluids appears to have some connection to that of [10] for conductive fluids and electrolytic solutions. We note that the reduction consistency issue was not considered in [10] or the related works of [55, 47, 56, 45] for conductive fluids, and the model as given therein appears not reduction-consistent.

At equilibrium, the solution to the current model is compatible with the zero-velocity requirement based on physics. This property leads to a method for computing the equilibrium state (or steady state) of two-phase dielectric systems, which is of great practical interest and importance, by solving a smaller reduced system of equations. This method is simpler and faster than integrating the full model in time until the steady state is reached.

We then present a semi-implicit splitting type algorithm, together with a spectral-element spatial discretization for 2D and a hybrid Fourier-spectral/spectral-element discretization for 3D, for numerically solving the governing equations of this two-phase dielectric flow model. The computations for different dynamic variables (electric potential, phase field function, velocity, and pressure) are de-coupled with our method. For each dynamic variable, the resultant linear algebraic system upon discretization involves a constant and time-independent coefficient matrix, which can be pre-computed and saved for later use, despite the variable physical properties (permittivity, density, viscosity) of the two-phase mixture. This characteristic of the current algorithm is crucial, and it enables the use of Fourier spectral discretization and fast Fourier transform (FFT) in 3D simulations of two-phase dielectric flows with variable mixture properties. For 3D problems, with each dynamic variable, the computations of different Fourier modes are completely de-coupled with the current method. Thanks to these characteristics, the presented method is computationally very efficient.

These attractive properties are attained based on several strategies. The most important strategy, for producing a semi-discretized system having constant coefficients when variable material properties are present on the continuum level, is inspired by and built upon the algorithm from [24] (with modifications). The main idea of [24] lies in a reformulation of the pressure/viscous terms in the momentum equation as follows,

$$\frac{1}{\rho}\nabla p \approx \frac{1}{\rho_0}\nabla p + \left(\frac{1}{\rho} - \frac{1}{\rho_0}\right)\nabla p^*, \qquad \frac{\mu}{\rho}\nabla^2 \mathbf{u} \approx \nu_m \nabla^2 \mathbf{u} - \left(\frac{\mu}{\rho} - \nu_m\right)\nabla \times \nabla \times \mathbf{u}^*,$$

where ρ and μ are the variable density and variable viscosity of the mixture, ρ_0 and ν_m are two appropriate constants, p and \mathbf{u} are the pressure and the divergence-free velocity, and p^* and \mathbf{u}^* are explicit approximations of p and \mathbf{u} with a prescribed order of accuracy. Such and similar reformulations lead to a semi-discretized system of equations with constant coefficients, in spite of the variable fluid properties on the continuum level. This semi-discretized system with *constant* coefficients is critical to the success of subsequent Fourier

spectral discretization in one or more directions in 3D space. This is because, if this system has variable coefficients, the FFT will induce convolutions with the coefficient functions in the frequency space, which will couple together all the Fourier modes of the unknown dynamic variables to be solved for.

The current algorithm is semi-implicit in nature, in which the nonlinear terms are treated explicitly and the linear terms are treated implicitly. As such the algorithm is only conditionally stable, in the sense that the time step size employed in the simulations cannot be large. On the other hand, this conditional stability in the algorithm enables very efficient computations within each time step, with constant precomputable coefficient matrices and de-coupled computations for all dynamic variables. As opposed to the semi-implicit approach, one may also consider the development of energy-stable type schemes, which is not pursued here. Energy-stable schemes are discretizations designed to satisfy a discrete version of the energy law, irrespective of the time step size. The strength of energy-stable schemes lies in that they are unconditionally stable and can allow the use of relatively large time step sizes in the simulations. We refer to e.g. [64, 62, 33, 31, 65, 32, 77, 61] (among others) for several energy-stable schemes for two-phase problems. The downside of the energy-stable algorithms lies in that their computational cost per time step can be very high. These schemes typically involve the solution of coupled nonlinear algebraic equations or coupled linear algebraic equations, and the linear algebraic systems resultant from these schemes involve time-dependent coefficient matrices, which require frequent re-computations (e.g. at every time step).

We present a number of numerical examples of two-phase dielectric flows under an imposed voltage in 2D and 3D to test the performance of the presented method. In particular, we compare the current simulation results with theoretical models and the experimental data from the literature. The comparisons show that the phase field model and the numerical method developed herein can capture the physics of this class of flow problems well.

The contributions of this paper lie in three aspects: (i) the reduction-consistent and thermodynamically-consistent phase field model for two-phase dielectric fluids, (ii) the simpler method for computing the equilibrium state of two-phase dielectric systems, and (iii) the efficient numerical algorithm for simulating two-phase dielectric flows.

The rest of this paper is organized as follows. In Section 2 we present the phase field model for two-phase dielectric flows and discuss the equilibrium solution to the model. In Section 3 we present the numerical algorithm for solving this model, and discuss the spectral-element implementation for 2D and the hybrid Fourier-spectral and spectral-element implementation for 3D. We employ several 2D and 3D two-phase dielectric flows to test the presented method in Section 4. In particular we compare the simulation results with theoretical models and the experimental data. Section 5 concludes the presentation with some closing remarks. In the Appendix we outline the development of the current phase field model based on the conservation laws and thermodynamic principles and discuss several further numerical tests.

2 Phase Field Model for Two-Phase Dielectric Fluids

Consider a domain Ω in two or three dimensions, and an isothermal system of two immiscible incompressible dielectric fluids in Ω . The two fluids are assumed to be Newtonian, with constant densities ρ_1 and ρ_2 , constant dynamic viscosities μ_1 and μ_2 , and constant relative permittivity ϵ_1 and ϵ_2 , respectively. We introduce a phase field variable ϕ , which assumes the constant values 1 and -1 in the bulk of the two fluids and has a smooth distribution in a thin layer surrounding the interface.

The material properties of the mixture are functions of the above parameters and the phase field variable ϕ , with the mixture density $\rho = \rho(\rho_1, \rho_2, \phi)$, mixture viscosity $\mu = \mu(\mu_1, \mu_2, \phi)$, and mixture permittivity $\epsilon = \epsilon(\epsilon_1, \epsilon_2, \phi)$. Specifically, we assume the following relations,

$$\begin{cases} \rho(\phi) = \frac{\rho_1 + \rho_2}{2} + \frac{\rho_1 - \rho_2}{2}\phi, & \mu(\phi) = \frac{\mu_1 + \mu_2}{2} + \frac{\mu_1 - \mu_2}{2}\phi, \\ \epsilon(\phi) = \frac{\epsilon_1 + \epsilon_2}{2} + \frac{\epsilon_1 - \epsilon_2}{2}\frac{\phi(3 - \phi^2)}{2}. \end{cases}$$
(2)

In the above relations, ρ and μ are linear with respect to ϕ , which has been commonly used (see e.g. [17, 21]). However, for ϵ we employ a relation based on the Hermite interpolation. The benefit of Hermite interpolation is that $\frac{d\epsilon}{d\phi} = 0$ in the bulk ($\phi = \pm 1$), while a linear relation would result in a non-zero derivative. The zero

derivative of permittivity plays an important role in our model, which will become clearer in later discussions.

2.1 Governing Equations

The model describing the motion of this system of fluids can be derived based on the conservation laws and thermodynamic principles. The development of this model has been discussed in detail in the appendix (Section 6.1). Here we only summarize the governing equations for this system.

Let **u** denote the velocity, \mathcal{P} denote the pressure, ϕ denote the phase field variable, V denote the electric potential, and **E** denote the electric field. Then the dynamics of this two-phase system is described by the following set of equations (see Section 6.1 for derivation and specifically (118) for the general form),

$$\frac{\partial \phi}{\partial t} + \mathbf{u} \cdot \nabla \phi = \gamma_1 \Delta \left(\lambda h(\phi) - \lambda \Delta \phi - \frac{\epsilon'}{2} \mathbf{E} \cdot \mathbf{E} \right), \tag{3}$$

$$\rho \left(\frac{\partial \mathbf{u}}{\partial t} + \mathbf{u} \cdot \nabla \mathbf{u} \right) + \tilde{\mathbf{J}} \cdot \nabla \mathbf{u} = -\nabla \cdot (\lambda \nabla \phi \otimes \nabla \phi) - \frac{\nabla \epsilon}{2} \mathbf{E} \cdot \mathbf{E} + \nabla \cdot \left[\mu \left(\nabla \mathbf{u} + \nabla \mathbf{u}^T \right) \right] - \nabla \mathcal{P}, \tag{4}$$

$$\nabla \cdot \mathbf{u} = 0,\tag{5}$$

$$\nabla \cdot (\epsilon \nabla V) = 0, \tag{6}$$

$$\mathbf{E} = \nabla V,\tag{7}$$

where the flux term $\tilde{\mathbf{J}}$ is given by

$$\tilde{\mathbf{J}} = -\gamma_1 \frac{\rho_1 - \rho_2}{2} \nabla \left(\lambda h(\phi) - \lambda \nabla^2 \phi - \frac{\epsilon'}{2} \mathbf{E} \cdot \mathbf{E} \right). \tag{8}$$

In these equations γ_1 is the mobility coefficient, and λ is the mixing energy density coefficient. ρ , μ and ϵ denote the density, dynamic viscosity, and permittivity of the mixture and are given in (2). $h(\phi)$ in equation (3) is defined by $\lambda h(\phi) = \frac{\partial F}{\partial \phi}$, where $F(\phi)$ is the interfacial mixing energy density function (with double well) given by,

$$F(\phi, \nabla \phi) = \frac{1}{2} \lambda |\nabla \phi|^2 + \frac{\lambda}{4n^2} (\phi^2 - 1)^2. \tag{9}$$

The constant η here is a length scale characterizing the interfacial thickness, and λ is related to the surface tension σ by $\lambda = \frac{3}{2\sqrt{2}}\sigma\eta$ [79]. So $h(\phi)$ is given by, $h(\phi) = \frac{1}{\eta^2}\phi(\phi^2 - 1)$.

With $\tilde{\mathbf{J}}$ given by (8) and ρ given in (2), equation (3) is equivalent to,

$$\frac{\partial \rho}{\partial t} + \mathbf{u} \cdot \nabla \rho = -\nabla \cdot \tilde{\mathbf{J}}.\tag{10}$$

Let μ_c denote a generalized chemical potential given by

$$\mu_c = \lambda h(\phi) - \lambda \nabla^2 \phi - \frac{\epsilon'}{2} \mathbf{E} \cdot \mathbf{E}. \tag{11}$$

Then, $\tilde{\mathbf{J}}$ can be written as, $\tilde{\mathbf{J}} = -\gamma_1 \frac{\rho_1 - \rho_2}{2} \nabla \mu_c$.

2.2 Reduction Consistency

We require that the system consisting of (3)–(7) should be reduction-consistent [23, 22]. In other words, if only one fluid component is present (while the other fluid is absent), the system of two-phase governing equations should exactly reduce to that of the corresponding single-phase system. This means that the system given by (3)–(7) should admit the following two solutions:

- $(\mathbf{u}, \mathcal{P}, V, \mathbf{E})$ and $\phi \equiv 1$: the first fluid is present, and the second fluid is absent.
- $(\mathbf{u}, \mathcal{P}, V, \mathbf{E})$ and $\phi \equiv -1$: the second fluid is present, and the first fluid is absent.

It can be verified that these solutions are ensured if the following conditions on $\epsilon(\phi)$ are satisfied,

$$\frac{d\epsilon}{d\phi}\Big|_{\phi=1} = 0, \qquad \frac{d\epsilon}{d\phi}\Big|_{\phi=-1} = 0.$$
 (12)

The choice for $\epsilon(\phi)$ in (2) satisfies these conditions. Therefore the phase field model given by (3)–(7), with the mixture properties given by (2), is reduction consistent. It is noted that if one chooses a linear form for $\epsilon(\phi)$ (similar to $\rho(\phi)$ and $\mu(\phi)$ in (2)), then the system (3)–(7) will not be reduction consistent (when $\epsilon_1 \neq \epsilon_2$). We refer to [23] for more detailed discussions of the reduction consistency for multiphase systems.

From the physics perspective, the electric field influences the generalized chemical potential through the term $\frac{\epsilon'(\phi)}{2} \mathbf{E} \cdot \mathbf{E}$. Physically, the generalized chemical potential in the phase field equation should only have an effect on the interface (not in the bulk region), i.e. μ_c should vanish in the bulk. This leads to the same conditions as given in (12). Therefore, the Hermite interpolation relation for $\epsilon(\phi)$ in equation (2) is crucial to the current model.

2.3 Energy Law

The model given by equations (3)–(7) admits an energy law. Let E(t) denote the total system energy,

$$E(t) = \int_{\Omega} \left(\frac{1}{2} \rho \mathbf{u} \cdot \mathbf{u} + F(\phi, \nabla \phi) + \frac{1}{2} \mathbf{D} \cdot \mathbf{E} \right) d\Omega + \int_{\partial \Omega_s} \Theta(\phi) dS.$$
 (13)

Here Ω and $\partial\Omega_s$ denote the flow domain and the solid domain boundary, respectively. $F(\phi, \nabla\phi)$ is the free energy density function defined in (9). The term $\frac{1}{2}\mathbf{D} \cdot \mathbf{E}$ represents the quasi-static electric energy of the system [43]. $\Theta(\phi)$ is a wall energy density function, whose form is given later, aiming to take into account the contact angle effect.

Taking the time derivative of (13) and using equations (3)–(9) and equation (107c) in the appendix lead to the following energy balance equation,

$$\frac{dE}{dt} = -\int_{\Omega} \gamma_{1} \left| \frac{1}{2} (\rho_{1} - \rho_{2}) \nabla \left(\frac{\partial F}{\partial \phi} - \nabla \cdot \frac{\partial F}{\partial \nabla \phi} - \frac{\epsilon'}{2} \mathbf{E} \cdot \mathbf{E} \right) \right|^{2} - \int_{\Omega} \mu \|\nabla \mathbf{u}\|^{2}
- \int_{\partial \Omega} \left[\left(\frac{\partial F}{\partial \phi} - \nabla \cdot \frac{\partial F}{\partial \nabla \phi} - \frac{\epsilon'}{2} \mathbf{E} \cdot \mathbf{E} \right) \frac{\rho_{1} - \rho_{2}}{2} - \frac{1}{2} (\mathbf{u} \cdot \mathbf{u}) \right] (\tilde{\mathbf{J}} \cdot \mathbf{n})
+ \int_{\partial \Omega} \left[\mu \nabla \mathbf{u} \cdot \mathbf{n} - F \mathbf{n} - \frac{1}{2} (\mathbf{u} \cdot \mathbf{u}) \mathbf{n} \right] \cdot \mathbf{u} - \int_{\partial \Omega} \lambda (\mathbf{n} \cdot \nabla \phi) \frac{\partial \phi}{\partial t} + \int_{\partial \Omega_{s}} \Theta'(\phi) \frac{\partial \phi}{\partial t} - \int_{\partial \Omega} (\mathbf{E} \times \mathbf{H}) \cdot \mathbf{n}, \tag{14}$$

where $\partial\Omega$ denotes the boundary of Ω and $\partial\Omega_s\subset\partial\Omega$ is the solid portion of $\partial\Omega$. The model ensures the dissipativeness of the volume integral terms on the right hand side (RHS). Whether the boundary integral terms are dissipative depends on the imposed boundary conditions, which can guide the choice for the appropriate forms of boundary conditions. The term $\mathbf{E}\times\mathbf{H}$ is the Poynting vector, representing the electromagnetic energy flux to the system [36].

2.4 Equilibrium Solution

The incorporation of the electric field term into the chemical potential and the choice of the $\epsilon(\phi)$ form in (2) (see also Remark 2.2) play an important role in our model. It allows us to derive the energy inequality, thus leading to a thermodynamically consistent model. It also enables us to compute the equilibrium state (steady state) of the two-phase dielectric system by using essentially the phase field equation only, instead of using the full system coupled with the Navier-Stokes equations. We note that in some other studies (e.g. [44, 75]), where the electric field term is absent from the chemical potential, this benefit does not exist and one needs to solve the full set of governing equations in time in order to find the steady state of the problem.

Specifically, the simpler method for computing the equilibrium solution to the current model is as follows. At equilibrium $(\frac{\partial}{\partial t} = 0)$, the model represented by the equations (3)–(7) admits the following solution,

$$\phi_s(\mathbf{x}), P_s(\mathbf{x}), V_s(\mathbf{x}), \text{ and } \mathbf{u}_s(\mathbf{x}) \equiv 0,$$
 (15)

variable	normalization constant	variable	normalization constant
x, y, z, η, d	L_0	V	V_d
$\epsilon,\epsilon_1,\epsilon_2$	ϵ_0	μ, μ_1, μ_2	μ_0
\mathbf{u}	$u_0 = \frac{\epsilon_0 V_d^2}{L_0 \mu_0}$	\mathcal{P}, P, p	$\rho_0 u_0^2$
$ ho, ho_1, ho_2$	$u_0 = \frac{\frac{c_0 v_d}{L_0 \mu_0}}{\frac{\mu_0^2}{\epsilon_0 V_d^2}}$ L_0^2 / μ_0	λ	$\epsilon_0 V_d^2$
γ_1	L_0^2/μ_0	\mathbf{E}	$V_d/L_0 = rac{L_0^2 \mu_0}{2}$
ϕ, ψ	1	$t, \Delta t$	$\frac{L_0^2 \mu_0}{\epsilon_0 V_d^2}$

Table 1: Normalization constants for variables and parameters. Choose $L_0, \epsilon_0, V_d, \mu_0$.

where

$$\gamma_1 \Delta \left[\lambda h(\phi_s) - \lambda \Delta \phi_s - \frac{\epsilon'(\phi_s)}{2} \mathbf{E} \cdot \mathbf{E} \right] = 0, \tag{16a}$$

$$\nabla \mathcal{P}_s - \nabla \cdot (\lambda \phi_s \otimes \nabla \phi_s) - \frac{\nabla \epsilon}{2} (\mathbf{E} \cdot \mathbf{E}) = 0, \tag{16b}$$

$$\nabla \cdot (\epsilon \nabla V_s) = 0, \tag{16c}$$

$$\mathbf{E} = \nabla V_s. \tag{16d}$$

It is important to note that the equilibrium state of the current model is compatible with the zero velocity $(\mathbf{u} = 0)$ requirement based on physics. In the presence of an external electric field, the $(\mathbf{E} \cdot \mathbf{E})$ term in (16a) will cause the equilibrium configuration of the fluid interface to deviate from that of the case with no electric field (e.g. circular or spherical, due to the surface tension).

These characteristics of the current model suggest that we can employ an alternative system to compute the steady-state solution. We replace equation (16a) by the following Cahn-Hilliard equation,

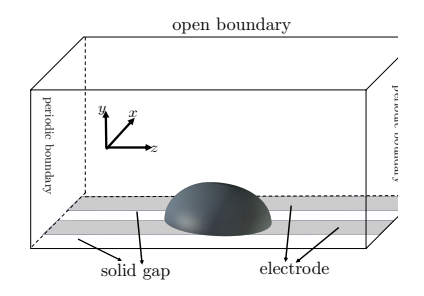
$$\frac{\partial \phi_s}{\partial \tau} = \gamma_1 \Delta \left(\lambda h(\phi_s) - \lambda \Delta \phi_s - \frac{\epsilon'}{2} \mathbf{E} \cdot \mathbf{E} \right), \tag{17}$$

where τ is a pseudo-time. We solve the system consisting of equations (17) and (16c)–(16d) by some time marching scheme until the steady state is reached. This in principle will produce the equilibrium solution to the original model consisting of (3)–(7), with $\mathbf{u}_s = 0$ and \mathcal{P}_s computed by using (16b). The alternative system consisting of (17) and (16c)–(16d) is simpler and faster to compute than the original full system consisting of equations (3)–(7). We will demonstrate the effectiveness of this simpler method for computing the equilibrium solution in Section 4 using numerical simulations, and also compare the results obtained using the simpler method and using the full model consisting of equations (3)–(7).

2.5 Normalization, Computational Domain, and Boundary/Initial Conditions

In numerical simulations we employ the normalized non-dimensional form of the governing equations. The normalization discussed here is for the full model (3)–(7). We employ a somewhat different normalization for the simpler steady-state model consisting of equations (16a)–(16d), which will be specified in a later section. Let L_0 denote a characteristic length scale, V_d a characteristic electric potential, μ_0 a characteristic dynamic viscosity, and ϵ_0 the vacuum permittivity with $\epsilon_0 = 8.85418781 \times 10^{-12} A^2 \cdot s^4/(kg \cdot m^3)$. Table 1 lists the normalization constants for different variables and parameters. For example, the normalized λ is given by $\frac{\lambda}{\epsilon_0 V_d^2}$ according to this table. The normalized governing equations have the same form as the original dimensional ones, and they are also given by the equations (3)–(7). Henceforth, the variables and parameters appearing in the equations (and boundary/initial conditions) are understood to have been normalized appropriately, and we will not differentiate their dimensional and non-dimensional forms.

We perform two-phase dielectric flow simulations in both 2D and 3D. The flow domain and the settings considered here largely follow those of the experiments by McHale, Brown and collaborators [54, 9, 8]. Especially we assume that in 3D the domain has at least one homogeneous direction, so that Fourier expansions can be performed along that direction. Figure 1 shows typical flow domains and configurations for 2D and 3D. We are interested in the deformation or motion of dielectric droplets on a solid wall. A regular array



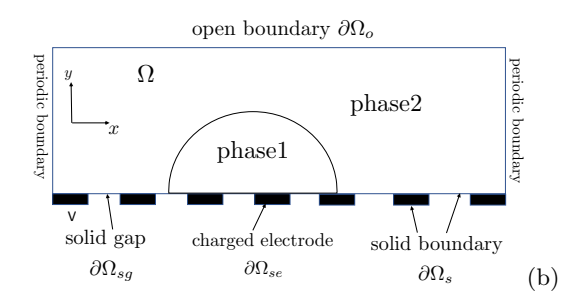


Figure 1: Typical flow domain and settings for (a) 3D and (b) 2D. On the bottom wall, the gray stripes denote the electrodes and the white stripes denote the gap between the electrodes.

of parallel electrodes (gray stripes in plot (a), or the dark regions in plot(b)) are embedded on the bottom wall, stretching along the z direction for 3D. The electrodes are separated by wall surfaces (white stripes in plot (a), or white regions in plot (b)). The top of the flow domain is open, while in the horizontal directions the flow is assumed to be periodic.

Let $\partial\Omega_o$ denote the open boundary on the top, $\partial\Omega_{se}$ ("se" standing for solid-electrode) denote the region of electrodes on the bottom wall, and $\partial\Omega_{sg}$ ("sg" standing for solid-gap) denote the gap region between the electrodes on the wall. The bottom wall constitutes the solid domain boundary $\partial\Omega_s$, with $\partial\Omega_s = \partial\Omega_{se} \cup \partial\Omega_{sg}$.

We employ periodic conditions for all the field variables in the horizontal directions and the following boundary conditions for the top and bottom sides of the domain:

Top open boundary $\partial\Omega_o$:

(phase field eq.)
$$\begin{cases} \mathbf{n} \cdot \nabla \left(\lambda h(\phi) - \lambda \Delta \phi - \frac{\epsilon'}{2} \mathbf{E} \cdot \mathbf{E} \right) = 0, & on \quad \partial \Omega_o \\ \nabla \phi \cdot \mathbf{n} = 0, & on \quad \partial \Omega_o. \end{cases}$$
 (18)

(momentum eq.)
$$\frac{\partial \mathbf{u}}{\partial n} = 0$$
, $P = 0$, on $\partial \Omega_o$. (19)

(electric potential)
$$\frac{\partial V}{\partial n} = 0$$
, on $\partial \Omega_o$. (20)

Bottom wall $(\partial \Omega_{se} \cup \partial \Omega_{sq} = \partial \Omega_s)$:

(phase field eq.)
$$\begin{cases} \mathbf{n} \cdot \nabla \left(\lambda h(\phi) - \lambda \Delta \phi - \frac{\epsilon'}{2} \mathbf{E} \cdot \mathbf{E} \right) = 0, & on \quad \partial \Omega_s \\ \lambda \nabla \phi \cdot \mathbf{n} + \Theta'(\phi) = 0, & on \quad \partial \Omega_s \end{cases}$$
 (21)

(momentum eq.)
$$\mathbf{u} = \mathbf{0}$$
, on $\partial \Omega_s$, (22)

(electric potential)
$$\begin{cases} \frac{\partial V}{\partial n} = 0, & on \quad \partial \Omega_{sg} \\ V = \mathcal{V}_e, & on \quad \partial \Omega_{se}. \end{cases}$$
 (23)

In equation (21) $\Theta(\phi)$ denotes the wall energy density function, which accounts for the contact angle effect, given by

$$\Theta(\phi) = \gamma \cos(\theta_s) \frac{\phi(\phi^2 - 3)}{4} + \frac{1}{2} (\gamma_{s1} + \gamma_{s2}). \tag{24}$$

where $\gamma, \gamma_{s1}, \gamma_{s2}$ are interfacial tension between phase1-phase2, phase1-solid and phase2-solid, and θ_s is the static contact angle. This functional form is essentially a Hermite interpolation of interfacial tensions; see [18] for more details. In equation (23) V_e denotes the imposed voltage on the electrodes. We will in general impose an alternate negative/positive voltage on adjacent electrodes as in the experiments (see e.g. [54]). In the gap region between the electrodes, we have employed a simple condition $\frac{\partial V}{\partial n} = 0$. This essentially assumes that the electric field at the wall (gap region) has only a tangent component. Note that this condition is exact if the fluids and the wall have matching permitivities or when the fluid is homogeneous [27]. In more general cases, this boundary condition may not be exactly accurate. We adopt this boundary condition because of its simplicity, and that the simulation results indicate that it can capture the flow physics reasonably well. We note that the set of boundary conditions (18)–(23) is reduction-consistent with $\epsilon(\phi)$ given by (2) and $\Theta(\phi)$ given by (24).

Finally we employ the following initial conditions,

$$\mathbf{u}(\mathbf{x}, t = 0) = \mathbf{u}_0(\mathbf{x}),\tag{25}$$

$$\phi(\mathbf{x}, t = 0) = \phi_0(\mathbf{x}),\tag{26}$$

where \mathbf{u}_0 and ϕ_0 denote the initial distributions for the velocity and the phase field function.

3 Numerical Algorithm

3.1 Algorithm Formulation

The system consisting of the equations (3)–(7), the boundary conditions (18)–(23) and the periodic conditions along the horizontal directions, and the initial conditions (25)–(26) constitute the initial/boundary value problem we need to solve for the velocity, pressure, phase field, and the electric potential.

For the purpose of numerical testing, we modify some of the equations and boundary conditions slightly by adding certain prescribed source terms. These source terms are useful for testing the convergence of the method using manufactured solutions, and they will be set to zero in actual flow simulations. Specifically, we re-write equations (3), (4) and (6) into,

$$\frac{\partial \phi}{\partial t} + \mathbf{u} \cdot \nabla \phi = \gamma_1 \Delta \left(\lambda h(\phi) - \lambda \Delta \phi - \frac{\epsilon'}{2} \mathbf{E} \cdot \mathbf{E} \right) + g(\mathbf{x}, t), \tag{27}$$

$$\frac{\partial \mathbf{u}}{\partial t} + \mathbf{N}(\mathbf{u}) + \frac{1}{\rho} \tilde{\mathbf{J}} \cdot \nabla \mathbf{u} = -\frac{\lambda}{\rho} \nabla^2 \phi \nabla \phi - \frac{\epsilon'}{2\rho} (\mathbf{E} \cdot \mathbf{E}) \nabla \phi + \frac{\mu}{\rho} \nabla^2 \mathbf{u} + \frac{1}{\rho} \nabla \mu \cdot \mathcal{D}(\mathbf{u}) - \frac{1}{\rho} \nabla P + \frac{1}{\rho} \mathbf{f}(\mathbf{x}, t) \quad (28)$$

$$\nabla \cdot (\epsilon V) = f_V(\mathbf{x}, t), \tag{29}$$

where g, \mathbf{f} and f_V are prescribed source terms, and

$$P = \mathcal{P} + \frac{\lambda}{2} \nabla \phi \cdot \nabla \phi, \quad \mathcal{D}(\mathbf{u}) = \nabla \mathbf{u} + \nabla \mathbf{u}^T, \quad \mathbf{N}(\mathbf{u}) = \mathbf{u} \cdot \nabla \mathbf{u}.$$
(30)

The boundary conditions (18)–(19) are modified as,

$$\mathbf{n} \cdot \nabla \left(\lambda h(\phi) - \lambda \nabla^2 \phi - \frac{1}{2} \epsilon' \mathbf{E}^2 \right) = g_1(x, t), \quad \mathbf{n} \cdot \nabla \phi = g_2(\mathbf{x}, t), \quad \mathbf{x} \in \partial \Omega_o;$$
 (31)

$$\frac{\partial \mathbf{u}}{\partial n} = \mathbf{f}_1(\mathbf{x}, t), \quad P = f_2(\mathbf{x}, t), \quad \mathbf{x} \in \partial \Omega_o;$$
(32)

where \mathbf{f}_1 , f_2 , g_1 , g_2 are prescribed source terms. The boundary conditions (21)–(22) are modified as,

$$\mathbf{n} \cdot \nabla \left(\lambda h(\phi) - \lambda \nabla^2 \phi - \frac{1}{2} \epsilon' \mathbf{E}^2 \right) = g_1(x, t), \quad \mathbf{n} \cdot \nabla \phi + \frac{1}{\lambda} \Theta'(\phi) = g_3(\mathbf{x}, t), \quad \mathbf{x} \in \partial \Omega_s;$$
 (33)

$$\mathbf{u} = \mathbf{w}(\mathbf{x}, t), \quad \mathbf{x} \in \partial \Omega_s;$$
 (34)

where g_3 and **w** are prescribed source terms.

We next present an algorithm for solving the system consisting of equations (27)–(29), (5), (7), (31)–(34), (20), (23), together with the periodic conditions in the horizontal directions. Let $n \ge 0$ denote the time step index, Δt denote the time step size, and $(\cdot)^n$ denote the variable (\cdot) at time step n. Given $(\mathbf{u}^n, P^n, \phi^n, V^n)$, we compute these quantities at step (n+1) successively by the following procedure:

Electric potential V^{n+1} and electric field \mathbf{E}^{n+1} :

$$\nabla \cdot (\varepsilon_0 \nabla V^{n+1}) = f_V^{n+1} - \nabla \cdot \left[(\epsilon(\phi^{*,n+1}) - \varepsilon_0) \nabla V^{*,n+1} \right], \tag{35a}$$

$$\frac{\partial V^{n+1}}{\partial n} = 0, \quad \text{on } \partial \Omega_o \cup \partial \Omega_{sg}, \tag{35b}$$

$$V^{n+1} = \mathcal{V}_e$$
, on $\partial \Omega_{se}$, (35c)

$$\mathbf{E}^{n+1} = \nabla V^{n+1}.\tag{35d}$$

Phase field ϕ^{n+1} :

$$\frac{\gamma_0 \phi^{n+1} - \hat{\phi}}{\Delta t} + \nabla \cdot (\mathbf{u}^{*,n+1} \phi^{*,n+1}) = -\lambda \gamma_1 \nabla^2 \left[\nabla^2 \phi^{n+1} - \frac{S}{\eta^2} (\phi^{n+1} - \phi^{*,n+1}) - h(\phi^{*,n+1}) + \frac{\epsilon'(\phi^{*,n+1})}{2\lambda} \left| \mathbf{E}^{n+1} \right|^2 \right] + g^{n+1},$$
(36a)

$$\mathbf{n} \cdot \nabla \left[\nabla^2 \phi^{n+1} - \frac{S}{\eta^2} (\phi^{n+1} - \phi^{*,n+1}) - h(\phi^{*,n+1}) + \frac{\epsilon'(\phi^{*,n+1})}{2\lambda} \left| \mathbf{E}^{n+1} \right|^2 \right] = g_1^{n+1}, \text{ on } \partial\Omega_o \cup \partial\Omega_s, \quad (36b)$$

$$\mathbf{n} \cdot \nabla \phi^{n+1} = g_2^{n+1}, \text{ on } \partial \Omega_o,$$
 (36c)

$$-\mathbf{n} \cdot \nabla \phi^{n+1} - \frac{\Theta'(\phi^{*,n+1})}{\lambda} = g_3^{n+1}, \text{ on } \partial \Omega_s.$$
(36d)

Pressure P^{n+1} :

$$\frac{\gamma_{0}\tilde{\mathbf{u}}^{n+1} - \hat{\mathbf{u}}}{\Delta t} + \frac{1}{\rho_{0}}\nabla P^{n+1} = -\mathbf{N}(\mathbf{u}^{*,n+1}) + \left(\frac{1}{\rho_{0}} - \frac{1}{\rho^{n+1}}\right)\nabla P^{*,n+1} - \frac{\mu^{n+1}}{\rho^{n+1}}\nabla \times \nabla \times \mathbf{u}^{*,n+1} \\
+ \frac{1}{\rho^{n+1}}\nabla \mu^{n+1} \cdot \mathcal{D}(\mathbf{u}^{*,n+1}) - \frac{\lambda}{\rho^{n+1}}\nabla^{2}\phi^{n+1}\nabla\phi^{n+1} + \frac{f^{n+1}}{\rho^{n+1}} \\
- \frac{1}{\rho^{n+1}}\tilde{\mathbf{J}}^{n+1} \cdot \nabla \mathbf{u}^{*,n+1} - \frac{\epsilon'(\phi^{n+1})}{2\rho^{n+1}}\left|\mathbf{E}^{n+1}\right|^{2}\nabla\phi^{n+1}, \tag{37a}$$

$$\nabla \cdot \tilde{\mathbf{u}}^{n+1} = 0, \tag{37b}$$

$$\frac{\partial \tilde{\mathbf{u}}^{n+1}}{\partial n} = \mathbf{f}_1^{n+1}, \text{ on } \partial \Omega_o, \tag{37c}$$

$$P^{n+1} = f_2^{n+1}$$
, on $\partial \Omega_o$, (37d)

$$\tilde{\mathbf{u}}^{n+1} \cdot \mathbf{n} = \mathbf{w}^{n+1} \cdot \mathbf{n}$$
, on $\partial \Omega_s$. (37e)

Velocity \mathbf{u}^{n+1} :

$$\frac{\gamma_{0}\mathbf{u}^{n+1} - \hat{\mathbf{u}}}{\Delta t} + \frac{1}{\rho_{0}}\nabla P^{n+1} - \nu_{m}\nabla^{2}\mathbf{u}^{n+1} = -\mathbf{N}(\mathbf{u}^{*,n+1}) + \left(\frac{1}{\rho_{0}} - \frac{1}{\rho^{n+1}}\right)\nabla P^{*,n+1} \\
+ \left(\nu_{m} - \frac{\mu^{n+1}}{\rho^{n+1}}\right)\nabla \times \nabla \times \mathbf{u}^{*,n+1} + \frac{1}{\rho^{n+1}}\nabla \mu^{n+1} \cdot \mathcal{D}(\mathbf{u}^{*,n+1}) - \frac{\lambda}{\rho^{n+1}}\nabla^{2}\phi^{n+1}\nabla\phi^{n+1} \\
+ \frac{f^{n+1}}{\rho^{n+1}} - \frac{1}{\rho^{n+1}}\tilde{\mathbf{J}}^{n+1} \cdot \nabla \mathbf{u}^{*,n+1} - \frac{\epsilon'(\phi^{n+1})}{2\rho^{n+1}} \left| \mathbf{E}^{n+1} \right|^{2}\nabla\phi^{n+1} \tag{38a}$$

$$\frac{\partial \mathbf{u}^{n+1}}{\partial n} = \mathbf{f}_1^{n+1}, \text{ on } \partial \Omega_o, \tag{38b}$$

$$\mathbf{u}^{n+1} = \mathbf{w}^{n+1}$$
, on $\partial \Omega_s$. (38c)

In the horizontal directions (x in 2D, x and z in 3D) we impose periodic conditions for (V^{n+1} , ϕ^{n+1} , P^{n+1} , \mathbf{u}^{n+1}). These periodic conditions are not explicitly included in the above system of equations.

The symbols in the above equations have the following meanings. $\tilde{\mathbf{J}}^{n+1}$ in (37a) and (38a) is given by,

$$\tilde{\mathbf{J}}^{n+1} = \frac{1}{2} (\rho_1 - \rho_2) \lambda \gamma_1 \nabla \left[\nabla^2 \phi^{n+1} - \frac{S}{\eta^2} (\phi^{n+1} - \phi^{*,n+1}) - h(\phi^{*,n+1}) + \frac{\epsilon'(\phi^{*,n+1})}{2\lambda} |\mathbf{E}^{n+1}|^2 \right], \tag{39}$$

in which S is a stabilization parameter to be described later. $\tilde{\mathbf{u}}^{n+1}$ is an auxiliary approximation of \mathbf{u} at time step (n+1). Let ξ denote a generic variable. Then in the above equations the expression $\frac{1}{\Delta t}D\xi^{n+1} =$

 $\frac{1}{\Delta t}(\gamma_0 \xi^{n+1} - \hat{\xi})$ represents an approximation of $\frac{\partial \xi}{\partial t}\Big|^{n+1}$ by the *J*-th order backward differentiation formula (BDF), where J = 1 or 2, and $\xi^{*,n+1}$ represents a *J*-th order explicit approximation of ξ^{n+1} . They are explicitly given by,

$$D\xi^{n+1} = \begin{cases} \xi^{n+1} - \xi^n, & \text{if } J = 1, \\ \frac{3}{2}\xi^{n+1} - 2\xi^n + \frac{1}{2}\xi^{n-1}, & \text{if } J = 2; \end{cases} \quad \xi^{*,n+1} = \begin{cases} \xi^n, & \text{if } J = 1, \\ 2\xi^n - \xi^{n-1}, & \text{if } J = 2. \end{cases}$$
(40)

Note that $\gamma_0 = 1$ for J = 1, and $\frac{3}{2}$ for J = 2.

The ε_0 in equation (35a), ρ_0 in (37a), and ν_m in (38a) are constant algorithmic parameters. With those terms involving these constants formulated as above, the algorithm leads to linear algebraic systems with constant and time-dependent coefficient matrices upon discretization, which makes the current method computationally highly efficient. We choose $\varepsilon_0 = \max(\epsilon_1, \epsilon_2)$, where ϵ_1, ϵ_2 are permittivities of the dielectric fluids. In (35a) we have treated the $\varepsilon_0 \nabla V$ term on the left hand side (LHS) implicitly and the correction term $(\epsilon - \varepsilon_0) \nabla V$ in the RHS explicitly. The consistent approximation of these terms ensures the *J*-th order accuracy of the overall scheme. We choose ρ_0 and ν_m following [24, 20], specifically with $\rho_0 = \min(\rho_1, \rho_2)$ and $\nu_m \geq \frac{1}{2} \frac{\max(\mu_1, \mu_2)}{\min(\rho_1, \rho_2)}$, where ρ_1 and ρ_2 are the densities, and μ_1 and μ_2 are the dynamic viscosities of two dielectric fluids, respectively. We note the approach using the Helmholtz-Hodge decomposition for dealing with the variable density in [13, 4, 15].

The term $\frac{S}{\eta^2}(\phi^{n+1} - \phi^{*,n+1})$ in equation (36a) is a stabilization term, where S is a chosen constant satisfying $S \geq \eta^2 \sqrt{\frac{4\gamma_0}{\lambda\gamma_1\Delta t}}$. This allows us to reformulate the fourth order Cahn-Hilliard equation into two decoupled Helmholtz type equations (see [18] for more details). Note that the convective term of the phase field equation is written into the conservative form in the discretized equation (36a). This form ensures the conservation of the integral of the phase field function on the discrete level (see Remark 3.2 below).

Remark 3.1 In the above algorithm we need to compute the initial distribution of the electric potential (and the electric field) to start the computation, i.e. solving for $V(\mathbf{x}, t = 0) = V_0(\mathbf{x})$. We use a fixed point iteration to compute the initial distribution.

$$\nabla \cdot \left(\varepsilon_0 \nabla V^{(k+1)}\right) = f_V^{ini} - \nabla \cdot \left[(\epsilon(\phi_0) - \varepsilon_0) \nabla V^{(k)} \right], \tag{41}$$

where ϕ_0 is the initial phase field distribution given in (27), $f_V^{ini} = f_V(\mathbf{x}, t = 0)$, and the superscript in $V^{(k)}$ refers to the iteration index. The electric potential distribution is obtained upon convergence of this iteration.

3.2 Implementation and Spatial Discretization

We next discuss how to implement the algorithm represented by equations (35a)–(38c) using high-order C^0 spectral elements in 2D and a hybrid Fourier spectral/spectral-element method in 3D. We first derive a weak form of the algorithm, which is suitable for both 2D and 3D. Then we further transform the weak form in 3D to a form specifically for the hybrid Fourier spectral/spectral-element discretization.

Given $(\mathbf{u}^n, P^n, \phi^n, V^n)$, we wish to compute $(\mathbf{u}^{n+1}, P^{n+1}, \phi^{n+1}, V^{n+1})$. We will first derive the weak forms about these variables in the continuous space by taking the L^2 inner product between an arbitrary test function and the equations about these variables. Then we restrict these variables and the test functions to appropriate function spaces to attain the final weak forms.

Let $e(\mathbf{x})$ denote an arbitrary test function. Taking the L^2 inner product between e and (35a) and using the integration by parts, we attain the weak form for V^{n+1} ,

$$\int_{\Omega} \varepsilon_0 \nabla V^{n+1} \cdot \nabla e = -\int_{\Omega} (\epsilon(\phi^{*,n+1}) - \varepsilon_0) \nabla V^{*,n+1} \cdot \nabla e - \int_{\Omega} f_V^{n+1} e, \quad \forall e.$$
 (42)

The weak form of the electric field $\mathbf{E}^{n+1}(\mathbf{x}) = (E_x^{n+1}(\mathbf{x}), E_y^{n+1}(\mathbf{x}), E_z^{n+1}(\mathbf{x}))$ is obtained by taking the L^2 inner product between $e(\mathbf{x})$ and equation (35d),

$$\int_{\Omega} \mathbf{E}^{n+1} e = \int_{\Omega} \nabla V^{n+1} e, \quad \forall e. \tag{43}$$

Equation (36a) can be written as (see [24] for details),

$$\nabla^2 \psi^{n+1} - \left(\alpha + \frac{S}{\eta^2}\right) \psi^{n+1} = Q_1 + \nabla^2 Q_2, \tag{44a}$$

$$\nabla^2 \phi^{n+1} + \alpha \phi^{n+1} = \psi^{n+1},\tag{44b}$$

where $\alpha = -\frac{S}{2\eta^2} \left(1 + \sqrt{1 - \frac{4\gamma_0}{\lambda\gamma_1\Delta t} \frac{\eta^4}{S^2}}\right)$, ψ^{n+1} is an auxiliary variable defined by (44b), and

$$Q_{1} = \frac{1}{\lambda \gamma_{1}} \left(g^{n+1} - \nabla \cdot (\mathbf{u}^{*,n+1} \phi^{*,n+1}) + \frac{\hat{\phi}}{\Delta t} \right), \quad Q_{2} = h(\phi^{*,n+1}) - \frac{S}{\eta^{2}} \phi^{*,n+1} - \frac{\epsilon'(\phi^{*,n+1})}{2\lambda} |\mathbf{E}^{n+1}|^{2}.$$
(45)

Let $\omega(\mathbf{x})$ denote an arbitrary test function. The weak forms for (44a) and (44b) are attained by taking the L^2 inner product between $\omega(\mathbf{x})$ and these equations,

$$\int_{\Omega} \nabla \psi^{n+1} \cdot \nabla \omega + \left(\alpha + \frac{S}{\eta^2}\right) \int_{\Omega} \psi^{n+1} \cdot \omega = \int_{\partial \Omega_o} \left[g_1^{n+1} + \left(\alpha + \frac{S}{\eta^2}\right) g_2^{n+1} \right] \omega
+ \int_{\partial \Omega_s} \left[g_1^{n+1} + \left(\alpha + \frac{S}{\eta^2}\right) \left(-g_3^{n+1} - \frac{\Theta'(\phi^{*,n+1})}{\lambda} \right) \right] \omega - \int_{\Omega} Q_1 \omega + \int_{\Omega} \nabla Q_2 \cdot \nabla \omega, \quad \forall \omega; \quad (46)$$

$$\int_{\Omega} \nabla \phi^{n+1} \cdot \nabla \omega - \alpha \int_{\Omega} \phi^{n+1} \omega = \int_{\partial \Omega_o} g_2^{n+1} \omega + \int_{\partial \Omega_s} \left[-g_3^{n+1} - \frac{\Theta'(\phi^{*,n+1})}{\lambda} \right] \omega - \int_{\Omega} \psi^{n+1} \omega, \quad \forall \omega. \quad (47)$$

Let $q(\mathbf{x})$ denote an arbitrary test function that vanishes on $\partial\Omega_o$. Taking the L^2 inner product between ∇q and equation (37a) leads to the weak form about P^{n+1} ,

$$\int_{\Omega} \nabla P^{n+1} \cdot \nabla q = \rho_0 \int_{\Omega} \left[\mathbf{T} + \nabla \left(\frac{\mu^{n+1}}{\rho^{n+1}} \right) \times \boldsymbol{\omega}^{*,n+1} \right] \cdot \nabla q
- \rho_0 \int_{\partial \Omega} \frac{\mu^{n+1}}{\rho^{n+1}} \mathbf{n} \times \boldsymbol{\omega}^{*,n+1} \cdot \nabla q - \frac{\rho_0 \gamma_0}{\Delta t} \int_{\partial \Omega_s} \mathbf{n} \cdot \mathbf{w}^{n+1} q, \quad \forall q \text{ with } q |_{\partial \Omega_o} = 0, \quad (48)$$

where $\boldsymbol{\omega} = \nabla \times \mathbf{u}$ and

$$\mathbf{T} = \frac{1}{\rho^{n+1}} \left[f^{n+1} - \lambda (\psi^{n+1} - \alpha \phi^{n+1}) \nabla \phi^{n+1} - \frac{\epsilon'(\phi^{n+1})}{2} |\mathbf{E}|^2 \nabla \phi^{n+1} + \nabla \mu^{n+1} \cdot \mathcal{D}(\mathbf{u}^{*,n+1}) \right.$$
$$\left. - \tilde{\mathbf{J}}^{n+1} \cdot \nabla \mathbf{u}^{*,n+1} \right] + \frac{\hat{u}}{\Delta t} - \mathbf{N}(\mathbf{u}^{*,n+1}) + \left(\frac{1}{\rho_0} - \frac{1}{\rho^{n+1}} \right) \nabla P^{*,n+1}. \tag{49}$$

When deriving the above equation, the following identity has been used,

$$\frac{\mu}{\rho} \nabla \times \boldsymbol{\omega} \cdot \nabla q = \nabla \cdot \left(\frac{\mu}{\rho} \boldsymbol{\omega} \times \nabla q \right) - \nabla \left(\frac{\mu}{\rho} \right) \times \boldsymbol{\omega} \cdot \nabla q.$$

For the weak form of equation (38a), let $v(\mathbf{x})$ be an arbitrary test function that vanishes on $\partial\Omega_s$, and we take the L^2 inner product between $v(\mathbf{x})$ and equation (38a) to get

$$\int_{\Omega} \nabla \mathbf{u}^{n+1} \cdot \nabla v + \frac{\gamma_0}{\nu_m \Delta t} \int_{\Omega} \mathbf{u}^{n+1} v = \frac{1}{\nu_m} \int_{\Omega} \left(\mathbf{T} - \frac{1}{\rho_0} \nabla P^{n+1} \right) v - \frac{1}{\nu_m} \int_{\Omega} \left(\frac{\mu^{n+1}}{\rho^{n+1}} - \nu_m \right) \boldsymbol{\omega}^{*,n+1} \times \nabla v \\
+ \frac{1}{\nu_m} \int_{\Omega} \nabla \left(\frac{\mu^{n+1}}{\rho^{n+1}} - \nu_m \right) \times \boldsymbol{\omega}^{*,n+1} v + \int_{\partial \Omega_o} \mathbf{f}_1^{n+1} v - \frac{1}{\nu_m} \int_{\partial \Omega_o} \left(\frac{\mu^{n+1}}{\rho^{n+1}} - \nu_m \right) \mathbf{n} \times \boldsymbol{\omega}^{*,n+1} v, \\
\forall v \text{ with } v|_{\partial \Omega_s} = 0, \tag{50}$$

where the following identity has been used,

$$v\left(\nu_m - \frac{\mu}{\rho}\right) \nabla \times \boldsymbol{\omega} = \nabla \times \left[v\boldsymbol{\omega}\left(\nu_m - \frac{\mu}{\rho}\right)\right] - v\nabla\left(\nu_m - \frac{\mu}{\rho}\right) \times \boldsymbol{\omega} - \left(\nu_m - \frac{\mu}{\rho}\right) \nabla v \times \boldsymbol{\omega}.$$

Remark 3.2 The discretized scheme as given by (42)–(50) conserves the volume integral of the phase field function, i.e.

$$\int_{\Omega} \phi^n d\Omega = \int_{\Omega} \phi^0 d\Omega, \quad \forall n \geqslant 0, \tag{51}$$

provided that there is no external force, only periodic or no-slip (or no penetration) boundary conditions are imposed, and the phase field at the first time step, $\phi^1(\mathbf{x})$, is computed by the first-order scheme (J=1). The relation (51) can be shown to be true by setting $\omega=1$ in (46)-(47), noting $\alpha\left(\alpha+\frac{S}{\eta^2}\right)=-\frac{\gamma_0}{\lambda\gamma_1\Delta t}$, using the divergence theorem and $\mathbf{n}\cdot\mathbf{u}=0$ for no-slip (or no penetration) boundaries, and by induction.

3.2.1 Two Dimensions

For two-dimensional (2D, $\Omega \subset \mathbb{R}^2$) problems we employ C^0 spectral elements for spatial discretizations. We partition the domain Ω using a spectral element mesh. Let Ω_h denote the discretized domain, $\Omega_h = \bigcup_{e=1}^{N_e} \Omega_h^e$, where Ω_h^e ($1 \leq e \leq N_e$) denotes the element e and N_e is the number of elements in the mesh. Let $\partial \Omega_h$, $\partial \Omega_{oh}$, $\partial \Omega_{sh}$ denote the discretized versions of the domain boundary $\partial \Omega$, open boundary $\partial \Omega_o$, and solid boundary $\partial \Omega_s$. Then $\partial \Omega_h = \partial \Omega_{oh} \cup \partial \Omega_{sh} = \partial \Omega_{oh} \cup \partial \Omega_{seh} \cup \partial \Omega_{sgh}$, where $\partial \Omega_{seh}$ and $\partial \Omega_{sgh}$ are the discretized versions of the solid-electrode boundary and the solid-gap boundary, respectively. Let $\Pi_K(\Omega_h^e)$ denote the linear space of polynomials defined on Ω_h^e with their degrees characterized by K (K will be referred to as the element order hereafter). Define

$$\begin{cases}
X_{h} = \{ v \in H^{1}(\Omega_{h}) : v |_{\Omega_{h}^{e}} \in \Pi_{K}(\Omega_{h}^{e}), 1 \leqslant e \leqslant N_{e} \}, \\
X_{h0}^{E} = \{ v \in X_{h} : v |_{\partial\Omega_{seh}} = 0 \}, \\
X_{h0}^{P} = \{ v \in X_{h} : v |_{\partial\Omega_{oh}} = 0 \}, \\
X_{h0}^{u} = \{ v \in X_{h} : v |_{\partial\Omega_{sh}} = 0 \}.
\end{cases}$$
(52)

In what follows we use $(\cdot)_h$ to denote the discretized version of (\cdot) .

The 2D fully discretized equations consists of the following:

For V_h^{n+1} : find $V_h^{n+1} \in X_h$ such that

$$\int_{\Omega_h} \varepsilon_0 \nabla V_h^{n+1} \cdot \nabla e_h = -\int_{\Omega_h} (\epsilon(\phi_h^{*,n+1}) - \varepsilon_0) \nabla V_h^{*,n+1} \cdot \nabla e_h - \int_{\Omega_h} f_{Vh}^{n+1} e_h, \quad \forall e_h \in X_{h0}^E;$$
 (53a)

$$V_h^{n+1} = \mathcal{V}_e, \quad \text{on } \partial\Omega_{seh}.$$
 (53b)

For \mathbf{E}_h^{n+1} : find $\mathbf{E}_h^{n+1} \in [X_h]^2$ such that

$$\int_{\Omega_h} \mathbf{E}_h^{n+1} e_h = \int_{\Omega_h} \nabla V_h^{n+1} e_h, \quad \forall e_h \in X_h.$$
 (54)

Algorithm 1: Solution Procedure within a Time Step for 2D Dielectric Flows

 $\begin{array}{ll} \textbf{input} \ : V^n, \, \phi^n, \, P^n, \, \mathbf{u}^n. \\ \textbf{output:} \ V^{n+1}, \, \mathbf{E}^{n+1}, \, \psi^{n+1}, \, \phi^{n+1}, \, P^{n+1}, \, \mathbf{u}^{n+1}. \end{array}$

- 1 solve equations (53a)–(53b) for V^{n+1}
- **2** solve equation (54) for \mathbf{E}^{n+1}
- **3** solve equation (55) for ψ^{n+1}
- **4** solve equation (56) for ϕ^{n+1}
- **5** solve equations (57a)–(57b) for P^{n+1}
- 6 solve equations (58a)–(58b) for \mathbf{u}^{n+1}

For ψ_h^{n+1} : find $\psi_h^{n+1} \in X_h$ such that

$$\int_{\Omega_{h}} \nabla \psi_{h}^{n+1} \cdot \nabla \omega_{h} + \left(\alpha + \frac{S}{\eta^{2}}\right) \int_{\Omega_{h}} \psi_{h}^{n+1} \cdot \omega_{h} = \int_{\partial \Omega_{oh}} \left[g_{1h}^{n+1} + \left(\alpha + \frac{S}{\eta^{2}}\right) g_{2h}^{n+1}\right] \omega_{h}
+ \int_{\partial \Omega_{sh}} \left[g_{1h}^{n+1} + \left(\alpha + \frac{S}{\eta^{2}}\right) \left(-g_{3h}^{n+1} - \frac{\Theta'(\phi_{h}^{*,n+1})}{\lambda}\right)\right] \omega_{h} - \int_{\Omega_{h}} Q_{1h} \omega_{h} + \int_{\Omega_{h}} \nabla Q_{2h} \cdot \nabla \omega_{h},
\forall \omega_{h} \in X_{h}.$$
(55)

For ϕ_h^{n+1} : find $\phi_h^{n+1} \in X_h$ such that

$$\int_{\Omega_{h}} \nabla \phi_{h}^{n+1} \cdot \nabla \omega_{h} - \alpha \int_{\Omega_{h}} \phi_{h}^{n+1} \omega_{h} = \int_{\partial \Omega_{oh}} g_{2h}^{n+1} \omega_{h} + \int_{\partial \Omega_{sh}} \left[-g_{3h}^{n+1} - \frac{\Theta'(\phi_{h}^{*,n+1})}{\lambda} \right] \omega_{h} - \int_{\Omega_{h}} \psi_{h}^{n+1} \omega_{h}, \quad \forall \omega_{h} \in X_{h}.$$
(56)

For P_h^{n+1} : find $P_h^{n+1} \in X_h$ such that

$$\int_{\Omega_{h}} \nabla P_{h}^{n+1} \cdot \nabla q_{h} = \rho_{0} \int_{\Omega_{h}} \left[\mathbf{T}_{h} + \nabla \left(\frac{\mu_{h}^{n+1}}{\rho_{h}^{n+1}} \right) \times \boldsymbol{\omega}_{h}^{*,n+1} \right] \cdot \nabla q_{h} \\
- \rho_{0} \int_{\partial\Omega_{h}} \frac{\mu_{h}^{n+1}}{\rho_{h}^{n+1}} \mathbf{n} \times \boldsymbol{\omega}_{h}^{*,n+1} \cdot \nabla q_{h} - \frac{\rho_{0} \gamma_{0}}{\Delta t} \int_{\partial\Omega_{sh}} \mathbf{n} \cdot \mathbf{w}_{h}^{n+1} q_{h}, \quad \forall q_{h} \in X_{h0}^{P}.$$
(57a)

$$P_h^{n+1} = f_{2h}^{n+1}$$
, on $\partial \Omega_{oh}$. (57b)

For \mathbf{u}_h^{n+1} : find $\mathbf{u}_h^{n+1} \in [X_h]^2$ such that

$$\int_{\Omega_{h}} \nabla v_{h} \cdot \nabla \mathbf{u}_{h}^{n+1} + \frac{\gamma_{0}}{\nu_{m} \Delta t} \int_{\Omega_{h}} \mathbf{u}_{h}^{n+1} v_{h} = \frac{1}{\nu_{m}} \int_{\Omega_{h}} \left(\mathbf{T}_{h} - \frac{1}{\rho_{0}} \nabla P_{h}^{n+1} \right) v_{h}
- \frac{1}{\nu_{m}} \int_{\Omega_{h}} \left(\frac{\mu_{h}^{n+1}}{\rho_{h}^{n+1}} - \nu_{m} \right) \boldsymbol{\omega}_{h}^{*,n+1} \times \nabla v_{h} + \frac{1}{\nu_{m}} \int_{\Omega_{h}} \nabla \left(\frac{\mu_{h}^{n+1}}{\rho_{h}^{n+1}} \right) \times \boldsymbol{\omega}_{h}^{*,n+1} v_{h} + \int_{\partial \Omega_{oh}} \mathbf{f}_{1h}^{n+1} v_{h}
- \frac{1}{\nu_{m}} \int_{\partial \Omega_{oh}} \left(\frac{\mu_{h}^{n+1}}{\rho_{h}^{n+1}} - \nu_{m} \right) \mathbf{n} \times \boldsymbol{\omega}_{h}^{*,n+1} v_{h}, \quad \forall v_{h} \in X_{h0}^{u};$$
(58a)
$$\mathbf{u}_{h}^{n+1} = \mathbf{w}_{h}^{n+1}, \text{ on } \partial \Omega_{sh}.$$
(58b)

Therefore, given $(\mathbf{u}^n, P^n, \phi^n, V^n)$, one can compute V^{n+1} , \mathbf{E}^{n+1} , ψ^{n+1} , ϕ^{n+1} , P^{n+1} and \mathbf{u}^{n+1} by solving equations (53a)–(58b) successively in an uncoupled fashion. The solution procedure is summarized in Algorithm 1.

3.2.2 Three Dimensions

For three dimensions (3D, $\Omega \subset \mathbb{R}^3$) we concentrate on problems with one homogeneous direction in this work, so that Fourier expansions can be employed along that direction, as stated previously. Let us assume that

the homogeneous direction is along the z axis, and we employ a hybrid spectral-element/Fourier spectral discretization to solve the problem, with spectral element discretization in the xy plane and Fourier spectral discretization along the z direction.

We take the domain along the z direction as $z \in [0, L_z]$, and assume that the domain and all the dynamic variables are periodic at z=0 and $z=L_z$, where L_z is the dimension of the computational domain in z. Then the following relations hold,

$$\begin{cases}
\Omega = \Omega_{2D} \otimes [0, L_z], & \partial\Omega = \partial\Omega_{2D} \otimes [0, L_z], & \partial\Omega_s = \partial\Omega_s^{2D} \otimes [0, L_z], & \partial\Omega_o = \partial\Omega_o^{2D} \otimes [0, L_z], \\
\partial\Omega_{se} = \partial\Omega_{se}^{2D} \otimes [0, L_z], & \partial\Omega_{sg} = \partial\Omega_{sg}^{2D} \otimes [0, L_z].
\end{cases}$$
(59)

In the above relations Ω is the 3D domain, and Ω_{2D} is the computational domain in the xy plane (i.e. projection of Ω onto the xy plane). Similarly, $\partial\Omega_{2D}$, $\partial\Omega_s^{2D}$, $\partial\Omega_o^{2D}$, $\partial\Omega_{se}^{2D}$ and $\partial\Omega_{sg}^{2D}$ are projections onto the xy plane of the 3D boundaries $\partial\Omega$, $\partial\Omega_s$, $\partial\Omega_o$, $\partial\Omega_{se}$ and $\partial\Omega_{sg}$, respectively. In addition, we have the following

$$\mathbf{n} = (\mathbf{n}_{2D}, 0), \quad \mathbf{n}_o = (\mathbf{n}_o^{2D}, 0), \quad \mathbf{n}_s = (\mathbf{n}_s^{2D}, 0).$$
 (60)

Here \mathbf{n} , \mathbf{n}_o and \mathbf{n}_s denote the outward-pointing unit vectors normal to $\partial\Omega$, $\partial\Omega_o$ and $\partial\Omega_s$, respectively. \mathbf{n}_{2D} , \mathbf{n}_o^{2D} and \mathbf{n}_s^{2D} are the outward-pointing unit vectors normal to $\partial\Omega_{2D}$, $\partial\Omega_o^{2D}$ and $\partial\Omega_s^{2D}$, respectively. Let N_z denote the number of Fourier grid points in z. We introduce the Fourier basis functions,

$$\Phi_k(z) = e^{i\beta_k z}, \quad \beta_k = \frac{2\pi k}{L_z}, \quad -\frac{N_z}{2} \le k \le \frac{N_z}{2} - 1.$$
(61)

Then, for a generic function f(x, y, z) we have the Fourier expansion relation,

$$f(x,y,z) = \sum_{k=-N_z/2}^{N_z/2-1} \hat{f}_k(x,y)\Phi_k(z), \quad \int_0^{L_z} f(x,y,z)\bar{\Phi}_k(z)dz = L_z\hat{f}_k(x,y), \tag{62}$$

where $\bar{\Phi}_k$ is the complex conjugate of Φ_k , and $\hat{f}_k(x,y)$ denotes the k-th Fourier mode of f(x,y,z). We define the basis and test functions in 3D by, for $-\frac{N_z}{2} \le k \le \frac{N_z}{2} - 1$,

$$\begin{cases}
Q_k(x, y, z) = l(x, y)\Phi_k(z), & \text{(basis function)}, \\
\bar{Q}_k(x, y, z) = l(x, y)\bar{\Phi}_k(z), & \text{(test function)},
\end{cases}$$
(63)

where l(x,y) denotes an arbitrary function in the xy plane. Define $\nabla = \left(\nabla_{2D}, \frac{\partial}{\partial z}\right) = \left(\frac{\partial}{\partial x}, \frac{\partial}{\partial y}, \frac{\partial}{\partial z}\right)$. Let f(x,y,z) denote a generic scalar field and $\mathbf{u}(x,y,z) = (\mathbf{u}_{2D}(x,y,z), u_z(x,y,z)) = (u_x(x,y,z), u_y(x,y,z), u_z(x,y,z))$ denote the velocity (or a generic vector) field. Then the following relations hold,

$$\begin{cases}
\int_{\Omega} f(x,y,z) \bar{Q}_{k}(x,y,z) d\Omega = L_{z} \int_{\Omega_{2D}} \hat{f}_{k}(x,y) l(x,y) d\Omega_{2D} \\
\int_{\Omega} \nabla f(x,y,z) \cdot \nabla \bar{Q}_{k}(x,y,z) d\Omega = L_{z} \int_{\Omega_{2D}} \left[\nabla_{2D} \hat{f}_{k}(x,y) \cdot \nabla_{2D} l(x,y) + \beta_{k}^{2} \hat{f}_{k}(x,y) l(x,y) \right] d\Omega_{2D} \\
\int_{\Omega} \mathbf{u} \cdot \nabla \bar{Q}_{k} d\Omega = L_{z} \int_{\Omega_{2D}} \left[\nabla_{2D} l(x,y) \cdot \hat{\mathbf{u}}_{2D,k} - i\beta_{k} l(x,y) \hat{u}_{z,k} \right] d\Omega_{2D}
\end{cases} (64)$$

where $\hat{\mathbf{u}}_{2D,k}$ and $\hat{u}_{z,k}$ are the Fourier modes of \mathbf{u}_{2D} and u_z , respectively, and $d\Omega = d\Omega_{2D}dz$.

By using the above integral relations, we can reduce the 3D weak forms in (42)–(50) into 2D weak forms about the Fourier modes. Let us assume in the following that $\omega(x,y)$ denote an arbitrary 2D test function for the electric potential, the electric field and the phase field functions, and v(x,y) denote an arbitrary 2D test function about the pressure and velocity fields. For simplicity, we will assume that $\omega(x,y)$ and v(x,y)vanish on the corresponding Dirichlet type boundaries. We use the 2D function $(\hat{\cdot})_k$ or $(\hat{\cdot})_k$ of (x,y) to denote the k-th Fourier mode of the 3D function (\cdot) of (x, y, z).

Let $\mathbf{R} = (\epsilon(\phi^{*,n+1}) - \varepsilon_0)\nabla V^{*,n+1} = (\mathbf{R}_{2D}, R_z)$. The weak form (42) is reduced to,

$$\int_{\Omega_{2D}} \varepsilon_0 \nabla_{2D} \hat{V}_k^{n+1} \cdot \nabla_{2D} \omega + \beta_k^2 \int_{\Omega_{2D}} \varepsilon_0 \hat{V}_k^{n+1} \omega = -\int_{\Omega_{2D}} \hat{\mathbf{R}}_k \cdot \nabla \omega - \int_{\Omega_{2D}} \hat{f}_{V,k}^{n+1} \omega, \quad \forall \omega(x,y),$$
 (65)

where $\nabla \omega(x,y) = (\nabla_{2D}\omega, -i\beta_k\omega)$, and we have used the following equation,

$$\int_{\Omega} \mathbf{R} \cdot \nabla \bar{Q}_{k} = \sum_{m=-N_{z}/2}^{N_{z}/2-1} \left(\int_{\Omega_{2D}} \hat{\mathbf{R}}_{m} \cdot \nabla \omega \right) \left(\int_{0}^{L_{z}} \Phi_{m}(z) \bar{\Phi}_{k}(z) \right)
= L_{z} \int_{\Omega_{2D}} \hat{\mathbf{R}}_{k} \cdot \nabla \omega = L_{z} \int_{\Omega_{2D}} \left(\hat{\mathbf{R}}_{2D,k} \cdot \nabla_{2D} \omega - i \beta_{k} \hat{R}_{z,k} \omega \right).$$
(66)

The 3D weak form (43) now becomes

$$\int_{\Omega_{2D}} (\hat{E}_{x,k}^{n+1}, \hat{E}_{y,k}^{n+1}, \hat{E}_{z,k}^{n+1}) \omega = \int_{\Omega_{2D}} (\partial_x \hat{V}_k^{n+1}, \partial_y \hat{V}_k^{n+1}, -i\beta_k \hat{V}_k^{n+1}) \omega, \quad \forall \omega(x,y),$$
 (67)

where $\hat{\mathbf{E}}_{k}^{n+1} = (\hat{E}_{x,k}^{n+1}, \hat{E}_{y,k}^{n+1}, \hat{E}_{z,k}^{n+1})$. The weak forms (46)–(47) are reduced to,

$$\int_{\Omega_{2D}} \nabla_{2D} \hat{\psi}_k^{n+1} \cdot \nabla_{2D} \omega + \left(\alpha + \frac{S}{\eta^2} + \beta_k^2\right) \int_{\Omega_{2D}} \hat{\psi}_k^{n+1} \omega = \int_{\Omega_{2D}} (\beta_k^2 \hat{Q}_{2,k} - \hat{Q}_{1,k}) \omega + \int_{\Omega_{2D}} \nabla_{2D} \hat{Q}_{2,k} \cdot \nabla \omega + \int_{\partial\Omega_{aD}^{2D}} \left[\hat{g}_{1,k}^{n+1} + \left(\alpha + \frac{S}{\eta^2}\right) \hat{g}_{2,k}^{n+1}\right] \omega + \int_{\partial\Omega_{sD}^{2D}} \left[\hat{g}_{1,k}^{n+1} + \left(\alpha + \frac{S}{\eta^2}\right) \hat{U}_k\right] \omega, \quad \forall \omega(x,y); \tag{68}$$

$$\int_{\Omega_{2D}} \nabla_{2D} \hat{\phi}_k^{n+1} \cdot \nabla_{2D} \omega + (-\alpha + \beta_k^2) \int_{\Omega_{2D}} \hat{\phi}_k^{n+1} \omega = \int_{\Omega_{2D}} \hat{\psi}_k^{n+1} \omega + \int_{\partial \Omega_{o}^{2D}} \hat{g}_{2,k}^{n+1} \omega + \int_{\partial \Omega_{s}^{2D}} \hat{U}_k \omega,
\forall \omega(x,y),$$
(69)

where $U = -g_3^{n+1} - \frac{\Theta'(\phi^{*,n+1})}{\lambda}$, and \hat{U}_k denotes the Fourier modes of U.

$$\begin{cases}
\mathbf{G} = (\mathbf{G}_{2D}, G_z) = \mathbf{T} + \nabla \left(\frac{\mu^{n+1}}{\rho^{n+1}}\right) \times \boldsymbol{\omega}^{*,n+1}, & \mathbf{Y} = \mathbf{G} - \frac{1}{\rho_0} \nabla P^{n+1}, \\
\mathbf{J} = (\mathbf{J}_{2D}, J_z) = \frac{\mu^{n+1}}{\rho^{n+1}} \mathbf{n} \times \boldsymbol{\omega}^{*,n+1}, & \mathbf{K} = \left(\frac{\mu^{n+1}}{\rho^{n+1}} - \nu_m\right) \boldsymbol{\omega}^{*,n+1}, & \mathbf{L} = \left(\frac{\mu^{n+1}}{\rho^{n+1}} - \nu_m\right) \mathbf{n} \times \boldsymbol{\omega}^{*,n+1}.
\end{cases} (70)$$

The weak form (48) for the pressure is reduced to

$$\int_{\Omega_{2D}} \nabla_{2D} \hat{P}_{k}^{n+1} \cdot \nabla_{2D} v + \beta_{k}^{2} \int_{\Omega_{2D}} \hat{P}_{k}^{n+1} v = \rho_{0} \int_{\Omega_{2D}} \hat{\mathbf{G}}_{2D,k} \cdot \nabla_{2D} v - i\beta_{k} \rho_{0} \int_{\Omega_{2D}} \hat{\mathbf{G}}_{z,k} v \\
- \rho_{0} \int_{\partial \Omega_{0}^{2D}} \hat{\mathbf{J}}_{2D,k} \cdot \nabla_{2D} v + i\beta_{k} \rho_{0} \int_{\partial \Omega_{0}^{2D}} \hat{J}_{z,k} v - \frac{\rho_{0} \gamma_{0}}{\Delta t} \int_{\partial \Omega_{s}^{2D}} \mathbf{n}_{2D} \cdot \hat{\mathbf{w}}_{2D,k}^{n+1} v, \quad \forall v(x,y). \tag{71}$$

The weak form (50) for the velocity is reduced to,

$$\int_{\Omega_{2D}} \nabla_{2D} v \cdot \nabla_{2D} \hat{\mathbf{u}}_{k}^{n+1} + \left(\beta_{k}^{2} + \frac{\gamma_{0}}{\nu_{m} \Delta t}\right) \int_{\Omega_{2D}} \hat{\mathbf{u}}_{k}^{n+1} v = \frac{1}{\nu_{m}} \int_{\Omega_{2D}} \hat{\mathbf{Y}}_{k} v - \frac{1}{\nu_{m}} \int_{\Omega_{2D}} \hat{\mathbf{K}}_{k} \times \nabla v + \int_{\partial\Omega^{2D}} \hat{\mathbf{f}}_{1,k}^{n+1} v - \frac{1}{\nu_{m}} \int_{\partial\Omega^{2D}} \hat{\mathbf{L}}_{k} v, \quad \forall v(x,y). \tag{72}$$

Note that the terms $i\beta_k\rho_0 \int_{\Omega_{2D}} \hat{G}_{z,k}v$ and $i\beta_k\rho_0 \int_{\partial\Omega_o^{2D}} \hat{J}_{z,k}^{n+1}v$ in equation (71) and the term $\frac{1}{\nu_m} \int_{\Omega_{2D}} \hat{\mathbf{K}}_k \times \nabla v$ in equation (72) mixes up the imaginary and real parts, which calls for special attention in the implementation.

To formulate the fully discretized equations in 3D, we partition the domain Ω_{2D} in the xy plane by a mesh of C^0 spectral elements. Let Ω_{2Dh} denote the discretized Ω_{2D} , $\Omega_{2Dh} = \bigcup_{e=1}^{N_e} \Omega_{2Dh}^e$, where Ω_{2Dh}^e denotes the element e in the xy plane. Let $\partial \Omega_{2Dh}$, $\partial \Omega_{oh}^{2D}$, and $\partial \Omega_{sh}^{2D}$ denote the discretized versions of $\partial \Omega_{2D}$, $\partial \Omega_{oh}^{2D}$, and $\partial \Omega_{sh}^{2D}$, respectively. Let $\partial \Omega_{seh}^{2D}$ and $\partial \Omega_{sgh}^{2D}$ denote the discretized solid-electrode and solid-gap boundaries in Ω_{2D} , $\partial \Omega_{sh}^{2D} = \partial \Omega_{seh}^{2D} \cup \partial \Omega_{sgh}^{2D}$. Let $\Pi_K(\Omega_{2Dh}^e)$ denote the polynomial space defined on Ω_{2Dh}^e with their degrees characterized by K. We define

$$\begin{cases}
\mathbb{Y}_{h} = \{ v \in H^{1}(\Omega_{2Dh}) : v |_{\Omega_{2Dh}^{e}} \in \Pi_{K}(\Omega_{2Dh}^{e}), 1 \leq e \leq N_{e} \}, \\
\mathbb{Y}_{h0}^{E} = \{ v \in \mathbb{Y}_{h} : v |_{\partial\Omega_{seh}^{2D}} = 0 \}, \\
\mathbb{Y}_{h0}^{P} = \{ v \in \mathbb{Y}_{h} : v |_{\partial\Omega_{oh}^{2D}} = 0 \}, \\
\mathbb{Y}_{h0}^{u} = \{ v \in \mathbb{Y}_{h} : v |_{\partial\Omega_{sh}^{2D}} = 0 \}.
\end{cases}$$
(73)

In the following the subscript h denotes the discretized version of a variable.

Then the fully discretized system in 3D consists of the following equations:

For V_h^{n+1} : find $\hat{V}_{kh}^{n+1} \in \mathbb{Y}_h$ such that (for $-N_z/2 \leqslant k \leqslant N_z/2 - 1$)

$$\int_{\Omega_{2Dh}} \varepsilon_0 \nabla_{2D} \hat{V}_{kh}^{n+1} \cdot \nabla_{2D} \omega_h + \beta_k^2 \int_{\Omega_{2Dh}} \varepsilon_0 \hat{V}_{kh}^{n+1} \omega_h = -\int_{\Omega_{2Dh}} \hat{\mathbf{R}}_{kh} \cdot \nabla \omega_h - \int_{\Omega_{2Dh}} \hat{f}_{V,kh}^{n+1} \omega_h,
\forall \omega_h \in \mathbb{Y}_{h0}^E;$$
(74a)

$$\hat{V}_{kh}^{n+1} = \begin{cases} \mathcal{V}_e, & k = 0, \\ 0, & k \neq 0. \end{cases} \quad \text{on } \partial\Omega_{seh}^{2D}.$$
 (74b)

For \mathbf{E}_h^{n+1} : find $\hat{\mathbf{E}}_{kh}^{n+1} = (\hat{E}_{x,kh}^{n+1}, \hat{E}_{y,kh}^{n+1}, \hat{E}_{z,kh}^{n+1}) \in [\mathbb{Y}_h]^3$, such that (for $-N_z/2 \leqslant k \leqslant N_z/2 - 1$)

$$\int_{\Omega_{2Dh}} (\hat{E}_{x,kh}^{n+1}, \hat{E}_{y,kh}^{n+1}, \hat{E}_{z,kh}^{n+1}) \omega_h = \int_{\Omega_{2Dh}} (\partial_x \hat{V}_{kh}^{n+1}, \partial_y \hat{V}_{kh}^{n+1}, -i\beta_k \hat{V}_{kh}^{n+1}) \omega_h, \quad \forall \omega_h \in \mathbb{Y}_h.$$
 (75)

For ψ_h^{n+1} : find $\hat{\psi}_{kh}^{n+1} \in \mathbb{Y}_h$ such that (for $-N_z/2 \leqslant k \leqslant N_z/2 - 1$)

$$\int_{\Omega_{2Dh}} \nabla_{2D} \hat{\psi}_{kh}^{n+1} \cdot \nabla_{2D} \omega_h + \left(\alpha + \frac{S}{\eta^2} + \beta_k^2\right) \int_{\Omega_{2Dh}} \hat{\psi}_{kh}^{n+1} \omega_h$$

$$= \int_{\Omega_{2Dh}} (\beta_k^2 \hat{Q}_{2,kh} - \hat{Q}_{1,kh}) \omega_h + \int_{\Omega_{2Dh}} \nabla_{2D} \hat{Q}_{2,kh} \cdot \nabla \omega_h$$

$$+ \int_{\partial \Omega_{ah}^{2D}} \left[\hat{g}_{1,kh}^{n+1} + \left(\alpha + \frac{S}{\eta^2}\right) \hat{g}_{2,kh}^{n+1} \right] \omega_h + \int_{\partial \Omega_{sh}^{2D}} \left[\hat{g}_{1,kh}^{n+1} + \left(\alpha + \frac{S}{\eta^2}\right) \hat{U}_{kh} \right] \omega_h, \quad \forall \omega_h \in \mathbb{Y}_h. \tag{76}$$

For ϕ_h^{n+1} : find $\hat{\phi}_{kh}^{n+1} \in \mathbb{Y}_h$ such that (for $-N_z/2 \leqslant k \leqslant N_z/2 - 1$)

$$\int_{\Omega_{2Dh}} \nabla_{2D} \hat{\phi}_{kh}^{n+1} \cdot \nabla_{2D} \omega_h + (-\alpha + \beta_k^2) \int_{\Omega_{2Dh}} \hat{\phi}_{kh}^{n+1} \omega_h$$

$$= \int_{\Omega_{2Dh}} \hat{\psi}_{kh}^{n+1} \omega_h + \int_{\partial\Omega_{2h}^{2D}} \hat{g}_{2,kh}^{n+1} \omega_h + \int_{\partial\Omega_{sh}^{2D}} \hat{U}_{kh} \omega_h, \quad \forall \omega_h \in \mathbb{Y}_h. \tag{77}$$

For P_h^{n+1} : find $\hat{P}_{kh}^{n+1} \in \mathbb{Y}_h$ such that (for $-N_z/2 \leqslant k \leqslant N_z/2 - 1$)

$$\int_{\Omega_{2Dh}} \nabla_{2D} \hat{P}_{kh}^{n+1} \cdot \nabla_{2D} v_h + \beta_k^2 \int_{\Omega_{2Dh}} \hat{P}_{kh}^{n+1} v_h = \rho_0 \int_{\Omega_{2Dh}} \hat{\mathbf{G}}_{2D,kh} \cdot \nabla_{2D} v_h - i\beta_k \rho_0 \int_{\Omega_{2Dh}} \hat{G}_{z,kh} v_h \\
- \rho_0 \int_{\partial\Omega_{oh}^{2D}} \hat{\mathbf{J}}_{2D,kh} \cdot \nabla_{2D} v_h + i\beta_k \rho_0 \int_{\partial\Omega_{oh}^{2D}} \hat{J}_{z,kh} v_h - \frac{\rho_0 \gamma_0}{\Delta t} \int_{\partial\Omega_{sh}^{2D}} \mathbf{n}_{2Dh} \cdot \hat{\mathbf{w}}_{2D,kh}^{n+1} v_h, \quad \forall v_h \in \mathbb{Y}_{h0}^P; \quad (78a)$$

$$\hat{P}_{kh}^{n+1} = \hat{f}_{2kh}^{n+1}, \quad \text{on } \partial\Omega_{oh}^{2D}. \quad (78b)$$

Algorithm 2: Solution Procedure within a Time Step for 3D Dielectric Flows

```
input: V^n, \phi^n, P^n, \mathbf{u}^n.
output: V^{n+1}, \mathbf{E}^{n+1}, \psi^{n+1}, \phi^{n+1}, P^{n+1}, \mathbf{u}^{n+1}.

1 solve equations (74a)–(74b) for \hat{V}_k^{n+1} (-N_z/2 \le k \le N_z/2), with Fourier transform to attain V^{n+1}
2 solve equation (75) for \hat{\mathbf{E}}_k^{n+1} (-N_z/2 \le k \le N_z/2), with Fourier transform to attain \mathbf{E}^{n+1}
3 solve equation (76) for \hat{\psi}_k^{n+1} (-N_z/2 \le k \le N_z/2), with Fourier transform to attain \psi^{n+1}
4 solve equation (77) for \hat{\phi}_k^{n+1} (-N_z/2 \le k \le N_z/2), with Fourier transform to attain \phi^{n+1}
5 solve equations (78a)–(78b) for \hat{P}_k^{n+1} (-N_z/2 \le k \le N_z/2), with Fourier transform to attain P^{n+1}
6 solve equations (79a)–(79b) for \hat{\mathbf{u}}_k^{n+1} (-N_z/2 \le k \le N_z/2), with Fourier transform to attain \mathbf{u}^{n+1}
```

For \mathbf{u}_h^{n+1} : find $\hat{\mathbf{u}}_{kh}^{n+1} \in [\mathbb{Y}_h]^3$ such that (for $-N_z/2 \leqslant k \leqslant N_z/2 - 1$)

$$\int_{\Omega_{2Dh}} \nabla_{2D} v_h \cdot \nabla_{2D} \hat{\mathbf{u}}_{kh}^{n+1} + \left(\beta_k^2 + \frac{\gamma_0}{\nu_m \Delta t}\right) \int_{\Omega_{2Dh}} \hat{\mathbf{u}}_{kh}^{n+1} v_h = \frac{1}{\nu_m} \int_{\Omega_{2Dh}} \hat{\mathbf{Y}}_{kh} v_h \\
- \frac{1}{\nu_m} \int_{\Omega_{2Dh}} \hat{\mathbf{K}}_{kh} \times \nabla v_h + \int_{\partial \Omega_{oh}^{2D}} \hat{\mathbf{f}}_{1,kh}^{n+1} v_h - \frac{1}{\nu_m} \int_{\partial \Omega_{oh}^{2D}} \hat{\mathbf{L}}_{kh} v_h, \quad \forall v_h \in \mathbb{Y}_{h0}^u. \tag{79a}$$

$$\hat{\mathbf{u}}_{hh}^{n+1} = \hat{\mathbf{w}}_{hh}^{n+1}, \quad \text{on } \partial \Omega_{oh}^{2D}. \tag{79b}$$

Given $(V^n, \phi^n, P^n, \mathbf{u}^n)$ in 3D, the field variables V^{n+1} , \mathbf{E}^{n+1} , ψ^{n+1} , ϕ^{n+1} , P^{n+1} and \mathbf{u}^{n+1} are computed by solving the equations (74)–(79) individually and successively in an un-coupled fashion. Algorithm 2 summarizes the solution procedure for 3D problems.

Remark 3.3 The Algorithms 1 and 2, respectively for 2D and 3D two-phase dielectric flows, share a common characteristic. The resultant linear algebraic systems for the dynamic variables (V^{n+1} , \mathbf{E}^{n+1} , ψ^{n+1} , ϕ^{n+1} , P^{n+1} , \mathbf{u}^{n+1}) all involve a constant and time-independent coefficient matrix upon discretization, which only needs to be computed once and thus can be pre-computed and saved for later use, despite the variable permittivity/density/viscosity field involved in the system on the continuum level. Because of this property, the current method is computationally very efficient for simulating two-phase dielectric flow problems.

4 Representative Numerical Simulations

4.1 Convergence Test

We next employ a manufactured analytic solution to the governing equations to demonstrate the spatial and temporal convergence rates of the numerical method presented in Section 3.

We first look into the convergence for 2D problems. Consider a domain $\Omega = \{(x,y) : 0 \le x \le 2, 0 \le y \le 1\}$ (see Figure 2(a)), and the two-phase dielectric governing equations and boundary/initial conditions on Ω as given by equations (27)–(29), (5), (7), (31)–(34), (20), (23). We employ the following manufactured solution to this problem:

$$\begin{cases} u = \cos(\pi y)\sin(\pi x)\sin(t), & v = -\sin(\pi y)\cos(\pi x)\sin(t), & P = \sin(\pi y)\cos(\pi x)\cos(t), \\ \phi = \cos(\pi x)\cos(\pi y)\sin(t), & V = \sin(\pi x)\cos(\pi y), \end{cases}$$
(80)

where $\mathbf{u} = (u, v)$. All the source terms involved in the governing equations and boundary/initial conditions are chosen such that the field distributions given in (80) satisfy the governing equations and boundary/initial conditions.

To simulate this problem, we discretize the domain using two spectral elements of the same size, as shown in Figure 2(a). On the left/right boundaries (x = 0, 2) we impose the periodic condition for all the dynamic variables. The bottom boundary (y = 0) is assumed to be a wall, and we impose the Dirichlet condition for the velocity and the electric potential (see equations (34) and (23)), and the boundary condition (33) for the phase field function. The top boundary (y = 1) is assumed to be open, and we impose the boundary

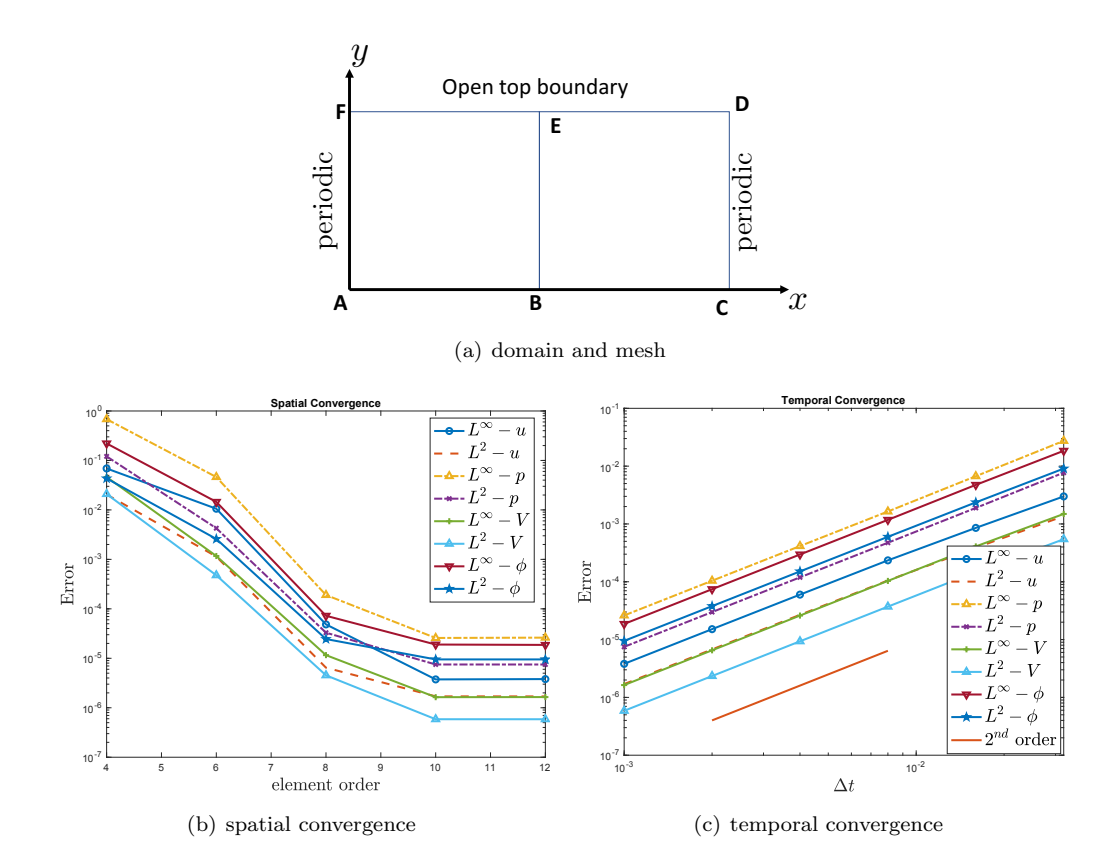


Figure 2: 2D convergence test: (a) Sketch of the computational domain and configuration. (b) L^{∞} and L^2 errors of the dynamic variables versus the element order (fixed $\Delta t = 0.001$), showing spatial exponential convergence. (c) L^{∞} and L^2 errors versus Δt (fixed element order = 14), showing temporal second-order convergence rate.

conditions (20), (31) and (32) for the electric potential, the phase field function and the velocity/pressure, respectively.

Figure 2(b) shows the L^{∞} and L^2 errors of the velocity, pressure, phase field function, and the electric potential versus the element order. Here the time step size is fixed at $\Delta t = 0.001$, and the governing equations are integrated from t=0 to $t=t_f=0.2$. Shown in this figure are the errors of dynamic variables at $t=t_f$. The errors decrease exponentially with increasing element order (when below 10), and they stagnate when the element order increases beyond 10 due to the dominance of the temporal truncation error.

Figure 2(c) illustrates the temporal convergence of the method. The L^{∞} and L^2 errors of the dynamic variables at $t = t_f = 0.4$ as a function of Δt are shown. In this group of tests the element order is fixed at 14. We observe a second-order convergence rate for these field variables.

To test the spatial/temporal convergence of the 3D algorithm, we consider the domain $\Omega = \{(x,y,z) : 0 \le x \le 2, -1 \le y \le 1, 0 \le z \le 2\}$, as sketched in Figure 3(a). The plane \overline{HBEK} (x=1) partitions the domain into two equal sub-domains. The domain Ω and all the flow variables are assumed to be homogeneous along z. The top boundary (y=1) is open. The boundaries along the x direction (x=0 and 2) are periodic. On the bottom face \overline{ACIG} , we impose the Dirichlet boundary condition for the velocity \mathbf{u} , and the wall boundary conditions (33) for the phase field function ϕ . For the electric potential V, we impose the Dirichlet condition (second equation in (23)) on the region \overline{ABHG} and the Neumann condition (first equation in (23)) on the region \overline{BCIH} .

We employ the following manufactured analytic solution on Ω for the 3D convergence tests,

$$\begin{cases} u = \cos(\pi x)\cos(\pi y)\cos(\pi z)\sin(t), & v = 0, \quad w = \sin(\pi x)\cos(\pi y)\sin(\pi z)\sin(t), \\ P = \sin(\pi x)\sin(\pi y)\sin(\pi z)\cos(t), & \phi = \cos(\pi x)\cos(\pi y)\cos(\pi z)\sin(t), & V = \sin(\pi x)\cos(\pi y)\cos(\pi z), \end{cases}$$
(81)

where $\mathbf{u} = (u, v, w)$. The source terms in the governing equations and the non-homogeneous boundary

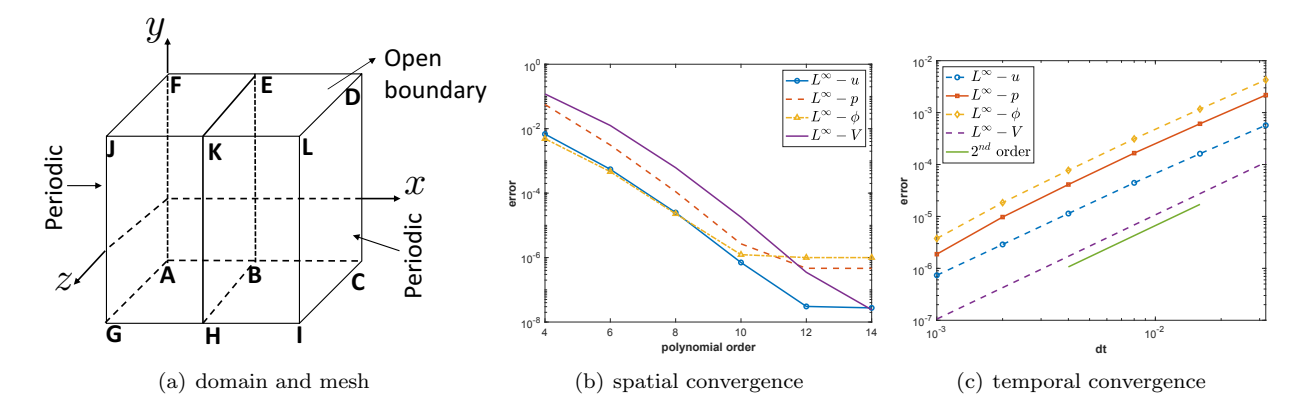


Figure 3: 3D convergence test: (a) Domain and configuration. (b) L^{∞} errors of the dynamic variables versus the element order (fixed $\Delta t = 0.001$ and $N_z = 8$), showing spatial exponential convergence. (b) L^{∞} errors versus Δt (fixed element order 14 and $N_z = 8$), showing temporal second-order convergence rate.

variable	normalization constant	variable	normalization constant
x, y, z, d, η	L_0	t	1
V, V_0	V_d	\mathbf{E}	V_d/L_0
$\epsilon,\epsilon_1,\epsilon_2$	$L_0\gamma/V_d^2$	γ_1	L_0^3/γ
λ	$L_0\gamma$	ϕ, ψ	1

Table 2: Normalization constants for variables and parameters with the simpler system from Section 2.4 for computing the equilibrium solution. Choose L_0 , V_d , and γ (surface tension).

conditions are set according to these analytic expressions. We employ $N_z = 8$ Fourier grid points along the z direction, and two spectral elements in the xy planes, as shown in Figure 3(a).

The spatial convergence of the 3D algorithm is illustrated by Figure 3(b), in which the L^{∞} errors of the dynamic variables are shown as a function of the element order. Here the problem is simulated from t=0 to $t=t_f=0.1$, and the time step size is fixed at $\Delta t=0.001$. The exponential convergence in space is evident from the results.

The temporal convergence of the 3D algorithm is illustrated by Figure 3(c). Here the L^{∞} errors of the dynamic variables are shown as a function of Δt . The element order has been fixed at 14, and the final integration time is $t = t_f = 0.1$. One can observe the second-order convergence rate with respect to Δt .

4.2 Equilibrium Dielectric Drop on a Wall

We study the 3D equilibrium shape of a dielectric liquid drop on a horizontal wall under an imposed electric field in this test. The problem setting is in accordance with the experiment from [54]; see Figure 4(a). When the electrodes on the wall are turned on, the dielectric drop (an initial hemisphere) deforms due to the imposed electric field, and eventually reaches an equilibrium state, as sketched in Figure 4(b). We are interested in simulating the equilibrium shape of the dielectric drop.

As discussed in Section 2.4, the current phase field model allows us to compute the equilibrium state of the system by solving an alternative simpler system consisting of equations (17), (16c) and (16d), with the corresponding boundary and initial conditions. After that, if needed, the pressure field can be computed by solving (16b), and the velocity is given by $\mathbf{u} = 0$. We will simulate the equilibrium shape of the dielectric liquid drop by this method.

We consider a computational domain $(x, y, z) \in \Omega = [0, \frac{5}{3}L_0] \times [0, \frac{7}{2}L_0] \times [0, \frac{7}{2}L_0]$, where $L_0 = 1.2mm$, as shown in Figure 4(a). The electrodes embedded on the bottom wall each has a width d = 0.1mm. Adjacent electrodes are 0.1mm apart on the wall, and the constant voltage imposed on adjacent electrodes have the same magnitude but with opposite signs $(V_0 \text{ and } -V_0)$, as sketched in Figure 4(b). The dielectric liquid drop (in ambient air) is initially shaped like a hemisphere, with a radius $R_0 = \frac{1}{2}L_0$ and its center located at $(X_0, Y_0, Z_0) = (\frac{5}{6}L_0, 0, \frac{7}{4}L_0)$.

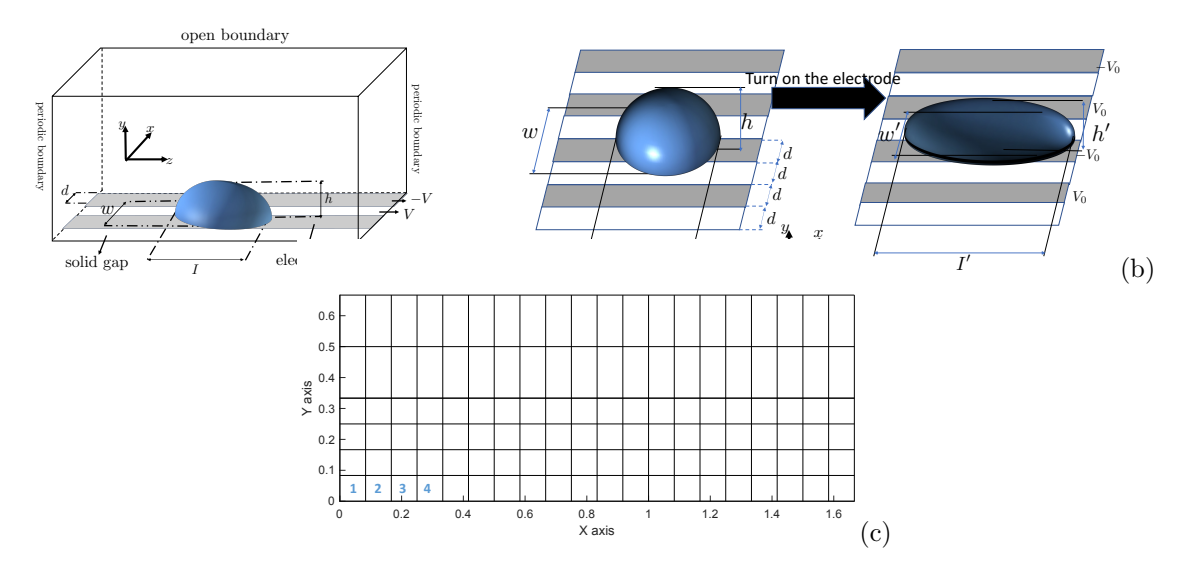


Figure 4: Dielectric liquid drop on a wall: (a) Sketch of domain and flow configuration. (b) Cartoon of the drop deformation when the electrodes are switched on. (c) The spectral element mesh in the xy plane used in the simulations. On bottom wall, the shaded regions are the electrodes and the white regions denote the gaps between the electrodes. In (c), at the bottom wall, the voltage is V_0 in element 1, element 2 is a gap, the voltage is $-V_0$ in element 3, element 4 is a gap, etc.

We employ the following physical parameter values:

$$\begin{cases} \text{surface tension: } \gamma = 3.857 \times 10^{-2} kg/s^2; \\ \text{permittivity: (air) } \epsilon_1 = \epsilon_0, \quad \text{(dielectric liquid) } \epsilon_2 = 32\epsilon_0; \end{cases}$$
(82)

where $\epsilon_0 = 8.854 \times 10^{-12} F/m$ is the vacuum permittivity. Note that the fluid density and viscosity play no role when we simulate the equilibrium state using the system consisting of (17), (16c) and (16d).

All the dynamic variables and simulation parameters are normalized consistently. The normalization constants used for non-dimensionalizing the alternative system of equations from Section 2.4 for the equilibrium solution are provided in Table 2. Note that they are a little different from those shown in Table 1 for normalizing the full system of governing equations. In particular, all the length variables are normalized by L_0 . For brevity and convenience of presentation, in what follows we employ the same symbols to denote the dimensional and the normalized variables or parameters. We employ a Cahn number $\eta = 0.02$, and the mobility is set by $\lambda \gamma_1 = 0.1$, where $\lambda = \frac{3}{2\sqrt{2}}\eta$. The pseudo-time-step size is $\Delta t = 2 \times 10^{-6}$ in the simulations.

We solve the system consisting of equations (17), (16c) and (16d) by the hybrid spectral element/Fourier spectral method in 3D. We employ $N_z=120$ Fourier grid points along the z direction and a mesh of 120 quadrilateral spectral elements (with element order 12) in the xy plane, with 20 uniform elements along x and 6 non-uniform elements along y (see Figure 4(c)). We impose the periodic boundary condition in x (at x=0 and $x=\frac{5}{3}L_0$), and the boundary conditions (18) and (20) at the top boundary $y=\frac{2}{3}L_0$. On the bottom wall (y=0) we impose the boundary conditions (21) and (23), where the imposed voltage on adjacent electrodes alternates between V_0 and $-V_0$ (see Figure 4(c)). All the dynamic variables are homogeneous along the z direction. The initial distribution of the phase field function is given by $\phi(x,y,z)=\tanh\left(\frac{\sqrt{(x-X_0)^2+(y-Y_0)^2+(z-Z_0)^2}-R_0}{\sqrt{2}\eta}\right)$.

Figure 5 shows the deformed shape of the dielectric drop under three imposed electrode voltages ($V_0 = 100$ volt, 150volt, and 200volt) obtained from the 3D simulations. The plots in the three rows show the plan view, the side view, and the perspective view of the drop, respectively. The drop deformation becomes increasingly pronounced with increasing electrode voltage. At $V_0 = 200$ volt, the dielectric drop becomes highly elongated along the z direction (see Figures 5(c,f,i)).

Figure 5 illustrates the asymmetric deformation of dielectric drops, an important feature observed in experiments (see [26]). The dielectric droplet tends to stretch along the direction parallel to the electrodes,

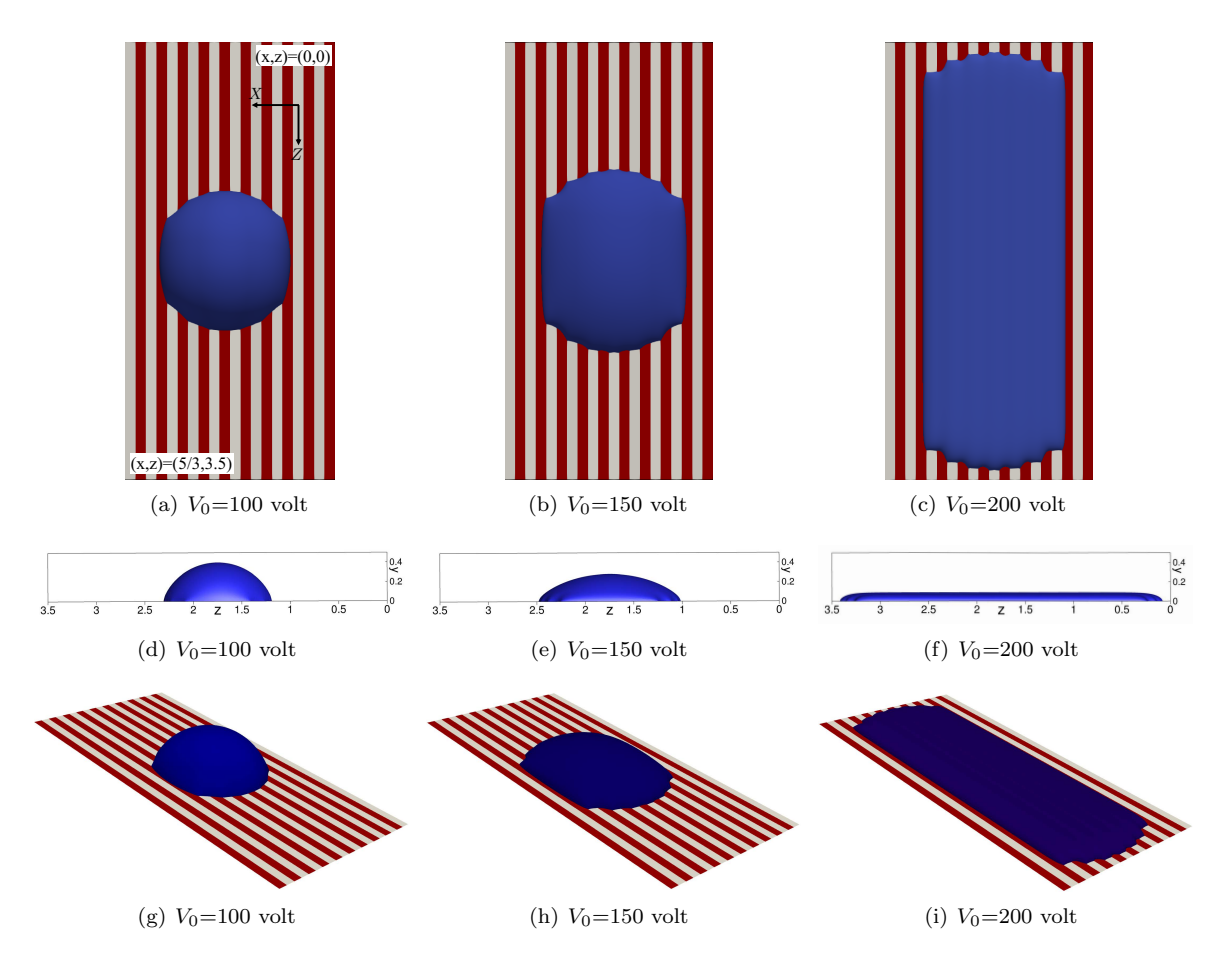


Figure 5: Dielectric drop on the wall: equilibrium drop shapes under imposed electrode voltage $V_0 = 100$ volt (left column), $V_0 = 150$ volt (middle column), and $V_0 = 200$ volt (right column). Top row: plan view (toward -y direction); Middle row: side view (toward -x direction); Bottom tow: perspective view.

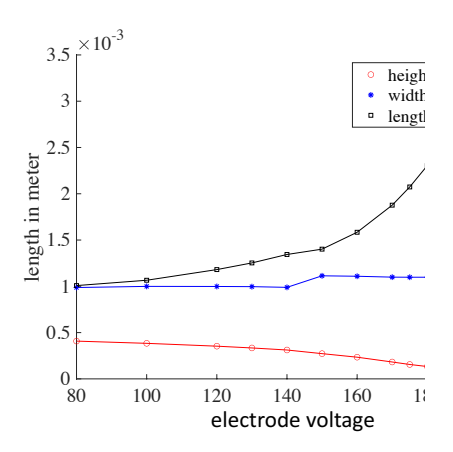
while in the direction perpendicular to the electrodes the droplet remains approximately the same in dimension. In other words, the width of the drop (w in Figure 4(a)) remains approximately unchanged, while the length and height of the drop (l and h in Figure 4(a)) can vary significantly with the electrode voltage.

The asymmetric deformation is further demonstrated by Figure 6(a), in which we plot the length, width, and height of the deformed dielectric drop as a function of the electrode voltage from our simulations. It is evident that, while the length and height exhibit a significant change, the width of the deformed drop remains nearly constant as the electrode voltage increases. This is because the electrodes serve as some potential walls, and so crossing those walls will increase the energy of the system. We refer to [26] for more details on the experimental observation and the explanation of the asymmetric deformation.

In [8] a theoretical model was proposed on the dielectric drop deformation, and it leads to the following formula relating the drop height to the electrode voltage,

$$h^2 = h_0^2 - \frac{\epsilon_0 \Delta \epsilon V_0^2}{4\delta \gamma} \Omega. \tag{83}$$

In this equation, h is the deformed drop height, V_0 is the electrode voltage, and $\Omega = h_0 l_0$, with h_0 and l_0 denoting the initial height (in y direction) and initial length (in x direction) of the drop. γ is the surface tension. ϵ_0 is the vacuum permittivity, and $\Delta \epsilon$ is the difference in the relative permittivity of the two fluids. $\delta = \frac{4d}{\pi}$ is a geometry parameter. In Figure 6(b) we show a comparison of the deformed drop height as a function of the electrode voltage between our simulation results and the theoretical model (83). While there exist some discrepancies in the quantitative values, the simulation results and the model are generally



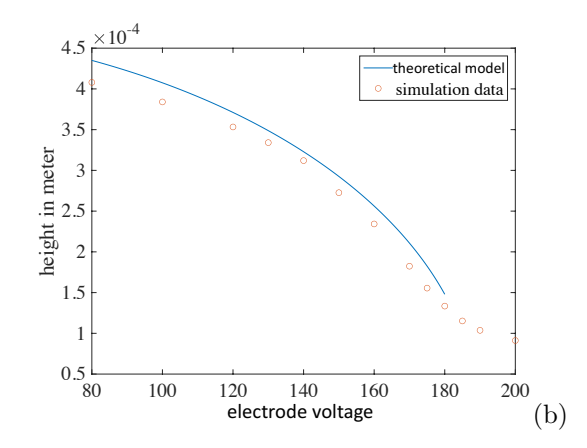
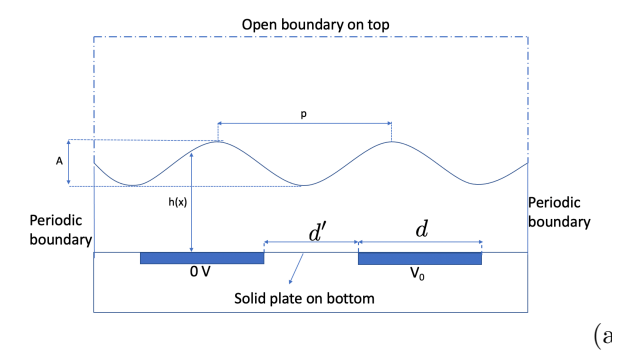


Figure 6: Dielectric drop on a wall: (a) the drop height/width/length as a function of the electrode voltage. (b) Comparison between the theoretical model [8] and the current simulation on the drop height as a function of the electrode voltage.



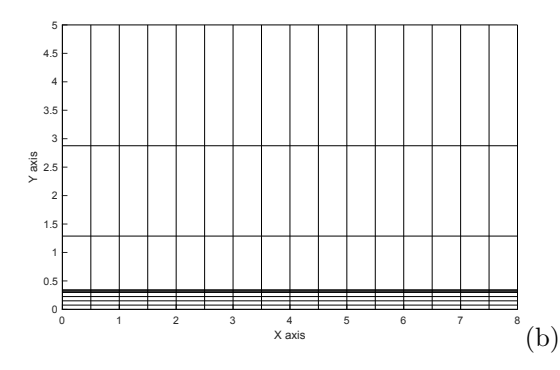


Figure 7: Dielectric thin film: (a) flow configuration and notation, (b) spectral-element mesh. The imposed voltage is 0 on the left electrode $(1 \le x \le 3)$ and V_0 on the right electrode $(5 \le x \le 7)$.

in reasonable agreement in the range $100 \le V_0 \le 180$ for the electrode voltage. It should be noted that the theoretical model (83) is only valid for a range of electrode voltage values (when $h \gg \delta$, see [8]). For the electrode voltage beyond about 180, the simulation result and the model prediction are qualitatively different. This discrepancy is due to the breakdown of the model equation (83). The trend exhibited by the simulation result in this region is similar to what has been observed in the experimental measurement [8].

4.3 Equilibrium Dielectric Film on a Surface

In this subsection we study the equilibrium state of a thin dielectric liquid film on a solid wall in two dimensions. The dielectric film exhibits a wave-like profile under an imposed electric field, as observed in the experiment [9], in which this is referred to as an optical interface.

The problem configuration and settings are illustrated in Figure 7(a). We consider a rectangular domain, $(x,y) \in \Omega = [0,4d] \times [0,\frac{5}{2}d]$, where d is the width of the electrode (see below). The domain and all the variables are assumed to be periodic in the horizontal (x) direction. The top of the domain is open, and the bottom of the domain is a solid wall. Two electrodes, each with a width d, are embedded on the bottom wall. The gap between the electrodes is d' = d. The two electrodes specifically occupy the regions $x \in [d/2, 3/2]$ and $x \in [5d/2, 7d/2]$ on the wall. The voltage imposed on the right electrode is V_0 , and on the left electrode is 0. A thin layer of dielectric fluid, with a thickness h_0 , is at rest on the bottom wall in an ambient fluid. When the electrodes are turned on, the fluid interface deforms under the imposed electric field and exhibits a wave-like profile at equilibrium. Our goal is to simulate the equilibrium dielectric fluid interface.

In what follows we provide two sets of simulations. The first set is obtained using the method from Section 2.4, based on the simpler system consisting of equations (17), (16c) and (16d). The second set, for

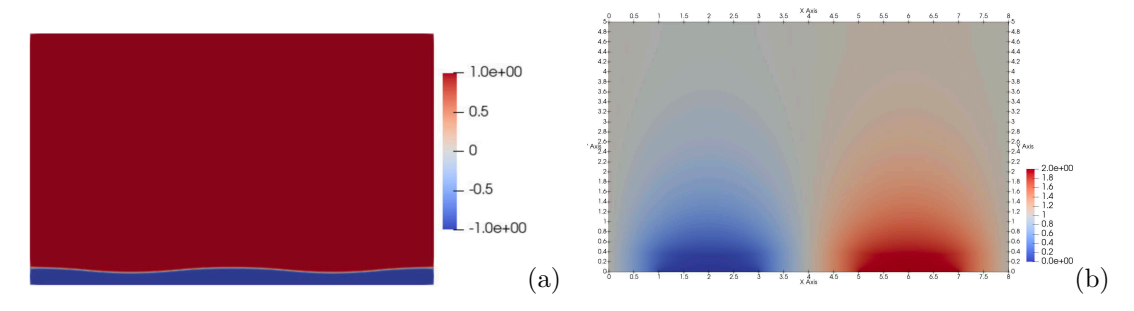


Figure 8: Dielectric thin film: Distributions of (a) the phase field function showing the fluid interface, and (b) the electric potential in the domain.

comparison, is based on the full model consisting of equations (3)–(7), together with appropriate boundary/initial conditions.

4.3.1 Equilibrium Simulation Using the Simpler System

We first simulate the equilibrium profile of the dielectric fluid interface using the method from Section 2.4, by solving the simpler system of (17), (16c) and (16d), with the boundary conditions as outlined in the above paragraphs.

We employ a surface tension $\gamma = 2.84 \times 10^{-2} kg/s^2$, and a permittivity for the ambient fluid the same as the vacuum permittivity, $\epsilon_1 = \epsilon_0$. The permittivity for the dielectric film (ϵ_2) is varied and will be specified below. All the variables and parameters are normalized based on the normalization constants in Table 2. Here we choose the length scale as $L_0 = \frac{d}{2}$, and the voltage scale as $V_d = 100$ volt. We use h(x) to denote the thickness of the equilibrium film at x.

Figure 7(b) shows a spectral element mesh employed in the current simulations. The elements are uniform in the x direction, and are generally non-uniform in y. Along the y direction we divide the domain into three regions: (i) near-wall region $(0 \le y \le h_0 - A/2)$, (ii) wave region $(h_0 - A/2 \le y \le h_0 + A/2)$, and (iii) upper region $(y \ge h_0 + A/2)$, where A is the peak-to-valley amplitude of the wave profile (see Figure 7(a)). For setting up the simulations, the amplitude A in the above is estimated based on the following theoretical model formula from [9],

$$A = \frac{16\epsilon_0}{3\pi^4\gamma} (\epsilon_1 - \epsilon_2) \exp\left(-\frac{2\pi h_0}{p}\right) V_0^2, \tag{84}$$

where p = d + d' = 2d. We employ N_{y_1} , N_{y_2} and N_{y_3} spectral elements in these three regions respectively along the y direction. The mesh is uniform in the near-wall and wave regions, and is non-uniform in the upper region (Figure 7(b)). The specific values for N_{y_1} , N_{y_2} and N_{y_3} will be provided below when discussing different simulation cases.

In all the simulations we employ a pseudo-time step size $\Delta t = 2.0 \times 10^{-6}$, Cahn number $\eta = 0.01$, and a mobility γ_1 by $\lambda \gamma_1 = 0.1$, where $\lambda = \frac{3}{2\sqrt{2}}\eta$. The initial phase field distribution is

$$\phi(x,y) = \tanh\left(\frac{y - h_0}{\sqrt{2}\eta}\right). \tag{85}$$

It should be noted that, while the physical length scale may be different for different simulation cases, the normalized computational domain is fixed due to the choice $L_0 = d/2$ and is always $(x, y) \in \Omega = [0, 8] \times [0, 5]$.

Figure 8 provides an overview of the equilibrium distributions of the phase field function ϕ (plot (a)) and the electric potential field V (plot (b)). The wavy fluid interface is unmistakable from Figure 8(a). This figure also illustrates that the domain dimension in y is much larger than the dielectric film thickness in our simulations. This is necessary because in the upper open boundary we have used the boundary condition (20), which is accurate only when the height of the computational domain is sufficiently large compared with the size of the electrode.

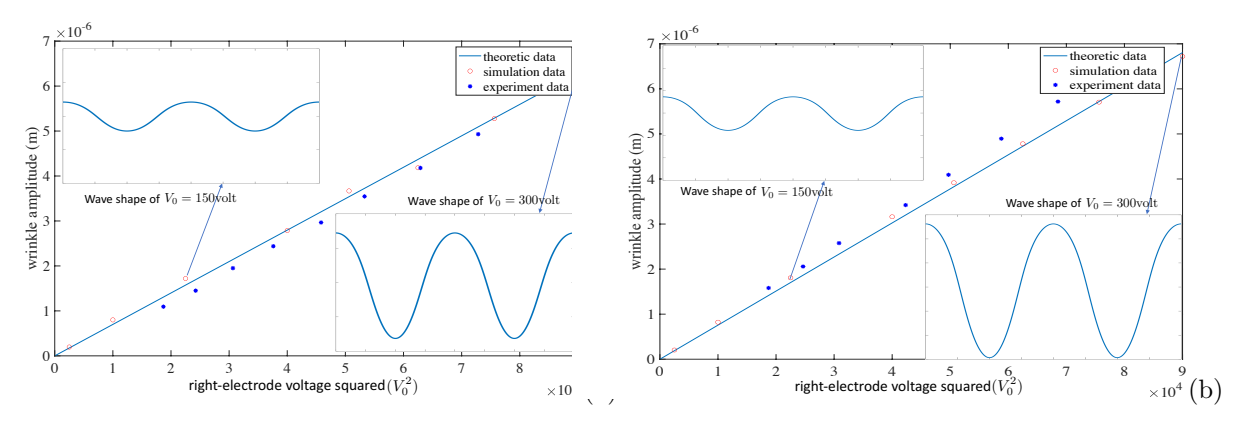


Figure 9: Dielectric thin film: Comparison of the amplitude (A) as a function of the electrode voltage squared (V_0^2) from the current simulations, the theoretical model (equation (84)), and the experimental measurement [9], for two cases with (a) $h_0 = 14\mu m$ and $p = 160\mu m$, and (b) $h_0 = 18\mu m$ and $p = 240\mu m$. The insets of these plots show two typical interface profiles.

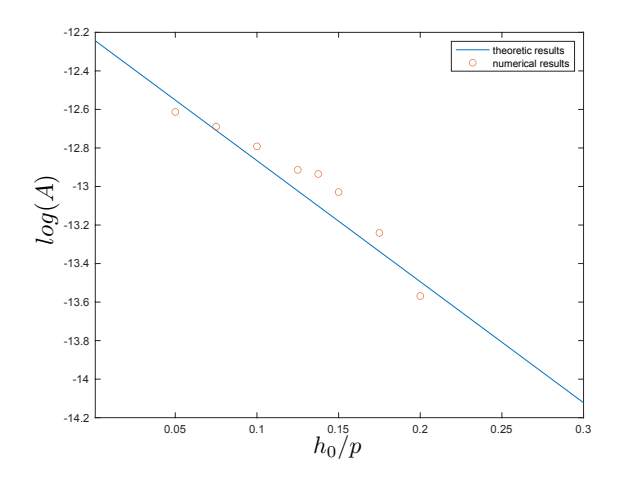


Figure 10: Dielectric thin film: Comparison of $\log(A)$ (interfacial wave amplitude) versus h_0/p (initial film thickness) from the current simulations and the theoretical model equation (84).

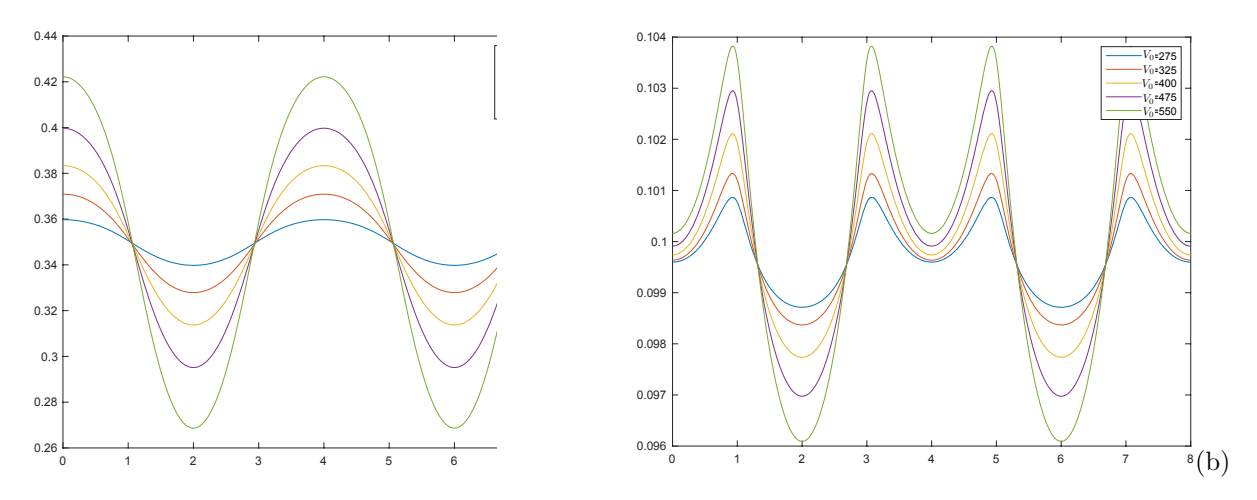


Figure 11: Dielectric thin film: Interfacial profiles at different electrode voltages: (a) sinusoidal-like profiles, (b) non-sinusoidal like profiles. In (a), $h_0=14\mu m,\ p=160\mu m,\ \text{and}\ \frac{\epsilon_2}{\epsilon_1}=8.$ In (b), $h_0=6\mu m,\ p=240\mu m,\ \text{and}\ \frac{\epsilon_2}{\epsilon_1}=2.$

Figure 9 is a comparison of the equilibrium interfacial amplitudes obtained from the current simulations, the theoretical model formula (84), and the experimental measurement of [9]. Here the initial film thickness (h_0) and the electrode width (d) are fixed, while the voltage on the right electrode (V_0) is varied systematically. The permittivity ratio is $\frac{\epsilon_2}{\epsilon_1} = 8$. We employ $(N_{y_1}, N_{y_2}, N_{y_3}) = (5, 4, 4)$ elements along the y direction in this set of simulations, with an element order 12 for all the elements. The two plots in this figure show the equilibrium interfacial amplitude as a function of V_0^2 for two cases, corresponding to $h_0 = 14\mu m$ and $p = 160\mu m$ (Figure 9(a)) and $h_0 = 18\mu m$ and $p = 240\mu m$ (Figure 9(b)), respectively. The insets of these plots depict two typical interfacial profiles at equilibrium corresponding to $V_0 = 150$ and 300 volts. It can be observed that the simulation results agree with the theoretical model and with the experimental data reasonably well.

Figure 10 shows another comparison between the current simulation and the theoretical model (84). In this set of simulations we have a fixed $V_0 = 200$ volt, $p = 160\mu m$ and $\epsilon_2/\epsilon_1 = 8$, while the initial thickness of the film is varied systematically. We again employ $(N_{y_1}, N_{y_2}, N_{y_3}) = (5, 4, 4)$ elements along the y direction. This figure plots the $\log(A)$ as a function of h_0/p from these tests. While there are some discrepancies, the simulation results overall are close to the predictions of the theoretical model equation (84).

As observed in the experiments of [9] and in the boundary integral model of [11], the interfacial profiles that are sinusoidal-like or non-sinusoidal-like can occur under the imposed electric field. We have observed both types of profiles in our simulations. Figure 11 shows examples of these two types of interfacial profiles attained from our simulations, corresponding to several electrode voltage values. Figure 11(a) corresponds to the case in Figure 9(a) (with $h_0 = 14\mu m$, $p = 160\mu m$ and $\epsilon_2/\epsilon_1 = 8$), exhibiting a sinusoidal wave-like profile. Figure 11(b) corresponds to the parameter values $h_0 = 6\mu m$, $p = 240\mu m$ and $\epsilon_2/\epsilon_1 = 2$, exhibiting an apparently non-sinusoidal wave-like profile.

4.3.2 Comparison with Full-Model Simulation

We now simulate the equilibrium profile of the dielectric fluid interface using the full model as given by the Equations (3)–(7), together with the boundary and initial conditions. The flow configuration and the problem setting follow those of Section 4.3.1, as given in Figure 7.

We consider the same group of tests as in Figure 9(a). The values for the physical and geometric parameters, such as the surface tension γ , the permittivities (ϵ_1 and ϵ_2), h_0 and p, are taken to be the same as in Section 4.3.1 (specifically Figure 9(a)). The only difference lies in the fluid densities and the dynamic viscosities, which are needed in the full model but do not appear in the simpler model of Section 4.3.1. Here in the full model we employ $\rho_1 = \rho_2 = 830kg/m^3$ for the two densities, and $\mu_1 = 1.2048 \times 10^{-5}kg/(m \cdot s)$ and $\mu_2 = 2\mu_1$ for the two dynamic viscosities. Employing the same density for the two fluids apparently does not correspond to realistic situations. Since we are seeking the equilibrium solution, employing the same density in principle will not alter the solution at equilibrium, but will make the computation considerably easier. All the physical variables and parameters have been normalized consistently.

In the full-model simulations, we employ the following simulation parameter values (non-dimensional): Cahn number $\eta = 0.01$, mobility $\gamma_1 = 0.05$, $\Delta t = 2 \times 10^{-6}$, the number of elements in the three regions along $y(N_{y_1}, N_{y_2}, N_{y_3}) = (5, 4, 4)$, and an element order 12. The initial phase field profile is given by (85). The electrode voltage V_0 is varied in the tests. The simulations have been performed for a sufficiently long time until the velocity becomes very small.

Figure 12 shows a comparison of the equilibrium interfacial profiles obtained by the simpler model of Section 4.3.1 and by the full model here. These profiles correspond to several electrode voltages ranging from $V_0 = 150$ volt to $V_0 = 275$ volt. The results from the simpler model and the full model in general agree very well, with their profiles essentially overlapping with each other. At larger electrode voltages (e.g. $V_0 = 275$ volt), some discrepancy in the valley (or peak) of the interfacial profile can be noticed between these two models.

Figure 13 is another comparison between the simpler model and the full model. It shows the interfacial amplitude A (see Figure 7(a)) as a function of the electrode voltage squared (V_0^2) obtained from the simpler model, the full model, and the theoretical model (84). It can be observed that the results from the simpler model and the full model agree well with each other, and that both are in good agreement with the theoretical model (84).

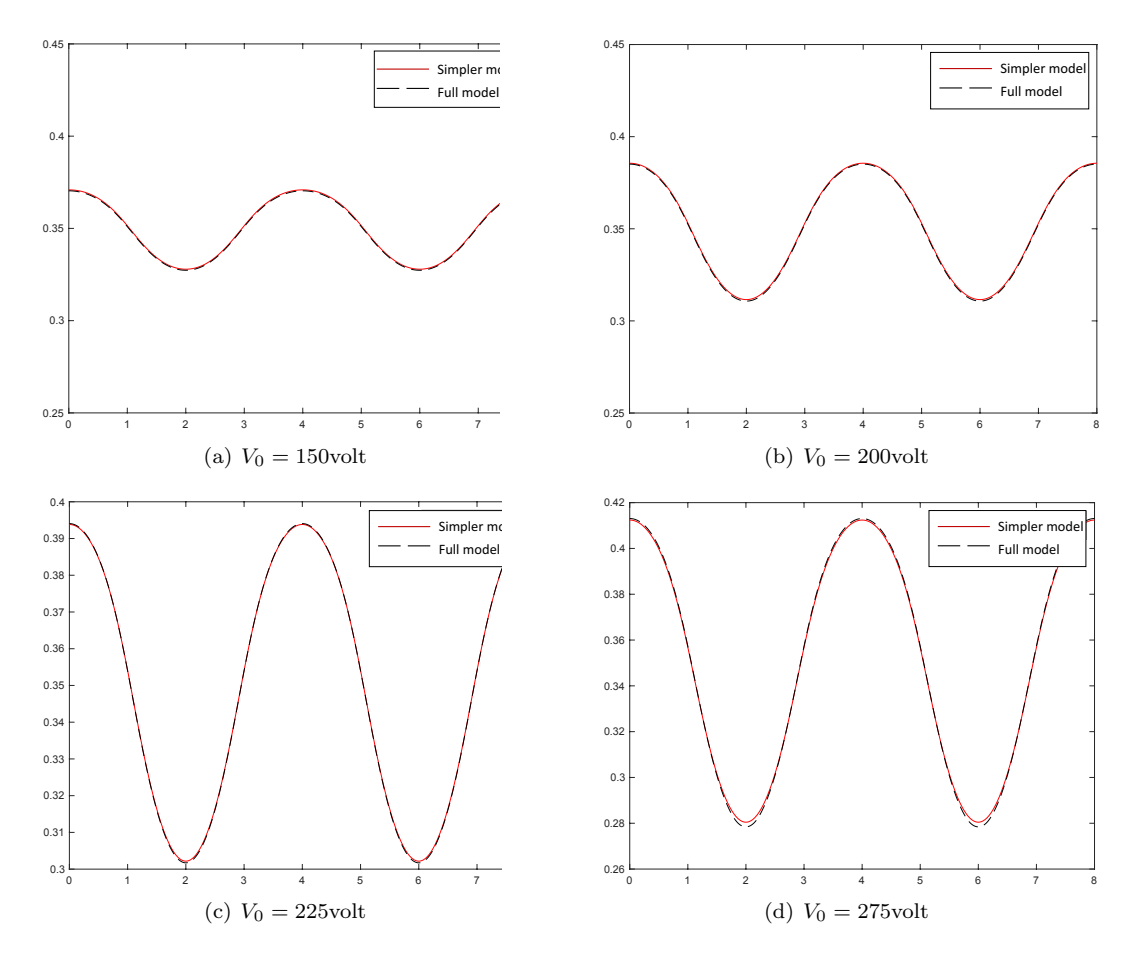


Figure 12: Dielectric thin film: Comparison of equilibrium interfacial profiles at several electrode voltages obtained from equilibrium simulations based on the simpler model of Section 2.4 and based on the full model.

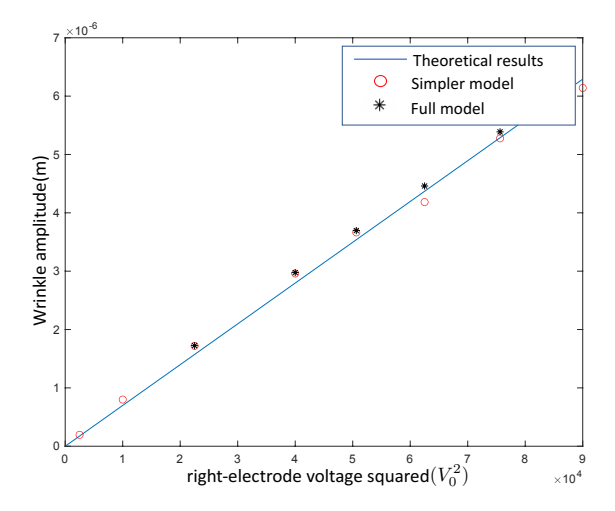


Figure 13: Dielectric thin film: Comparison of the interfacial amplitude versus the electrode voltage squared obtained from the equilibrium simulations based on the simpler model and the full model, and from the theoretical model (84).

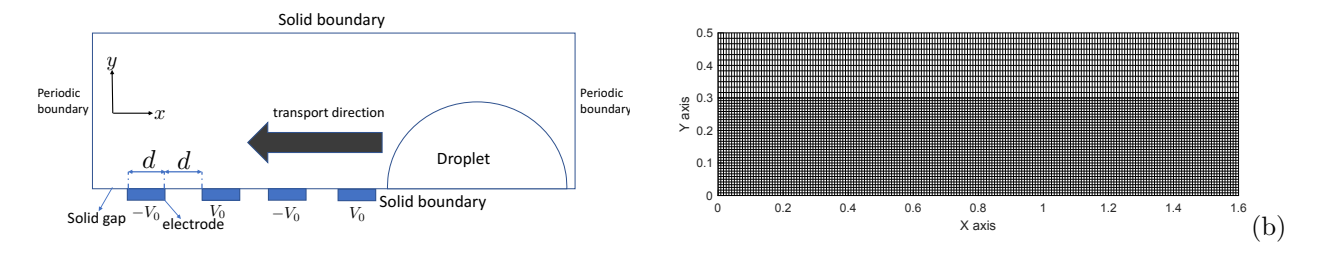


Figure 14: Drop transport: (a) Flow configuration and settings. (b) Mesh of 9216 non-uniform spectral elements.

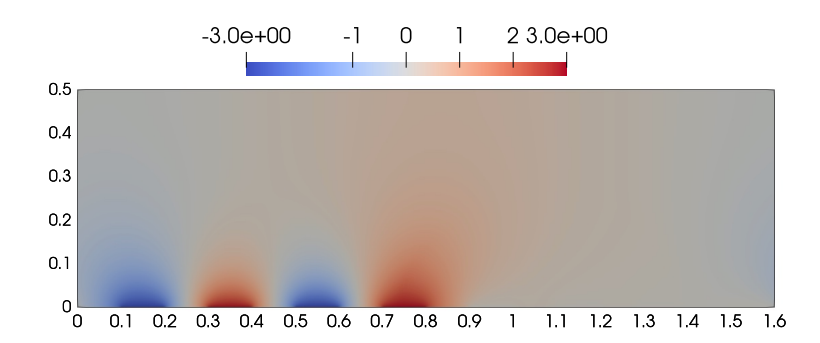


Figure 15: Drop transport: Distribution of the electric potential (t = 0.0).

4.4 Dynamic Simulations

The simulations in Sections 4.2 and 4.3 are for steady-state problems. In this section we further test the proposed method using dynamic problems with two-phase dielectric flows.

4.4.1 Transport of a Dielectric Drop on a Wall

We study the transport of a dielectric fluid drop on a horizontal wall in two dimensions in this subsection. The problem setting is illustrated by Figure 14(a). Consider a rectangular domain, which is periodic in the horizontal direction, open on the top, and has a solid wall at the bottom. An array of electrodes is embedded on the left half of the bottom wall, while the right half of the wall is free of electrodes. A dielectric liquid drop is initially at rest in the electrode-free region of the wall. When the electrodes are switched on, the drop will be pulled leftwards to the electrode-embedded region of the wall, due to its interaction with the nonuniform electric field. The goal of this problem is to simulate the motion of the liquid drop.

We employ the model given by equations (3)–(7) to simulate this problem, with the boundary and initial conditions as described below. We consider a computational domain, $(x,y) \in \Omega = [0, \frac{8}{5}L_0] \times [0, \frac{1}{2}L_0]$, where $L_0 = 1mm$. Figure 14(b) shows the mesh of 9216 non-uniform quadrilateral spectral elements employed in the simulations, with 192 and 48 elements along the x and y directions, respectively. Four electrodes are embedded on the bottom wall, with a voltage V_0 or $-V_0$, where $V_0 = 300$ volt. The electrode-embedded regions on the wall are: $x/L_0 \in [0.1, 0.2]$ (voltage $-V_0$), $x/L_0 \in [0.3, 0.4]$ (voltage V_0), $x/L_0 \in [0.5, 0.6]$ (voltage $-V_0$), and $x/L_0 \in [0.7, 0.8]$ (voltage V_0). We impose the boundary conditions (21)–(23) on the bottom wall $(y/L_0 = 0)$, with a static contact angle $\theta_s = 90^0$. The boundary conditions (18)–(20) are imposed on the top domain boundary $(y/L_0 = 0.5)$. We impose periodic boundary conditions for all the dynamic variables on the horizontal boundaries $(x/L_0 = 0, 1.6)$. The drop is assumed to be semi-circular initially, with a radius $R_0 = 0.28L_0$ and its center located at $(x_0, y_0) = (1.2L_0, 0)$. We employ an initial phase field profile,

$$\phi(x, y, t = 0) = \tanh \frac{\sqrt{(x - x_0)^2 + (y - y_0)^2} - R_0}{\sqrt{2}\eta},$$
(86)

and zero initial velocity in the simulations.

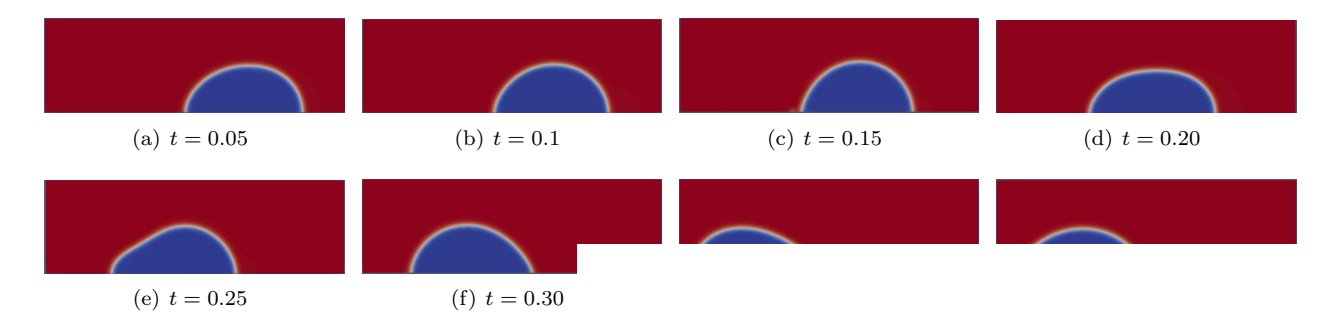


Figure 16: Drop transport: A temporal sequence Shown are the distributions of the phase field fund

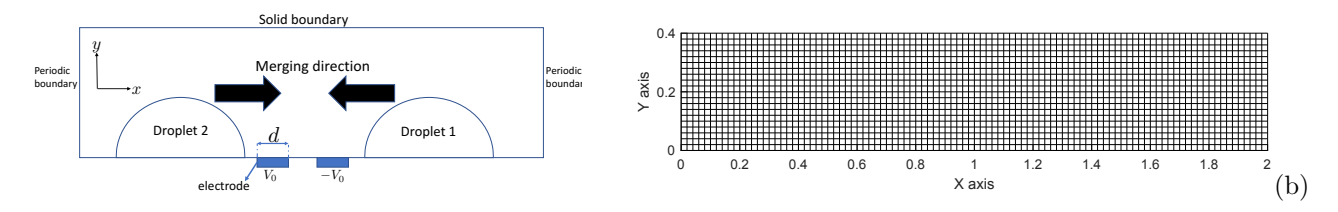


Figure 17: Drop coalescence: (a) Flow configuration and settings. (b) Mesh of 2000 quadrilateral spectral elements.

The following physical parameters are employed for this problem:

$$\begin{cases} \text{surface tension: } \gamma = 2.84 \times 10^{-2} kg/s^2; \\ \text{densities: } \rho_1 = \rho_2 = 429.7 kg/m^3; \text{ (ambient fluid } \rho_1, \text{ drop } \rho_2) \\ \text{dynamic viscosities: (ambient fluid) } \mu_1 = 12.048 \times 10^{-4} kg/(m \cdot s), \quad (\text{drop) } \mu_2 = 2\mu_1; \\ \text{permittivities: (ambient fluid) } \epsilon_1 = \epsilon_0 = 8.854 \times 10^{-12} F/m, \quad (\text{drop) } \epsilon_2 = 8.1\epsilon_0; \\ \text{model parameters: } \eta = 0.01 L_0, \quad \lambda = \frac{3}{2\sqrt{2}} \gamma \eta, \quad \gamma_1 = 1 \times 10^{-4} \frac{L_0^2}{\mu_1}, \quad \Delta t = 1 \times 10^{-6} \frac{L_0^2 \mu_1}{\epsilon_0 V_0^2}. \end{cases}$$

All the physical variables and parameters are normalized consistently based on the normalization constants listed in Table 1, with L_0 and ϵ_0 as given above and the μ_0 and V_d therein given by $\mu_0 = \mu_1$ and $V_d = V_0$ for this problem. We employ an element order 6 in the simulations.

Figures 15 and 16 provide an overview of the electric potential distribution in the domain and the motion of the dielectric drop on the bottom wall. Shown in Figure 16 are a temporal sequence of snapshots of the phase field function $\phi(x,y,t)$ in the domain. One can observe that the dielectric drop moves leftward along the wall due to the interaction with the imposed electric field, and approaches an equilibrium state resting on top of the electrodes.

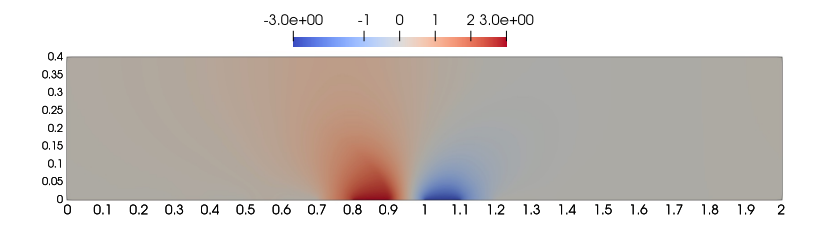


Figure 18: Drop coalescence: distribution of the electric potential field (t = 0.0).

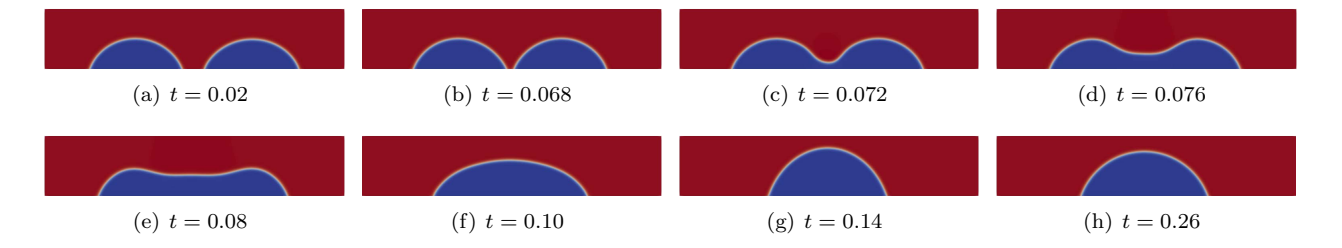


Figure 19: Drop coalescence: a temporal sequence of snapshots of the phase field distribution, showing the motion and coalescence of the two dielectric fluid drops.

4.4.2 Coalescence of Two Dielectric Liquid Drops

We study the motion and coalescence of two dielectric fluid drops in this subsection. Figure 17(a) sketches the flow configuration and problem setting. We again consider a rectangular domain, periodic in the horizontal direction, open at the top, and with a solid wall at the bottom. Two electrodes are embedded in the middle of the bottom wall, whose imposed voltages have the same magnitude but with opposite signs. Two liquid drops of the same dielectric fluid, initially at rest in the electrode-free regions of the wall, are pulled toward each other when the electrodes are turned on, and merge into a single drop. Our goal is to simulate this process with the proposed method.

The simulation settings and the boundary conditions are similar to those employed in Section 4.4.1. We employ a computational domain $(x,y) \in \Omega = [0,2L_0] \times [0,\frac{2}{5}L_0]$, where $L_0 = 1mm$, and the phase field model given by the equations (3)–(7). Figure 17(b) shows the mesh of 2000 quadrilateral spectral elements (with an element order 8) employed in the simulations. The two electrodes occupy the following regions on the wall: $x/L_0 \in [0.8, 0.9]$ (with voltage V_0), and $x/L_0 \in [1, 1.1]$ (with voltage $-V_0$), where $V_0 = 300$ volt. The boundary conditions (21)–(23) are imposed on the bottom wall, with a static contact angle $\theta_s = 75^0$ (measured on the side of the fluid drop). The boundary conditions (18)–(20) are imposed on the top boundary $(y/L_0 = 0.4)$. Periodic conditions are imposed on the horizontal boundaries $(x/L_0 = 0, 2.0)$ for all the dynamic variables. Both drops are assumed to be shaped like a circular cap initially, with radius R_0 and their centers located at (X_1, Y_1) and (X_2, Y_2) , respectively, as given by

$$R_0/L_0 = \frac{0.3}{\sin \theta_s}, \quad X_1/L_0 = 0.6, \quad Y_1 = -R_0 \cos \theta_s, \quad Y_2/L_0 = 1.4, \quad Y_2 = -R_0 \cos \theta_s.$$
 (88)

The initial phase field distribution is

$$\phi(x, y, t = 0) = \tanh \frac{\sqrt{(x - X_1)^2 + (y - Y_1)^2} - R_0}{\sqrt{2}\eta} + \tanh \frac{\sqrt{(x - X_2)^2 + (y - Y_2)^2} - R_0}{\sqrt{2}\eta} - 1, \quad (89)$$

where η is the characteristic interfacial thickness. The initial velocity is set to zero.

We employ the following physical and simulation parameters for this problem:

Surface tension:
$$\gamma = 1.136 \times 10^{-1} kg/s^2$$
;
densities: $\rho_1 = \rho_2 = 129.7 kg/m^3$; (ambient fluid ρ_1 , drop ρ_2)
dynamic viscosities: (ambient fluid) $\mu_1 = 12.048 \times 10^{-4} kg/(m \cdot s)$, (drop) $\mu_2 = 2\mu_1$;
permittivities: (ambient fluid) $\epsilon_1 = \epsilon_0 = 8.854 \times 10^{-12} F/m$, (drop) $\epsilon_2 = 8.1\epsilon_0$; (90)
static contact angle: $\theta_s = 75^0$ (measured on the drop side);
model parameters: $\eta = 0.007L_0$, $\lambda = \frac{3}{2\sqrt{2}}\gamma\eta$, $\gamma_1 = 5 \times 10^{-5} \frac{L_0^2}{\mu_1}$, $\Delta t = 1 \times 10^{-6} \frac{L_0^2 \mu_1}{\epsilon_0 V_0^2}$.

The physical variables and parameters in the system are normalized based on those constants given in Table 1, in which L_0 and ϵ_0 are as given above and we set $\mu_0 = \mu_1$ and $V_d = V_0$.

Figure 18 shows the distribution of the electric potential in the domain, signifying a non-uniform potential and thus a non-uniform electric field. The electric field is stronger near the electrodes, and is weaker in the

region farther away from the electrodes. As a result, the net Korteweg-Helmholtz force $(-\frac{1}{2}(\mathbf{E} \cdot \mathbf{E})\nabla \epsilon)$ acting on the dielectric drops has a direction pointing toward the electrodes, which causes the drops to move inward toward each other.

Figure 19 shows a temporal sequence of snapshots of the phase field distribution in the domain. It can be observed that the two drops move along the wall and merge with each other to form a single drop, which approaches an equilibrium state resting on top of the electrodes.

5 Concluding Remarks

We have developed a method for modeling and simulating multiphase flows consisting of two immiscible incompressible dielectric fluids, and their interactions with external electric fields in two and three dimensions. We first presented a thermodynamically-consistent and reduction-consistent formulation based on the phase-field framework for modeling two-phase dielectric fluids. The model respects the mass and momentum conservations, and the second law of thermodynamics. When only one fluid component is present, the two-phase formulation reduces exactly to that for the single-phase system. In particular, the presented model accommodates an equilibrium solution that is compatible with the requirement of zero velocity based on physics. This property leads to a simpler method for simulating two-phase dielectric systems at equilibrium, by solving a much simplified system consisting of the phase field equation and the electric potential equation only.

We have further presented an efficient semi-implicit type algorithm, together with a spectral-element discretization for 2D and a hybrid Fourier-spectral/spectral-element discretization for 3D in space, for simulating this class of problems. This algorithm allows the computation of different dynamic variables successively in an uncoupled fashion. Upon discretization the algorithm involves only coefficient matrices that are constant and time-independent in the resultant linear algebraic systems, even when the physical properties of the two dielectric fluids (e.g. the permittivities, densities, viscosities) are different. This property is crucial and enables us to employ the combined Fourier spectral and spectral-element discretization and fast Fourier transforms (FFT) for 3D simulations.

We have tested the performance of the presented method using several two-phase dielectric problems at equilibrium or in dynamic evolution. The simulation results obtained using the current method have been compared with theoretical models and with experimental measurements. The numerical results signify that the method developed herein can capture the physics well, and that it provides an effective technique for simulating this class of problems.

Acknowledgments

This work was partially supported by the US National Science Foundation (DMS-2012415, CMMI-2029540).

6 Appendix: Model Development and Further Numerical Tests

6.1 Development of Phase Field Model for Two-Phase Dielectric Flows

We outline below the derivation of the phase field model for two-phase dielectric fluids based on the conservation laws and thermodynamic principles. Much of this development builds upon the works of [1, 19].

Mass Conservation We consider a system of two immiscible incompressible dielectric fluids, and let ρ_1, ρ_2 denote the constant densities of these two pure fluids (without mixing). Consider an arbitrary control volume V_c of the mixture, with mass M. Let M_1 and M_2 denote the mass of these two fluids within V_c . Then $\hat{\rho}_1 = \frac{M_1}{V_c}$ and $\hat{\rho}_2 = \frac{M_2}{V_c}$ denote the densities of the two phases within the mixture. Naturally, we can introduce the mixture density ρ ,

$$\rho = \frac{M}{V_c} = \frac{M_1 + M_2}{V_c} = \hat{\rho}_1 + \hat{\rho}_2 \tag{91}$$

Let V_1 and V_2 denote the volume occupied by each pure fluid component with mass M_1 and M_2 . We assume that when forming the mixture there is no volume loss or volume addition, i.e.

$$V_c = V_1 + V_2$$
 (92)

We introduce the volume fraction of each fluid by, $\phi_i = \frac{V_i}{V_c} = \frac{M_i/\rho_i}{M_i/\hat{\rho}_i} = \frac{\hat{\rho}_i}{\rho_i}$ (i = 1, 2). Note that $0 \le \phi_i \le 1$. Then equation (92) becomes

$$\phi_1 + \phi_2 = 1. \tag{93}$$

We define the phase field variable by, $\phi = \phi_1 - \phi_2$.

The mass conservation for each phase in the mixture is given by,

$$\frac{\partial \hat{\rho}_i}{\partial t} + \nabla \cdot \hat{\mathbf{J}}_i = 0, \quad i = 1, 2, \tag{94}$$

where $\hat{\mathbf{J}}_i$ is the mass flux of phase *i*. We introduce the velocity \mathbf{u}_i of each phase in the mixture by $\hat{\mathbf{J}}_i = \hat{\rho}_i \mathbf{u}_i$ (i = 1, 2). Then equation (94) is transformed into,

$$\frac{\partial \hat{\rho}_i}{\partial t} + \nabla \cdot (\hat{\rho}_i \mathbf{u}_i) = 0, \quad i = 1, 2. \tag{95}$$

We define the bulk mixture velocity \mathbf{u} by the volume average of the velocities of the two phases,

$$\mathbf{u} = \phi_1 \mathbf{u}_1 + \phi_2 \mathbf{u}_2. \tag{96}$$

Then it follows that

$$\nabla \cdot \mathbf{u} = \nabla \cdot \left(\frac{\hat{\rho}_1}{\rho_1} \mathbf{u}_1 + \frac{\hat{\rho}_2}{\rho_2} \mathbf{u}_2\right) = \nabla \cdot \left(\frac{\hat{\mathbf{J}}_1}{\rho_1} + \frac{\hat{\mathbf{J}}_2}{\rho_2}\right) = -\frac{\partial}{\partial t} \left(\frac{\hat{\rho}_1}{\rho_1} + \frac{\hat{\rho}_2}{\rho_2}\right) = -\frac{\partial}{\partial t} (\phi_1 + \phi_2) = -\frac{\partial 1}{\partial t} = 0, \quad (97)$$

where equation (93) has been used.

Equation (97) indicates the bulk mixture velocity as defined above is divergence free (see also [17, 1]). One can also use the mass fraction to define the bulk velocity (see e.g. [50]). However, in that case the bulk velocity will not be divergence free. In the current work we employ the volume-averaged velocity as the bulk mixture velocity, as given by (96).

Finally, the mass conservation in terms of the bulk density ρ is, by adding equation (94) for i=1,2,

$$\frac{\partial \rho}{\partial t} + \mathbf{u} \cdot \nabla \rho = -\nabla \cdot \tilde{\mathbf{J}},\tag{98}$$

where $\tilde{\mathbf{J}} = (\hat{\mathbf{J}}_1 - \hat{\rho}_1 \mathbf{u}) + (\hat{\mathbf{J}}_2 - \hat{\rho}_2 \mathbf{u})$. $\tilde{\mathbf{J}}$ denotes the total difference of the mass flux of different phases with respect to the bulk. It will be determined by an constitutive relation based on the energy inequality. Note that equation (91) implies $\rho = \frac{\rho_1 + \rho_2}{2} + \frac{\rho_1 - \rho_2}{2} \phi$. So equation (98) can be transformed into,

$$\frac{\partial \phi}{\partial t} + \mathbf{u} \cdot \nabla \phi = -\frac{2}{\rho_1 - \rho_2} \nabla \cdot \tilde{\mathbf{J}}. \tag{99}$$

Momentum Conservation Following [34, 1, 19], we assume that the inertia and the kinetic energy due to the relative motion of each fluid phase with respect to the bulk motion are negligible. The conservation of momentum for each fluid phase is represented by,

$$\frac{\partial(\hat{\rho}_i \mathbf{u}_i)}{\partial t} + \nabla \cdot (\hat{\rho}_i \mathbf{u}_i \mathbf{u}_i) = \nabla \cdot \mathbf{T}_i + \boldsymbol{\pi}_i, \quad i = 1, 2,$$
(100)

where \mathbf{T}_i is the stress tensor of the phase i, and $\boldsymbol{\pi}_i$ (i = 1,2) represents the interaction body force, with $\boldsymbol{\pi}_1 + \boldsymbol{\pi}_2 = 0$.

We rewrite the above equation into,

$$\frac{\partial(\hat{\rho}_{i}\mathbf{u})}{\partial t} + \nabla \cdot (\hat{\rho}_{i}\mathbf{u}\mathbf{u}) + \frac{\partial(\hat{\rho}_{i}(\mathbf{u}_{i} - \mathbf{u}))}{\partial t} + \nabla \cdot (\hat{\rho}_{i}(\mathbf{u}_{i} - \mathbf{u})(\mathbf{u}_{i} - \mathbf{u})) + \nabla \cdot (\hat{\rho}_{i}(\mathbf{u}_{i} - \mathbf{u})\mathbf{u}) + \nabla \cdot (\hat{\rho}_{i}\mathbf{u}(\mathbf{u} - \mathbf{u}_{i})) = \nabla \cdot \mathbf{T}_{i} + \boldsymbol{\pi}_{i}.$$
(101)

We omit the third and the fourth terms on the left hand side (LHS) based on the assumption that the inertia and the kinetic energy of the differential motion relative to the bulk are negligible. We move the term $\nabla \cdot (\rho_i \mathbf{u}(\mathbf{u} - \mathbf{u}_i))$ to the right hand side (RHS) and incorporate it into the $\nabla \cdot \mathbf{T}_i$ term to get,

$$\frac{\partial(\hat{\rho}_i \mathbf{u})}{\partial t} + \nabla \cdot (\hat{\rho}_i \mathbf{u} \mathbf{u}) + \nabla \cdot (\mathbf{J}_i \mathbf{u}) = \nabla \cdot \tilde{\mathbf{T}}_i + \boldsymbol{\pi}_i, \quad i = 1, 2,$$
(102)

where $\mathbf{J}_i = \hat{\mathbf{J}}_i - \hat{\rho}_i \mathbf{u}$ and $\tilde{\mathbf{T}}_i = \mathbf{T}_i - \hat{\rho}_i \mathbf{u}(\mathbf{u} - \mathbf{u}_i)$. Then we sum up equation (102) for all the phases,

$$\frac{\partial(\rho \mathbf{u})}{\partial t} + \nabla \cdot (\rho \mathbf{u}\mathbf{u}) + \nabla \cdot (\tilde{\mathbf{J}}\mathbf{u}) = \nabla \cdot \mathbf{T},\tag{103}$$

where **T** is a stress tensor with $\mathbf{T} = \tilde{\mathbf{T}}_1 + \tilde{\mathbf{T}}_2$, and we have used $\boldsymbol{\pi}_1 + \boldsymbol{\pi}_2 = 0$. In light of (98), this equation can be transformed into,

$$\rho \left(\frac{\partial \mathbf{u}}{\partial t} + \mathbf{u} \cdot \nabla \mathbf{u} \right) + \tilde{\mathbf{J}} \cdot \nabla \mathbf{u} = \nabla \cdot \mathbf{T}. \tag{104}$$

We assume that the the stress tensor T is symmetric, and re-write it into

$$\mathbf{T} = \frac{1}{3} (\operatorname{tr} \mathbf{T}) \mathbf{I} + \mathbf{S} = -p \mathbf{I} + \mathbf{S}, \tag{105}$$

where **I** denotes the identity tensor, **S** is a trace-free symmetric tensor, and $p = -\frac{1}{3} \text{tr} \mathbf{T}$ will be called the pressure. Then equation (104) becomes,

$$\rho \left(\frac{\partial \mathbf{u}}{\partial t} + \mathbf{u} \cdot \nabla \mathbf{u} \right) + \tilde{\mathbf{J}} \cdot \nabla \mathbf{u} = -\nabla p + \nabla \cdot \mathbf{S}. \tag{106}$$

The tensor S will be determined from a constitutive relation based on the energy inequality.

Quasi-Static Maxwell Equations We focus on a system of dielectric fluids, which are non-conductive and contain no free electric charge. The characteristic velocity in the system is negligible compared with the speed of light. On the other hand, we would like to take into account the fluid motion and the momentum transport. So this is an electro quasi-static system [16].

The quasi-static Maxwell equations are given by,

$$\nabla \cdot \mathbf{D} = 0,\tag{107a}$$

$$\nabla \times \mathbf{E} = \mathbf{0},\tag{107b}$$

$$\frac{\partial \mathbf{D}}{\partial t} = \nabla \times \mathbf{H},\tag{107c}$$

where **E** is the electric field, **D** is electric displacement field ($\mathbf{D} = \epsilon \mathbf{E}$, with ϵ denoting the material permittivity), and **H** is the magnetizing field. Equation (107a) indicates that there is no free charge in the system. Equation (107b) allows us to introduce the electric potential $V(\mathbf{x})$ by

$$\mathbf{E} = \nabla V. \tag{108}$$

Note that the equations (107a) and (107b) alone are sufficient to determine the electric field. Equation (107c) will not be solved in numerical simulations. But this equation plays an important role in deriving the energy balance relation. The magnetic field \mathbf{H} is weak based on the quasi-static assumption.

Energy Inequality and Constitutive Relations Let us now determine the forms of $\tilde{\mathbf{J}}$ and \mathbf{S} involved in the mass/momentum balance equations based on the second law of thermodynamics. We define the total energy of the system by,

$$E(t) = \int_{\Omega} \left[\frac{1}{2} \rho \mathbf{u} \cdot \mathbf{u} + F(\phi, \nabla \phi) + \frac{1}{2} \mathbf{D} \cdot \mathbf{E} \right] dV + \int_{\partial \Omega_s} \Theta(\phi) dS, \tag{109}$$

where Ω is an arbitrary domain, $\partial\Omega_s$ denotes the wall boundary, $\frac{1}{2}\mathbf{D}\cdot\mathbf{E}$ is the electric energy density, $F(\phi, \nabla\phi)$ is the phase-field free energy density function (see e.g. (9)), and $\Theta(\phi)$ denotes a wall energy density to account for the contact angle effect. We assume that mixture permittivity is a function of the phase field function, $\epsilon = \epsilon(\phi)$. By using equations (98), (104) and (107), we can derive

$$\frac{dE}{dt} = \int_{\Omega} \frac{\rho_{1} - \rho_{2}}{2} \nabla \left[\frac{\partial F}{\partial \phi} - \nabla \cdot \frac{\partial F}{\partial \nabla \phi} - \frac{\epsilon'}{2} \mathbf{E} \cdot \mathbf{E} \right] \cdot \tilde{\mathbf{J}} - \int_{\Omega} \left(\mathbf{T} + \frac{\partial F}{\partial \nabla \phi} \otimes \nabla \phi - \boldsymbol{\sigma}_{M} \right) : \nabla \mathbf{u}$$

$$- \int_{\partial \Omega} \left[\frac{\rho_{1} - \rho_{2}}{2} \left(\frac{\partial F}{\partial \phi} - \nabla \cdot \frac{\partial F}{\partial \nabla \phi} - \frac{\epsilon'}{2} \mathbf{E} \cdot \mathbf{E} \right) \tilde{\mathbf{J}} \cdot \mathbf{n} - \frac{1}{2} (\mathbf{u} \cdot \mathbf{u}) \tilde{\mathbf{J}} \cdot \mathbf{n} \right]$$

$$+ \int_{\partial \Omega} \left[\left(\mathbf{T} - \boldsymbol{\sigma}_{M} + \frac{\partial F}{\partial \nabla \phi} \otimes \nabla \phi \right) \cdot \mathbf{n} - F \mathbf{n} - \frac{1}{2} (\mathbf{u} \cdot \mathbf{u}) \mathbf{n} \right] \cdot \mathbf{u}$$

$$+ \int_{\partial \Omega} \left(\frac{\partial F}{\partial \nabla \phi} \cdot \mathbf{n} \right) \frac{\partial \phi}{\partial t} + \int_{\partial \Omega_{s}} \Theta'(\phi) \frac{\partial \phi}{\partial t} - \int_{\partial \Omega} (\mathbf{E} \times \mathbf{H}) \cdot \mathbf{n}. \tag{110}$$

where $\epsilon' = \frac{d\epsilon}{d\phi}$, and σ_M is the Maxwell stress tensor [43], given by

$$\sigma_M = \mathbf{D} \otimes \mathbf{E} - \frac{\epsilon}{2} (\mathbf{E} \cdot \mathbf{E}) \mathbf{I}.$$
 (111)

The second law of thermodynamics dictates that in the absence of external forces (including surface forces acting on the boundary) the system should be dissipative. This means that the contributions of the volume integral terms involved in the above equation to dE/dt should always be non-positive, while the contributions of the surface integral terms can be controlled if appropriate boundary conditions are imposed. We would like to choose the constitutive relations about $\tilde{\bf J}$ and $\bf T$ such that the requirements of the second law of thermodynamics are satisfied.

To ensure the non-positivity of the first volume integral on the RHS of (110), we choose the following constitutive relation,

$$\tilde{\mathbf{J}} = -\gamma_1 \frac{\rho_1 - \rho_2}{2} \nabla \left(\frac{\partial F}{\partial \phi} - \nabla \cdot \frac{\partial F}{\partial \nabla \phi} - \frac{\epsilon'}{2} \mathbf{E} \cdot \mathbf{E} \right), \tag{112}$$

where $\gamma_1 \geqslant 0$ is a non-negative constant or function.

Noting the symmetry of the tensors **T** and σ_M , the second volume integral on the RHS of (110) can be transformed into,

$$-\int_{\Omega} \left(\mathbf{T} - \boldsymbol{\sigma}_{M} + \frac{\partial F}{\partial \nabla \phi} \otimes \nabla \phi \right) : \nabla \mathbf{u}$$

$$= -\int_{\Omega} \left[\mathbf{T} - \boldsymbol{\sigma}_{M} + \frac{1}{2} \left(\frac{\partial F}{\partial \nabla \phi} \otimes \nabla \phi + \nabla \phi \otimes \frac{\partial F}{\partial \nabla \phi} \right) \right] : \frac{1}{2} \left(\nabla \mathbf{u} + \nabla \mathbf{u}^{T} \right)$$

$$-\int_{\Omega} \frac{1}{2} \left(\frac{\partial F}{\partial \nabla \phi} \otimes \nabla \phi - \nabla \phi \otimes \frac{\partial F}{\partial \nabla \phi} \right) : \frac{1}{2} \left(\nabla \mathbf{u} - \nabla \mathbf{u}^{T} \right)$$

$$= -\int_{\Omega} \left[\mathbf{S} - \tilde{\boldsymbol{\sigma}}_{M} + \tilde{\boldsymbol{\mathcal{F}}}_{\phi} \right] : \frac{1}{2} \left(\nabla \mathbf{u} + \nabla \mathbf{u}^{T} \right)$$

$$-\int_{\Omega} \frac{1}{2} \left(\frac{\partial F}{\partial \nabla \phi} \otimes \nabla \phi - \nabla \phi \otimes \frac{\partial F}{\partial \nabla \phi} \right) : \frac{1}{2} \left(\nabla \mathbf{u} - \nabla \mathbf{u}^{T} \right)$$

$$(113)$$

where we have used equations (97), (105) and (107), and

$$\begin{cases} \tilde{\boldsymbol{\sigma}}_{M} = \boldsymbol{\sigma}_{M} - \frac{1}{3} \left[\operatorname{tr} \boldsymbol{\sigma}_{M} \right] \mathbf{I}, \\ \tilde{\boldsymbol{\mathcal{F}}}_{\phi} = \boldsymbol{\mathcal{F}}_{\phi} - \frac{1}{3} \left[\operatorname{tr} \boldsymbol{\mathcal{F}}_{\phi} \right] \mathbf{I}, \quad \boldsymbol{\mathcal{F}}_{\phi} = \frac{1}{2} \left(\frac{\partial F}{\partial \nabla \phi} \otimes \nabla \phi + \nabla \phi \otimes \frac{\partial F}{\partial \nabla \phi} \right). \end{cases}$$
(114)

problem	dimension	wall-time/step (secs)	CPUs	number-elements	element-order
section 4.2	3D	4.21	6	120	12
section $4.3.1$	2D	0.15	2	336	12
section $4.3.2$	2D	0.38	2	336	12
section 4.4.1	2D	0.15	80	9216	6
section $4.4.2$	2D	0.05	64	2000	8

Table 3: Summary of computational cost (wall-time in seconds per time step or per pseudo-time step) and associated parameters for the test problems in the main text. In the problem of Section 4.2 the number and order of spectral elements given in the table are for the xy-plane, and 144 (Fourier) grid points are used in z direction.

We choose the following constitutive relation to ensure its non-positivity,

$$\mathbf{S} - \tilde{\boldsymbol{\sigma}}_M + \tilde{\boldsymbol{\mathcal{F}}}_{\phi} = \mu(\nabla \mathbf{u} + \nabla \mathbf{u}^T), \tag{115}$$

$$\frac{\partial F}{\partial \nabla \phi} \otimes \nabla \phi - \nabla \phi \otimes \frac{\partial F}{\partial \nabla \phi} = 0. \tag{116}$$

where $\mu \geqslant 0$ is a non-negative constant or function. Equation (116) is a condition that the free energy density function $F(\phi, \nabla \phi)$ must satisfy. Equation (115) provides the tensor **S**,

$$\mathbf{S} = \mu(\nabla \mathbf{u} + \nabla \mathbf{u}^T) + \left(\boldsymbol{\sigma}_M - \frac{1}{3}[\operatorname{tr}\boldsymbol{\sigma}_M]\mathbf{I}\right) - \left(\boldsymbol{\mathcal{F}}_{\phi} - \frac{1}{3}[\operatorname{tr}\boldsymbol{\mathcal{F}}_{\phi}]\mathbf{I}\right). \tag{117}$$

In light of equations (112), (117), (99), (106), (97), (107a) and (108), we can write down the system of governing equations as follows,

$$\frac{\partial \phi}{\partial t} + \mathbf{u} \cdot \nabla \phi = \nabla \cdot \left[\gamma_1 \nabla \left(\frac{\partial F}{\partial \phi} - \nabla \cdot \frac{\partial F}{\partial \nabla \phi} - \frac{\epsilon'}{2} \mathbf{E} \cdot \mathbf{E} \right) \right], \tag{118a}$$

$$\rho \left(\frac{\partial \mathbf{u}}{\partial t} + \mathbf{u} \cdot \nabla \mathbf{u} \right) + \tilde{\mathbf{J}} \cdot \nabla \mathbf{u} = -\nabla \cdot \left(\frac{\partial F}{\partial \nabla \phi} \otimes \nabla \phi \right) - \frac{\nabla \epsilon}{2} (\mathbf{E} \cdot \mathbf{E}) + \nabla \cdot \left[\mu \left(\nabla \mathbf{u} + \nabla \mathbf{u}^T \right) \right] - \nabla \mathcal{P}, \quad (118b)$$

$$\nabla \cdot \mathbf{u} = 0,\tag{118c}$$

$$\nabla \cdot (\epsilon \nabla V) = 0. \tag{118d}$$

In the above equations,

$$\mathcal{P} = p + \frac{1}{3} \operatorname{tr} \boldsymbol{\sigma}_{M} - \frac{1}{3} \operatorname{tr} \boldsymbol{\mathcal{F}}_{\phi}, \tag{119}$$

and we have used

$$\nabla \cdot \boldsymbol{\sigma}_{M} = \nabla \cdot \left[\mathbf{D} \otimes \mathbf{E} - \frac{\epsilon}{2} (\mathbf{E} \cdot \mathbf{E}) \mathbf{I} \right] = -\frac{\nabla \epsilon}{2} (\mathbf{E} \cdot \mathbf{E}). \tag{120}$$

This set of equations constitutes the phase field model that describes the motion of a system of two immiscible incompressible dielectric fluids. This model is thermodynamically consistent.

In this model the form for the mixing energy density function $F(\phi, \nabla \phi)$ is still to be chosen, and it must satisfy the condition (116). If we choose $F(\phi, \nabla \phi)$ based on equation (9), which satisfies the condition (116), then the system (118) will be reduced to the system consisting of equations (3)–(6).

6.2 Computational Cost

Table 3 summarizes the computational cost of our method for simulating the problems from Sections 4.2 to 4.4. We list the wall time in seconds per time step (for dynamic problems) or per pseudo-time step (for equilibrium problems), the number of CPUs used, the number and order of spectral elements for 2D or in the xy planes for 3D. Additional parameters for the test problems, if any, are provided in the table caption.

Element Order 2 L^{∞} -u error 6.68E-5 1.66E-5 4.03E-6 convergence order 2.01 2.04 L^{2} -u error 1.09E-5 2.40E-6 5.55E-7	128×128
	9.21E-7
L^2 -u error 1.09E-5 2.40E-6 5.55E-7	2.13
E 4 01101 1.00E 0 2.10E 0 0.00E 1	1.33E-7
convergence order 2.19 2.11	2.06
L^{∞} -p error 2.62E-2 6.56E-3 1.61E-3	4.01E-4
convergence order 2.00 2.03	2.00
L^2 -p error 4.21E-3 1.03E-3 2.55E-4	6.36E-5
convergence order 2.03 2.02	2.00
L^{∞} -V error 3.46E-2 8.99E-3 2.28E-3	5.73E-4
convergence order 1.95 1.98	1.99
L^2 -V error 1.01E-2 2.55E-3 6.42E-4	1.61E-4
convergence order 1.98 1.99	2.00
L^{∞} - ϕ error 7.32E-4 3.62E-4 1.20E-4	3.04E-5
convergence order 1.02 1.59	1.98
L^2 - ϕ error 1.66E-4 6.38E-5 5.77E-6	1.12E-6
convergence order 1.38 3.47	2.37
Element Order 4 L^{∞} -u error 7.27E-7 7.30E-8 2.17E-9	4.29E-11
convergence order 3.31 5.07	5.66
L^2 -u error 2.41E-8 1.65E-9 4.64E-11	2.76E-12
convergence order 3.87 5.15	4.07
L^{∞} -p error 3.69E-5 1.81E-6 1.11E-7	6.98E-9
convergence order 4.35 4.03	3.99
L^2 -p error $6.47E-6 3.24E-7 1.51E-8$	1.07E-9
	3.82
convergence order 4.32 4.42	5.69E-9
convergence order 4.32 4.42 L^{∞} -V error $2.25\text{E-}5$ $1.44\text{E-}6$ $9.07\text{E-}8$	4.00
L^{∞} -V error 2.25E-5 1.44E-6 9.07E-8 convergence order 3.96 3.99	4.00
$\begin{array}{c ccccc} L^{\infty}\text{-V error} & 2.25\text{E-5} & 1.44\text{E-6} & 9.07\text{E-8} \\ \text{convergence order} & 3.96 & 3.99 \\ \hline L^{2}\text{-V error} & 5.67\text{E-6} & 3.56\text{E-7} & 2.23\text{E-8} \\ \end{array}$	4.00 1.39E-9
$\begin{array}{c ccccccccccccccccccccccccccccccccccc$	1.39E-9 4.00
$\begin{array}{c ccccccccccccccccccccccccccccccccccc$	1.39E-9 4.00 1.87E-9
$\begin{array}{c ccccccccccccccccccccccccccccccccccc$	1.39E-9 4.00 1.87E-9 3.26
$\begin{array}{c ccccccccccccccccccccccccccccccccccc$	1.39E-9 4.00 1.87E-9

Table 4: h-refinement (2D): L^{∞} and L^2 errors and the convergence order corresponding to a series of spectral element meshes and two element orders. The analytic solution used in the test is given by equation (80).

It should be noted that the numerical tests in Sections 4.3.1 and 4.3.2 are for the same dielectric film problem, but computed using different methods, with the simpler method in Section 4.3.1 and with the full model in Section 4.3.2. The data in Table 3 show that the simpler method is much faster than the full model. We further note that the simpler method generally takes markedly fewer (pseudo) time steps to reach the equilibrium state than the full model simulation.

6.3 Convergence Test on the h-Refinement of Method

Section 4.1 illustrates the convergence of the current method as the spatial resolution or the time step size is varied. In those spatial convergence tests the element order is varied systematically, while the spectral element mesh is fixed. This approach to refine the resolution is often known as p-refinement. We next discuss the convergence of our method as the resolution is refined in another way, known as h-refinement, in which the element order is fixed while the mesh size is varied systematically.

We employ the 2D analytic solution (Equation (80)) from Section 4.1 for the h-refinement tests. We fix the element order at 2 (polynomial degree 1) or 4 (polynomial degree 3), the time step size at $\Delta t = 10^{-4}$ (for element order 2) and $\Delta t = 2 \times 10^{-6}$ (for element order 4), and integrate in time from t = 0 to $t = t_f = 2 \times 10^{-3}$.

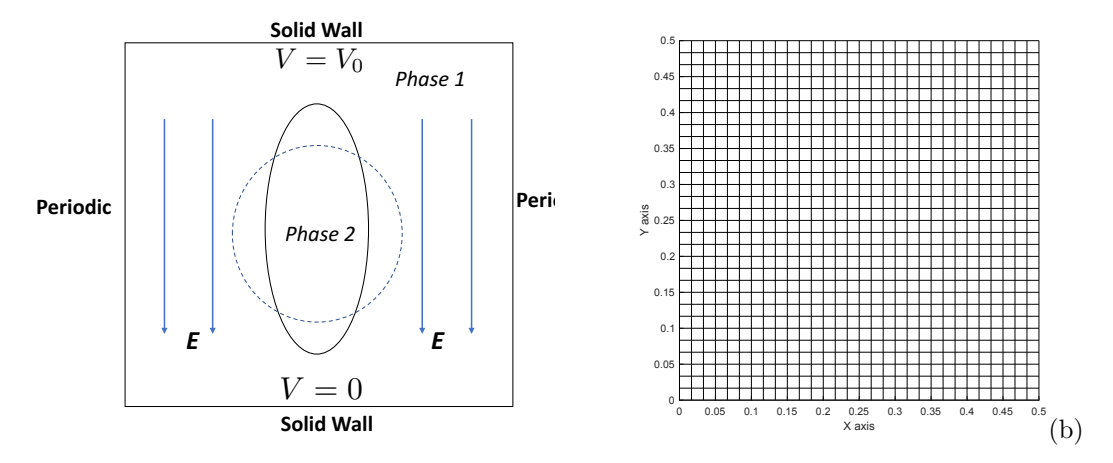


Figure 20: Equilibrium dielectric drop in a uniform electric field: (a) problem setting, (b) spectral element mesh with 900 quadrilateral elements.

We vary the number of uniform elements between 16×16 and 128×128 , doubling the elements in both directions during each refinement. Table 4 summarizes the L^{∞} and L^2 errors of different variables and the convergence order based on these errors. The convergence order is computed by $\frac{\ln(\varepsilon_1/\varepsilon_2)}{\ln(N_2/N_1)}$, where ε_1 and ε_2 are the errors before and after the refinement and N_1 and N_2 denote the corresponding number of elements along each direction. The data show that the convergence order for h-refinement approximately follows the element order, generally around 2.0 (resp. 4.0) for a fixed element order 2 (resp. 4). However, the convergence is not always regular, and some deviation from these expected convergence orders can be observed.

6.4 Numerical Tests on the Cahn Number and Mobility Parameter

This section tests the effects of the interfacial thickness (Cahn number) η and the mobility parameter γ_1 on the simulation results. We consider the equilibrium state and the oscillation of a dielectric drop in a uniform electric field in two dimensions.

6.4.1 Equilibrium Dielectric Drop in a Uniform Electric Field: Effect of Cahn Number

The current phase field equation contains an electric field term, unlike the standard Cahn-Hilliard equation. In the presence of external electric field, the equilibrium state differs from that of the Cahn-Hilliard system. For the standard Cahn-Hilliard equation, the equilibrium interfacial profile theoretically follows the tanh distribution [79]. For the current model, on the other hand, the equilibrium interfacial profile can no longer be attained theoretically due to the electric field. We next simulate the equilibrium interfacial profile of a dielectric drop in an electric field, and study the effect of the Cahn number. We compare the attained interfacial parameters with those of the tanh profile to show their similarities.

Figure 20(a) illustrates the problem setting. We consider a 2D square domain $\Omega = [0, 0.5L_0] \times [0, 0.5L_0]$, where $L_0 = 10^{-5}m$. The bottom and top of the domain are solid walls, with an voltage V = 0 and $V = V_0 = 50$ volt imposed respectively. A dielectric fluid drop, initially circular with a radius $0.1L_0$, is at rest in the center. The permittivities of the ambient fluid and the drop are $\epsilon_1 = 17.6\epsilon_0$ and $\epsilon_2 = 3.53\epsilon_0$, respectively, where ϵ_0 denotes the vacuum permittivity. The surface tension between the two fluids is $\gamma = 0.01N/m$. The dielectric drop deforms due to the electric field, and forms an oval at equilibrium. The goal is to simulate the equilibrium state of the drop and investigate the effect of the Cahn number.

We employ the simpler system (16) to simulate the dielectric drop, with a non-dimensional mobility $\gamma_1 = 0.01$ and a pseudo-time step size $\Delta t = 10^{-5}$. The initial phase field distribution is given by

$$\phi(x, y, t = 0) = \tanh \frac{\sqrt{(x - x_0)^2 + (y - y_0)^2} - R_0}{\sqrt{2}\eta},$$
(121)

where $(x_0, y_0) = (0.25, 0.25)$, $R_0 = 0.1$, and η is the Cahn number. A mesh of 900 quadrilateral elements (Figure 20(b)) with an element order 6 is employed in the simulations.

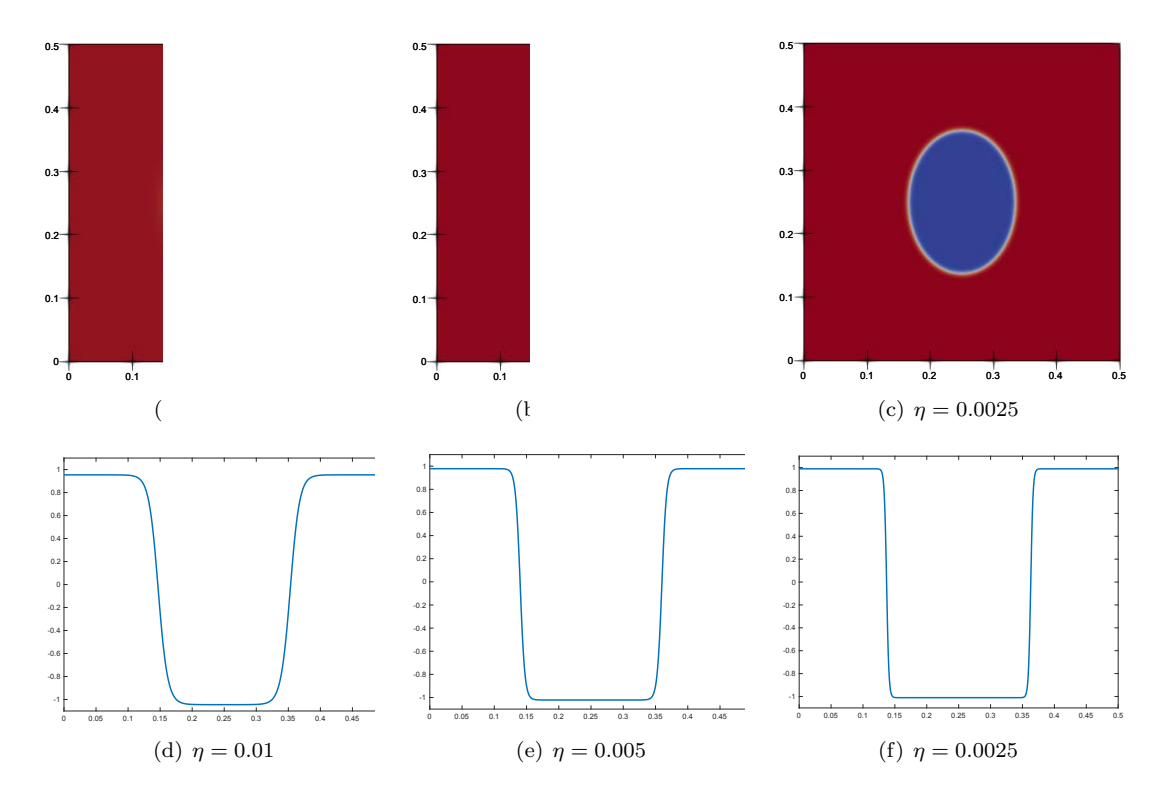
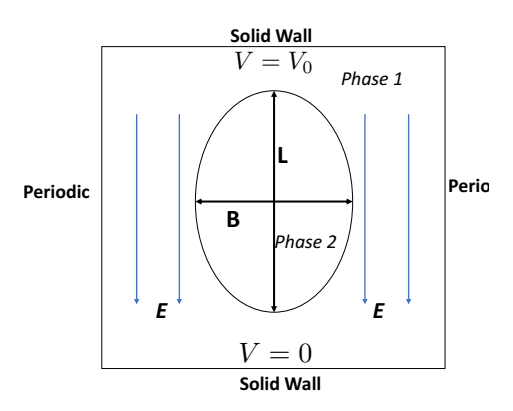


Figure 21: Dielectric drop in uniform electric field: Equilibrium phase field distribution (top row), and equilibrium profile of phase field along the vertical centerline (x = 0.25) of domain (bottom row), computed using three Cahn numbers $\eta = 0.01$, 0.005 and 0.0025.

	η	p = 0.95	p = 0.97	p = 0.99
simulation	0.0025	5.4	6.2	8.0
	0.005	5.2	6.0	7.6
	0.01	5.4	6.2	7.9
tanh profile	_	5.2	5.9	7.5

Table 5: Dielectric drop in uniform electric field: Comparison of interfacial thickness δ_p/η from the simulation and from the theoretical tanh profile, corresponding to several Cahn numbers. p denotes the threshold value used for defining the interfacial thickness δ_p . For the tanh profile $\delta_p/\eta = 2\sqrt{2} \tanh^{-1}(p)$.

Figure 21 shows the equilibrium distributions of the phase field ϕ , and the ϕ profiles along the vertical centerline (x=0.25), obtained using three Cahn numbers $\eta=0.01$, 0.005 and 0.0025. At equilibrium the dielectric drop is deformed, and as the Cahn number decreases the drop becomes more sharply defined. The interfacial profiles appear to resemble a tanh profile qualitatively. We can notice a shift from the expected ± 1 in the bulk value of ϕ , with the shift being smaller as η decreases, a phenomenon well-known with the phase field method [80]. Table 5 provides a quantitative comparison of the interfacial thickness between the simulation and the theoretical tanh profile. Here the interfacial thickness δ_p is defined as the thickness of the region $\left\{ \mathbf{x} = (x,y) \mid x=0.25, \ \middle| \phi(\mathbf{x}) - \frac{1}{2}(\phi_{\max} + \phi_{\min}) \middle| \leqslant \frac{p}{2}(\phi_{\max} - \phi_{\min}) \right\}$ along the centerline, where ϕ_{\max} and ϕ_{\min} are the maximum and minmum values of $\phi(\mathbf{x})$ in the bulk, respectively, and p<1 is a prescribed threshold value close to 1. For the tanh profile, the phase field distribution (in 1D) is given by $\phi(x) = \tanh \frac{x}{\sqrt{2\eta}}$ [79], leading to an interfacial thickness $\delta_p/\eta = 2\sqrt{2} \tanh^{-1}(p)$ based on the above definition. Table 5 lists the δ_p/η corresponding to three Cahn numbers and three threshold values p=0.95, 0.97 and 0.99, from our simulation and the tanh profile. The data suggest that the equilibrium profile of the dielectric drop obtained from our method is largely consistent with the tanh profile.



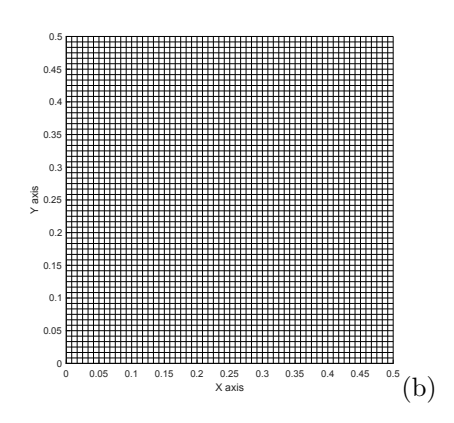


Figure 22: Transient dielectric drop in a uniform electric field: (a) Problem setting and configuration. (b) Spectral element mesh with 3600 elements. L and B denote the major and minor axes, respectively.

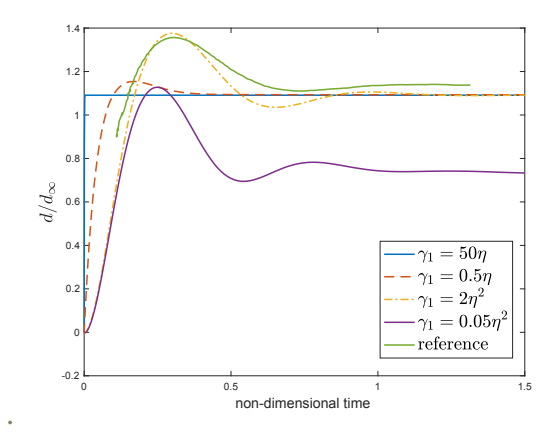


Figure 23: Transient dielectric drop in a uniform electric field: time histories of the deformation ratio d/d_{∞} computed with a range of values for the mobility γ_1 . Fixed Cahn number $\eta = 0.0025$. The reference curve is from [68].

6.4.2 Transient Dielectric Drop in a Uniform Electric Field: Effect of Mobility Parameter

We next illustrate the effect of the mobility γ_1 in the model on the transient process of a dielectric drop approaching the equilibrium state in an external electric field. The mobility is known to influence the computed dynamics with the phase field method [37, 38, 51, 52]. An inappropriate mobility may cause the fluid interface to deviate from the equilibrium profile significantly, leading to a convective distortion and instability [52]. The analyses in [51] suggest that the mobility should scale as $\gamma_1 \sim \eta^2$ in order for the phase field model to be consistent with the sharp interface limit. Our simulation is indicative of a relation consistent with this scaling.

We consider a problem setup similar to that of Section 6.4.1. But here we focus on the transient process as the drop deforms and approaches the equilibrium configuration, in a way similar to [68]. We simulate this dynamic process by the full phase field model (equations (3)–(7)) and investigate the effect of the mobility γ_1 . Figure 22(a) provides the problem configuration and the important parameters of the transient dielectric drop to be monitored. In particular, we record the time histories of the major and minor axes (L and B) of the drop and compute the deformation ratio d = (L - B)/(L + B). Following [68], this ratio is normalized by $d_{\infty} = \frac{R_0 \epsilon_0 \epsilon_1 V_0^2}{\sigma L_0^2} \frac{9(\epsilon_1/\epsilon_2 - 1)^2}{16(\epsilon_1/\epsilon_2 + 2)^2}$. The variables involved in this expression are explained below.

We choose the physical parameters in accordance with [68], and normalize them according to Table 1. The relevant parameters are $L_0=10^{-5}m$, $\epsilon_0=8.854\times 10^{-12}C/V\cdot m$, $\mu_0=0.001Pa\cdot s$, $V_d=100V$, $\rho_0=1000kg/m^3$, and the surface tension $\sigma=0.03N/m$. The non-dimensionalized simulation parameters include the densities $\rho_1=\rho_2=1$, viscosities $\mu_1=\mu_2=1$, the upper-wall voltage $V_0=0.5$, relative

permittivities $\epsilon_1 = 3$ and $\epsilon_2 = 80$, and the mixing energy density coefficient $\lambda = \frac{3}{2\sqrt{2}}\sigma\eta$. The drop is initially circular and at rest, with a radius $R_0 = 0.1$ and its center located at $(x_0, y_0) = (0.25, 0.25)$. The initial phase field distribution is given by (121), and we employ a zero initial velocity. Figure 22(b) shows the mesh, with 3600 quadrilateral elements and an element order 6.

Figure 23 depicts time histories of the deformation ratio corresponding to several mobility values ranging from $\gamma_1 = 0.05\eta^2$ to $\gamma_1 = 50\eta$. Here the Cahn number is fixed at $\eta = 0.0025$. This figure also shows the result from [68] as a reference. With a mobility around $\gamma_1 \sim \eta^2$, the deformation ratio oscillates around an equilibrium value (see the curve $\gamma_1 = 2\eta^2$), similar to [68]. With a mobility much larger than η^2 , the deformation ratio reaches its equilibrium value almost instantly and no oscillation is observed. The results indicate that the mobility values on the order η^2 or larger yield essentially the same equilibrium value for the deformation ratio. On the other hand, if γ_1 is significantly lower than η^2 , the deformation ratio exhibits an oscillation, but over time it can approach an equilibrium value that deviates significantly from that obtained with mobility about η^2 or larger. Overall these tests suggest that a mobility around η^2 appears to yield more reasonable dynamics. This is consistent with the theoretical analyses of [51]. In the simulations of this paper we have employed mobility values generally on the order of η^2 .

References

- [1] Helmut Abels, Harald Garcke, and Günther Grün. Thermodynamically consistent, frame indifferent diffuse interface models for incompressible two-phase flows with different densities. *Mathematical Models and Methods in Applied Sciences*, 22(03):1150013, 2012.
- [2] G.L. Aki, W. Dreyer, and J. Giesselmann. A quasi-incompressible diffuse interface model with phase transition. *Mathematical Models and Methods in Applied Sciences*, 24:827–861, 2014.
- [3] D.M. Anderson, G.B. McFadden, and A.A. Wheeler. Diffuse-interface methods in fluid mechanics. *Annual Review of Fluid Mechanics*, 30:139–165, 1998.
- [4] J.R. Baltzer and D. Livescu. Variable-density effects in incompressible non-buoyant shear-driven turbulent mixing layers. *Journal of Fluid Mechanics*, 900:A16, 2020.
- [5] JS Batchelder. Dielectrophoretic manipulator. Review of Scientific Instruments, 54(3):300–302, 1983.
- [6] Bruno Berge and Jérôme Peseux. Variable focal lens controlled by an external voltage: An application of electrowetting. *The European Physical Journal E*, 3(2):159–163, 2000.
- [7] Franck Boyer. A theoretical and numerical model for the study of incompressible mixture flows. Computers & fluids, 31(1):41–68, 2002.
- [8] Carl V Brown, Glen McHale, and Christophe L Trabi. Dielectrophoresis-driven spreading of immersed liquid droplets. *Langmuir*, 31(3):1011–1016, 2015.
- [9] CV Brown, GG Wells, MI Newton, and Glen McHale. Voltage-programmable liquid optical interface. Nature Photonics, 3(7):403-405, 2009.
- [10] E. Campillo-Funollet, G. Grun, and F. Klingbeil. On modeling and simulation of electrokinetic phenomena in two-phase flow with general mass densities. SIAM J. Appl. Math., 72:1899–1925, 2012.
- [11] David J Chappell and Reuben D O'Dea. Numerical-asymptotic models for the manipulation of viscous films via dielectrophoresis. *Journal of Fluid Mechanics*, 901, 2020.
- [12] D. Chugh and K.V.I.S. Kaler. Leveraging liquid dielectrophoresis for microfluidic applications. *Biomed. Mater.*, 3:34009, 2008.
- [13] D. Chung and D.I. Pullin. Direct numerical simulation and large-eddy simulation of stationary buoyancy-driven turbulence. *Journal of Fluid Mechanics*, 643:279–308, 2010.
- [14] Christopher G Cooney, Chao-Yi Chen, Michael R Emerling, Ali Nadim, and James D Sterling. Electrowetting droplet microfluidics on a single planar surface. *Microfluidics and Nanofluidics*, 2(5):435–446, 2006.
- [15] M.S. Day and J.B. Bell. Numerical simulation of laminar reacting flows with complex chemistry. *Combustion Theory and Modelling*, 4:535–556, 2000.
- [16] Marc De Montigny and Germain Rousseaux. On the electrodynamics of moving bodies at low velocities. European journal of physics, 27(4):755, 2006.
- [17] Hang Ding, Peter DM Spelt, and Chang Shu. Diffuse interface model for incompressible two-phase flows with large density ratios. *Journal of Computational Physics*, 226(2):2078–2095, 2007.

- [18] S Dong. On imposing dynamic contact-angle boundary conditions for wall-bounded liquid—gas flows. Computer Methods in Applied Mechanics and Engineering, 247:179–200, 2012.
- [19] S. Dong. An efficient algorithm for incompressible N-phase flows. *Journal of Computational Physics*, 276:691–728, 2014.
- [20] S. Dong. An outflow boundary condition and algorithm for incompressible two-phase flows with phase field approach. *Journal of Computational Physics*, 266:47–73, 2014.
- [21] S. Dong. Physical formulation and numerical algorithm for simulating N immiscible incompressible fluids involving general order parameters. *Journal of Computational Physics*, 283:98–128, 2015.
- [22] S. Dong. Wall-bounded multiphase flows of N immiscible incompressible fluids: consistency and contact-angle boundary condition. Journal of Computational Physics, 338:21–67, 2017.
- [23] S. Dong. Multiphase flows of N immiscible incompressible fluids: a reduction-consistent and thermodynamically-consistent formulation and associated algorithm. *Journal of Computational Physics*, 361:1–49, 2018.
- [24] S. Dong and J. Shen. A time-stepping scheme involving constant coefficient matrices for phase-field simulations of two-phase incompressible flows with large density ratios. *Journal of Computational Physics*, 231(17):5788-5804, 2012.
- [25] C Eck, M Fontelos, G Grün, F Klingbeil, and O Vantzos. On a phase-field model for electrowetting. Interfaces Free Bound, 11(2):259–290, 2009.
- [26] Andrew MJ Edwards, Carl Vernon Brown, Michael I Newton, and Glen McHale. Dielectrowetting: The past, present and future. Current opinion in colloid & interface science, 36:28–36, 2018.
- [27] Helge Engan. Excitation of elastic surface waves by spatial harmonics of interdigital transducers. *IEEE Transactions on Electron Devices*, 16(12):1014–1017, 1969.
- [28] Peter RC Gascoyne, Jody V Vykoukal, Jon A Schwartz, Thomas J Anderson, Daynene M Vykoukal, K Wayne Current, Charles McConaghy, Frederick F Becker, and Craig Andrews. Dielectrophoresis-based programmable fluidic processors. Lab on a Chip, 4(4):299–309, 2004.
- [29] Hongyao Geng and Sung Kwon Cho. Dielectrowetting for digital microfluidics: principle and application. a critical review. *Reviews of Adhesion and Adhesives*, 5(3):268–302, 2017.
- [30] Y. Gong, J. Zhao, and Q. Wang. An energy stable algorithm for a quasi-incompressible hydrodynamic phase-field model of viscous fluid mixtures with variable densities and viscosities. *Computer Physics Communications*, 219:20–34, 2017.
- [31] G. Grun and F. Klingbeil. Two-phase flow with mass density contrast: stable schemes for a thermodynamically consistent and frame-indifferent diffuse-interface model. *J. Comput. Phys.*, 257:708–725, 2014.
- [32] Z. Guo, P. Lin, J. Lowengrub, and S.M. Wise. Mass conservative and energy stable finite difference methods for the quasi-incompressible Navier-Stokes-Cahn-Hilliard system: primitive and projecton-type schemes. *Comput. Meth. Appl. Mech. Engrg.*, 326:144–174, 2017.
- [33] Z. Guo, P. Lin, and J.S. Lowengrub. A numerical method for the quadi-incompressible Cahn-Hilliard-Navier-Stokes equations for variable density flows with a discrete energy law. *J. Comput. Phys.*, 276:486–507, 2014.
- [34] Morton E Gurtin, Debra Polignone, and Jorge Vinals. Two-phase binary fluids and immiscible fluids described by an order parameter. *Mathematical Models and Methods in Applied Sciences*, 6(06):815–831, 1996.
- [35] Robert A Hayes and B Johan Feenstra. Video-speed electronic paper based on electrowetting. Nature, 425(6956):383–385, 2003.
- [36] John David Jackson. Classical electrodynamics, 1999.
- [37] D. Jacqmin. Calculation of two-phase Navier-Stokes flows using phase-field modeling. *Journal of Computal Physics*, 155:96–127, 1999.
- [38] D. Jacqmin. Contact-line dynamics of a diffuse fluid interface. Journal of Fluid Mechanics, 402:57–88, 2000.
- [39] T.B. Jones. Liquid dielectrophoresis on the microscale. J. Electrostat., 51:290–299, 2001.
- [40] T.B. Jones, M. Gunji, M. Washizu, and M.J. Feldman. Dielectrophoresis liquid actuation and nanodroplet formation. *Journal of Applied Physics*, 89:1441–1448, 2001.
- [41] T.B. Jones, M.P. Perry, and J.R. Melcher. Dielectric siphons. Science, 174:1232–1233, 1971.
- [42] J. Kim and J. Lowengrub. Phase field modeling and simulation of three-phase flows. *Interfaces and*

- Free Boundaries, 7:435-466, 2005.
- [43] L.D. Landau and E.M. Lifshitz. Electrodynamics of continuous media, volume 8. Elsevier, 2013.
- [44] Yuan Lin, Paal Skjetne, and Andreas Carlson. A phase field model for multiphase electro-hydrodynamic flow. *International Journal of Multiphase Flow*, 45:1–11, 2012.
- [45] G. Linga, A. Bolet, and J. Mathiesen. Bernaise: A flexible framework for simulating two-phase electrohydrodynamic flows in complex domains. Frontiers in Ohysics, 7:21, 2019.
- [46] G. Linga, A. Bolet, and J. Mathiesen. Transient electrohydrodynamic flow with concentration-dependent fluid properties: Modeling and energy-stable schemes. *Journal of Computational Physics*, 412:109430, 2020.
- [47] Gaute Linga, Asger Bolet, and Joachim Mathiesen. Controlling wetting with electrolytic solutions: Phase-field simulations of a droplet-conductor system. *Physical Review E*, 98(1):013101, 2018.
- [48] C. Liu and J. Shen. A phase field model for the mixture of two incompressible fluids and its approximation by a fourier-spectral method. *Physica D*, 179:211–228, 2003.
- [49] C. Liu, J. Shen, and X. Yang. Decoupled energy stable schemes for a phase-field model of two-phase incompressible flows with variable density. *Journal of Scientific Computing*, 62:601–622, 2015.
- [50] J. Lowengrub and L. Truskinovsky. Quasi-incompressible Cahn-Hilliard fluids and topological transitions. Proceedings of Royal Society London A, 454:2617–2654, 1998.
- [51] Francesco Magaletti, Francesco Picano, Mauro Chinappi, Luca Marino, and Carlo Massimo Casciola. The sharp-interface limit of the Cahn-Hilliard/Navier-Stokes model for binary fluids. *Journal of Fluid Mechanics*, 714:95–126, 2013.
- [52] Xiaoyu Mao, Vaibhav Joshi, and Rajeev Jaiman. A variational interface-preserving and conservative phase-field method for the surface tension effect in two-phase flows. *Journal of Computational Physics*, 433:110166, 2021.
- [53] Glen McHale, Carl V Brown, Michael I Newton, Gary G Wells, and Naresh Sampara. Developing interface localized liquid dielectrophoresis for optical applications. In *Optical design and testing V*, volume 8557, pages 13–20. SPIE, 2012.
- [54] Glen McHale, CV Brown, MI Newton, GG Wells, and Naresh Sampara. Dielectrowetting driven spreading of droplets. *Physical review letters*, 107(18):186101, 2011.
- [55] S. Metzger. On numerical schemes for phase field models for electrowetting with electrolyte solutions. *Proc. Appl. Math Mech.*, 15:715–718, 2015.
- [56] S. Metzger. On stable dissipation reducing splitting schemes for two-phase flow of electrolytic solutions. Numer. Algor., 80:1361–1390, 2019.
- [57] Frieder Mugele and Jean-Christophe Baret. Electrowetting: from basics to applications. *Journal of physics: condensed matter*, 17(28):R705, 2005.
- [58] Ricardo H Nochetto, Abner J Salgado, and Shawn W Walker. A diffuse interface model for electrowetting with moving contact lines. *Mathematical Models and Methods in Applied Sciences*, 24(01):67–111, 2014.
- [59] Herbert A Pohl. The motion and precipitation of suspensoids in divergent electric fields. *Journal of applied Physics*, 22(7):869–871, 1951.
- [60] L. Rayleigh. On the theory of surface forces II. Phil. Mag., 33:209, 1892.
- [61] M. Schorpour Roudbari, G. Simsek, E.H. van Brummelen, and K.G. van der Zee. Diffuse-interface twophase flow models with different densities: a new quasi-incompressible form and a linear energy-stable method. *Mathematical Models and Methods in Applied Sciences*, 28:733–770, 2018.
- [62] A.J. Salgado. A diffuse interface fractional time-stepping technique for incompressible two-phase flows with moving contact lines. ESAIM: Mathematical Modeling and Numerical Analysis, 47:743-769, 2013.
- [63] D.A. Saville. Electrohydrodynamics: the Taylor-Melcher leaky dielectric model. Annual review of fluid mechanics, 29(1):27–64, 1997.
- [64] J. Shen and X. Yang. A phase-field model and its numerical approximation for two-phase incompressible flows with different densities and viscosities. SIAM Journal on Scientific Computing, 32:1159–1179, 2010.
- [65] J. Shen and X. Yang. Decoupled energy stable schemes for phase-field models of two-phase incompressible flows. SIAM J. Numer. Anal., 53:279–296, 2015.
- [66] J. Shen, X. Yang, and Q. Wang. On mass conservation in phase field models for binary fluids. Comminications in Computational Physics, 13:1045–1065, 2013.
- [67] Vijay Srinivasan, Vamsee K Pamula, and Richard B Fair. An integrated digital microfluidic lab-on-a-chip for clinical diagnostics on human physiological fluids. *Lab on a Chip*, 4(4):310–315, 2004.

- [68] Graeme Supeene, Charles R Koch, and Subir Bhattacharjee. Deformation of a droplet in an electric field: Nonlinear transient response in perfect and leaky dielectric media. *Journal of colloid and interface* science, 318(2):463–476, 2008.
- [69] M.F.P. ten Eikelder, K.G. van der Zee, I. Akkerman, and D. Schillinger. A unified framework for Navier-Stokes Cahn-Hilliard models with non-matching densities. *Mathematical Models and Methods in Applied Sciences*, 33:175–221, 2023.
- [70] Hongmiao Tian, Jinyou Shao, Yucheng Ding, Xiangming Li, and Hongzhong Liu. Numerical characterization of electrohydrodynamic micro- or nanopatterning processes based on a phase-field formulation of liquid dielectrophoresis. *Langmuir*, 29(15):4703–4714, 2013.
- [71] J. van der Waals. The thermodynamic theory of capillarity under the hypothesis of a continuous density variation. J. Stat. Phys., 20:197–244, 1893.
- [72] Sheng Wang, Junxiang Shi, Hsiu-Hung Chen, Tiancheng Xu, and Chung-Lung Chen. Numerical and experimental investigation of bubble dynamics via electrowetting-on-dielectric (ewod). In *International Conference on Micro/Nanoscale Heat Transfer*, volume 49651, page V001T04A003. American Society of Mechanical Engineers, 2016.
- [73] Yanbo Xie, Miao Sun, Mingliang Jin, Guofu Zhou, and Lingling Shui. Two-phase microfluidic flow modeling in an electrowetting display microwell. *The European Physical Journal E*, 39(2):1–5, 2016.
- [74] Su Xu, Hongwen Ren, and Shin-Tson Wu. Dielectrophoretically tunable optofluidic devices. *Journal of Physics D: Applied Physics*, 46(48):483001, 2013.
- [75] Qingzhen Yang, Ben Q Li, and Yucheng Ding. 3d phase field modeling of electrohydrodynamic multiphase flows. *International Journal of Multiphase Flow*, 57:1–9, 2013.
- [76] Qingzhen Yang, Ben Q Li, Jinyou Shao, and Yucheng Ding. A phase field numerical study of 3d bubble rising in viscous fluids under an electric field. *International Journal of Heat and Mass Transfer*, 78:820–829, 2014.
- [77] H. Yu and X. Yang. Numerical approximations for a phase-field moving contact line model with variable densities and viscosities. *Journal of Computational Physics*, 334:665–686, 2017.
- [78] P. Yue. Thermodynamically consistent phase-field modeling of contact angle hysteresis. *Journal of Fluid Mechanics*, 899:A15, 2020.
- [79] P. Yue, J.J. Feng, C. Liu, and J. Shen. A diffuse-interface method for simulating two-phase flows of complex fluids. *Journal of Fluid Mechanics*, 515:293–317, 2004.
- [80] P. Yue, C. Zhou, and J.J. Feng. Spontaneous shrinkage of drops and mass conservation in phase-field simulations. *Journal of Computal Physics*, 223:1–9, 2007.
- [81] Q. Zhao and W. Ren. A finite element method for electrowetting on dielectric. *Journal of Computational Physics*, 429:109998, 2021.